Università degli Studi di Salerno
Facoltà di Scienze MM. FF. NN.
Dipartimento di Chimica e Biologia

Development of Molecular Models of Interfaces using a Multi-Scale Hybrid Particle-Field Approach: Application to Composite Materials and Biomembranes

Antonio De Nicola

Salerno, 2013
Università degli Studi di Salerno
Dipartimento di Chimica e Biologia
Dottorato di Ricerca in Chimica, Ciclo XII

Tutor: Dr. Giuseppe Milano

Preface

This thesis presents some of the main results of my research performed at Department of Chemistry and Biology at University of Salerno during the period 2011-2013. The contents are divided in three parts, where the first constitutes the theoretical background of the particle-field method. The second contents consist in the study of the interface of polymer matrix with silica nanoparticle. The third part covers the investigation of polymer aggregates interacting with biomembrane.

List of Papers

1. De Nicola, A.; Zhao, Y.; Hezaveh, S.; Roccatano, D.; Kawakatsu, T.; Milano, G. *Phys. Chem. Chem. Phys.* **2014,** DOI: 10.1039/C3CP54242D
2. De Nicola, A.; Milano, G.; Kawakatsu , T. *Macromolecular Chemistry and Physics* **2013**, 214, 1940.
3. Milano, G.; Kawakatsu, T.; De Nicola, A. *Physical Biology* **2013**, 10, 045007.
4. De Nicola, A.; Zhao, Y.; Kawakatsu, T.; Roccatano, D.; Milano, G. *Theoretical Chemistry Accounts* **2012**, 131, 1167.
5. Hezaveh, S.; Samanta, S.; De Nicola, A.; Milano, G.; Roccatano, D. *The Journal of Physical Chemistry B* **2012**, 116, 14333.
6. Zhao, Y.; De Nicola, A.; Kawakatsu, T.; Milano, G. *Journal of Computational Chemistry* **2012**, 33, 868.

Acknowledgements

First of all I'd like to extend my gratitude to my supervisor Dr. Giusppe Milano for all the support and the time he dedicated to me during these years. I have learned invaluable amounts of chemistry and physics from him.
I also want to thank professor Toshihiro Kawakatsu of the Tohoku University, for all useful and interesting discussions about the MD-SCF method and all work made during my Ph. D. project. Thanks to Prof. Kawakatsu and my supervisor Dr. Milano, I had the possibility to work with this new promising technique MD-SCF.

I want to thank the IMAST S.c.a.r.l. to funding my Ph. D. project. In particular I am very grateful to Professor Luigi Nicolais to give me the possibiliy to become a part of very interesting and exciting research network about the polymer composites. After this experience in IMAST, I considerably improved my knowledge about different aspects of polymer composites. In IMAST I meet several enthusiastic people. I'm grateful to Dott.sa Eva Milella for all the support got me. Special thanks for Dr. Gianfranco Innocenti. He got me very useful suggestions and comments to my project. I want to thank also all guys in IMAST that shared with me these three years of Ph. D. project.

Sharing room with Anna Vangone e Raffaele Credendino, they become close friends over these years. I enjoyed for the time spent together. Thank You.

Finally, I'd like to thank my parents and my girlfriend Marianna for constantely encuraging me in this project.

Fisciano, Ferburary 2014

Antonio De Nicola

Contents

1
Introduction

"Development of Multiscale Models for Complex Chemical Systems"
Martin Karplus, Michale Levitt, Arieh Warshel
Nobel Prize in Chemisry 2013

1-1 Polymer Composite Materials

Polymer composite materials have been widely studied for a long time. They can be defined as material made by two different phases in which distinct interfaces separate different phases. When one of the phases becomes nanosized (of the order 0.1-100 nm), they are defined nanocomposites. The constituent of the continuous phase is called "*matrix*". Usually the matrix is more ductile and less hard phase. Instead, the "*dispersed*" phase is embedded in the matrix in a discontinuous form[1]. Such materials combine the advantages of the inorganic material (e.g., rigidity, thermal stability) and the organic polymer (e.g., flexibility, dielectric, ductility, and processability).

The peculiar features of polymer nanocomposite can be explained on the basis of the combined behavior of the

reinforcing element (nanofillers)/polymer matrix interface. It is immediately clear that the understanding of the links between the microstructure and the macroscopic properties is critical for the successful development of polymer composite materials.

A very relevant task in the theoretical material science is to build up models able to reproduce and predict the macroscopic properties of materials based on their constituent. Due to the nature of polymer nanocomposite, is well known that the fillers are in principle mobile. This implies that they can form clusters, of different size, having effects on the polymer matrix/nanoparticle interfaces that paly a strong role on the average properties of the material[2].

1-2 Multiscale of soft matter material

"Properties of soft matter systems are determined by a variety of processes and interactions originating from a wide range of time and length scales."

K. Kremer[5]

Though this holds for many physical systems, it is of special importance for soft matter, where the relevant energy scale is the thermal energy k_BT. Processes occurring on rather

different scales often are governed by rather similar energy scales. As a characteristic example let us mention phase segregation effects in polymers or block copolymers. While the local dynamics on the monomer level is dominated by bond angle, torsion, and excluded volume interactions, all typically of the order of a few k_BT, the free energy difference of the whole polymer in the homogeneous mixture and the segregated state is typically also of the orderof a few k_BT. Whereas the former processes occur on a ps or at most ns time scale (if far enough away from the glass transition temperature, which we will not discuss here), the latter can take up to seconds or more if only the chains are long enough. Consequently molecular simulation approaches to soft matter phenomena require a wide range of simulation methods, which appropriately deal with different levels of resolution. Coming back to the above example, generic aspects of polymer dynamics as well as certain aspects of conformational properties like chain stiffness can be studied by highly simplified and idealized models, while specific amplitudes and prefactors, which easily can vary by orders of magnitude, or local arrangements of groups usually require detailed microscopic input. Thus a variety of different models and simulation schemes has been developed, where microscopic structure information is employed to

parameterize higher level more coarse models[3-6]. While this defines length scaling factors rigorously by the very construction, it is not at all clear how to do that for dynamical quantities in a rigorous way. Actually for most molecular systems this might be even impossible. In the following we will focus on these problems. In this context we also will discuss a more pragmatic ansatz, which allows us to deduce dynamical information from coarse-grained models without any adjustable parameter not coming from the simulations themselves.

1-3 What This Thesis is About

The main aim of this thesis is to study, by simulation tools, the interfaces of different systems. In particular we want to investigate the role of the interface of both polymer matrix with silica nanoparticles and biological systems interacting with polymers. In both cases to approach to these problems we adopted a multiscale scheme in developing of models able to keep the nature of such problems. Specific models, using the hybrid Particle-Field Molecular Dynamic technique (PF-MD), have been developed. The features of PF-MD models allow us to study, with chemical detail, phenomena involving huge time and length scales otherwise not accessible with

standard MD techniques.

The thesis is organized in the following way. In the Chapter 2 a briefly description of the theoretical scheme of the hybrid PF-MD approach is reported. The main advantages of this approach will be described jointly with the implementation of this scheme to the MD.

In the Chapter 3 a strategy to obtain well-relaxed atomistic structure of polymer melt, employing the PF models, is reported. In particular a procedure to obtain well relaxed structure of polymethylmethacrylate (PMMA) and polyethylene oxide (PEO) is shown. Furthermore, as application, a study to characterize the interface of composite material of PMMA melt with Silica Nanoparticle is reported.

In the Chapter 4 the development and validation of PF models of different phospholipids is reported. In particular, the models have been tested and validated on the reproduction of lamellar and non-lamellar phase (i.e. micellar, hexagonal and inverse micelle). In order to validate such models, the main structural properties, calculated from the simulations, have been compared with experiments.

The development and validation of block-copolymer models is reported in the Chapter 5. In particular, models of Pluronic L64 and L62 have been developed and tested on the reproduction of phase behaviour in polymer/water mixture.

Furthermore, a study to understand the interaction between a Pluronic micelle and a lipid bilayer is reported.

References:

(1) Amrita Saritha; Sant Kumar Malhotra; Sabu Thomas; Kuruvilla Joseph; Koichi Goda; Sreekala, M. S. *Polymer Composites* Boschstr. 12, 69469 Weinheim, Germany, 2013; Vol. 2.
(2) Langner, K. M.; Sevink, G. J. A. *Soft Matter* **2012**, *8*, 5102.
(3) Tschöp, W.; Kremer, K.; Batoulis, J.; Bürger, T.; Hahn, O. *Acta Polymerica* **1998**, *49*, 61.
(4) Muller, M.; Schmid, F. In *Advanced Computer Simulation Approaches for Soft Matter Sciences Ii*; Holm, C., Kremer, K., Eds.; Springer-Verlag Berlin: Berlin, 2005; Vol. 185, p 1.
(5) Praprotnik, M.; Delle Site, L.; Kremer, K. *Annual Review Of Physical Chemistry* **2008**, *59*, 545.
(6) Ayton, G. S.; Voth, G. A. *Current Opinion in Structural Biology* **2009**, *19*, 138.

2
Hybrid Particle-Field Molecular Dynamics

The main idea of Self Consistent Field (SCF) techniques is to split up the calculation of multibody interactions in two procedures: i.e. to find the ensemble averaged conformation distribution and to find the segment potentials based on the segment distribution. For this aim, a set of partial differential equations are solved numerically using lattice approximations and a discrete set of coordinates, onto which segments can be placed, has to be defined. Parameters are defined so that the results of the Molecular Dynamic (MD) simulations are reproduced by those of the SCF simulations[1].

Müller and Schick[2] proposed a novel approach developing an off lattice representation of the field theory; they obtained the single-chain partition function via a partial enumeration[3] over a large set of molecular conformations of a lipid chain with RIS statistics.

More recently, the single chain in mean field (SCMF) method introduced by Müller *et al*, in which a density field is kept static for a number of Monte Carlo steps, has been

successfully applied to homopolymer and block copolymer systems[4-6].

One of the advantages of this hybrid approach is the lack of any limitation in treating complex molecular architectures and/or intramolecular interactions. In the frame of the hybrid scheme proposed by Müller, this approach has recently been extended to MD simulations. In particular, the MD method has been combined with SCF description (MD-SCF); an implementation suitable for the treatment of atomistic force fields and/or specific CG models has been reported and validated[7,8].

After the introduction of the MD-SCF approach, this kind of hybrid model, due to its computational efficiency, is also gaining popularity for biomembranes modeling. Very recently, Sevink *et al* introduced a hybrid scheme, combining Brownian dynamics (BD) and dynamic density functional theory (DDFT), that is able to model efficiently complete vesicles with molecular detail[9].

In the following the basic theoretical scheme of MD-SCF simulations and its implementation will be described.

2-1 Theoretical scheme

In this section, a description of the hybrid particle–field MD simulation scheme is given. For further details and a complete treatment of this approach the readers can refer to[7,8] where the

derivation and the implementation have been introduced and to[7,10] for a general aspect of SCF methods.

The main issue, according to the spirit of SCF theory, will be to derive the partition function of a single molecule in an external potential $V(\boldsymbol{r})$ and to obtain a suitable expression of the $V(\boldsymbol{r})$ and its derivatives. In this formulation, the most computationally expensive part of the MD simulations, i.e., the evaluation of the non bonded force and its potential between atoms of different molecules, can be replaced by evaluation for each atom of those with an external potential that depends on the local density at position $\boldsymbol{r}$.

In the framework of the SCF theory, a molecule is regarded to be interacting with the surrounding molecules not directly but through a mean field. According to this picture, we can split the Hamiltonian of a system of M molecules into two parts:

$$\hat{H}(\Gamma) = \hat{H}_0(\Gamma) + \hat{W}(\Gamma), \tag{1}$$

where Γ is used as shorthand for a set of positions of all atoms in the system, which specifies a point in the phase space. In Eq. (1) and also in the following, the symbol ^(hat) indicates that the associated physical quantity is a function of the microscopic states described by the phase space Γ.

$\hat{H}_0(\Gamma)$ is the Hamiltonian of a reference ideal system

composed of M non interacting chains but with all the intramolecular interaction terms (bond, angle, non bonded) that are usually considered in molecular simulations. On the other hand, the deviation from the reference system due to the intermolecular non bonded interactions is accounted for by the term $\hat{W}(\Gamma)$ in Eq. (1).

Assuming the canonical *(NVT)* ensemble, the partition function of this system is given by:

$$Z = \frac{1}{M!}\int d\Gamma \exp\left\{-\beta\left[\hat{H}_0\left(\Gamma\right) + \hat{W}\left(\Gamma\right)\right]\right\}, \tag{2}$$

The density distribution of atoms from microscopic point of view can be obtained considering that the microscopic density distribution can be defined as a sum of delta functions centered at the center of mass of each particle as:

$$\hat{\phi}\left(\mathbf{r};\Gamma\right) = \sum_{p=1}^{M}\sum_{i=0}^{N_M}\delta\left(\mathbf{r} - \mathbf{r}_i^{(p)}\right), \tag{3}$$

where M is the total number of molecules in the system, N_M is the number of particles contained in p-th molecule, $\mathbf{r}_i^{\left(p\right)}$ is the position of the i-th particle in p-th molecule.

The deviation $\hat{W}(\Gamma)$ from the reference state $\hat{H}_0$, Eq. 1,

originates from the interactions between molecules. To calculate the interaction term $\hat{W}(\Gamma)$ we need to introduce several assumption. First of all, we assume that $\hat{W}(\Gamma)$ depends on Γ only through the segment number density $\hat{\phi}$ (r;Γ) as:

$$\hat{W}\left(\Gamma\right) = W\left[\hat{\phi}\left(\mathbf{r};\Gamma\right)\right], \tag{4}$$

Using the assumption of Eq. (4) and the property of δ functional that obeys

$$\int D\{f(\mathbf{r})\}\delta\left[f(\mathbf{r}) - g(\mathbf{r})\right]F\left[g(\mathbf{r})\right] = F\left[f(\mathbf{r})\right], \tag{5}$$

we can rewrite the partition function of the Eq. (2) as:

$$\begin{aligned} Z = \frac{1}{M!}\int d\Gamma \int D\{\varphi(\mathbf{r})\}\delta\left[\varphi(\mathbf{r}) - \hat{\phi}(\mathbf{r};\Gamma)\right] \\ \times \exp\left\{-\beta\left[\hat{H}_0(\Gamma) + W\left(\varphi(\mathbf{r})\right)\right]\right\}. \end{aligned} \tag{6}$$

Using the Fourier representation of the delta functional, we obtain

$$\delta\left[\varphi(\mathbf{r})-\hat{\phi}(\mathbf{r};\Gamma)\right]= \\ \int D\{w(\mathbf{r})\}\exp\left[i\int w(\mathbf{r})\left\{\varphi(\mathbf{r})-\hat{\phi}(\mathbf{r};\Gamma)\right\}d\mathbf{r}\right]. \tag{7}$$

Inserting Eq. (7) into Eq. (6) leads to

$$Z=\frac{1}{M!}\int d\Gamma\int D\{\varphi(\mathbf{r})\}\int D\{w(\mathbf{r})\} \\ \times\exp\left[i\int w(\mathbf{r})\left\{\varphi(\mathbf{r})-\hat{\phi}(\mathbf{r};\Gamma)\right\}d\mathbf{r}\right] \\ \times\exp\left\{-\beta\left[\hat{H}_0(\Gamma)+W(\varphi(\mathbf{r}))\right]\right\}. \tag{8}$$

At that point we define z, as the partition function of a system made of a single molecule in an external potential $V(\mathbf{r})\equiv i/\beta(w(\mathbf{r}))$ as:

$$z\left[V(\mathbf{r})\right]=\int d\Gamma\exp\left\{-\beta\left[\hat{H}_0(\Gamma)+\int\hat{\phi}(\mathbf{r},\Gamma)V(\mathbf{r})d\mathbf{r}\right]\right\}. \tag{9}$$

Using this definition Eq. (9) and rearranging Eq. (8) we obtain

$$Z=\frac{1}{M!}\int d\Gamma\int D\{w(\mathbf{r})\}\exp\left\{-\beta-\left[\frac{1}{\beta}\ln z+W(\varphi(\mathbf{r}))\right.\right. \\ \left.\left.-\int V(\mathbf{r})\varphi(\mathbf{r})d\mathbf{r}\right]\right\}. \tag{10}$$

In terms of this partition function, the mean field approximation is obtained by replacing the sum over the

canonical ensemble in Eq. (10) with a Gaussian integral around the most probable state that minimizes the argument of the exponential function on the right side of Eq. (10).

The condition for the determination of the most probable state is given using functional derivatives:

$$\begin{cases} \dfrac{\delta}{\delta\phi(\mathbf{r})}\left\{-\beta\left[-\dfrac{1}{\beta}\ln z + W\left(\varphi(\mathbf{r})\right) - \int V(\mathbf{r})\left(\varphi(\mathbf{r})\right)d\mathbf{r}\right]\right\} = 0 \\ \dfrac{\delta}{\delta V(\mathbf{r})}\left\{-\beta\left[-\dfrac{1}{\beta}\ln z + W\left(\varphi(\mathbf{r})\right) - \int V(\mathbf{r})\left(\varphi(\mathbf{r})\right)d\mathbf{r}\right]\right\} = 0. \end{cases} \tag{11}$$

This lead to

$$\begin{aligned} V(\mathbf{r}) &= \frac{\delta W[\phi]}{\delta\phi(\mathbf{r})} \\ \phi(\mathbf{r}) &= -\frac{1}{z\beta}\frac{\delta z}{\delta V(\mathbf{r})} = \left\langle\hat{\phi}\left(\mathbf{r},\Gamma\right)\right\rangle = \phi(\mathbf{r}). \end{aligned} \tag{12}$$

According to the derivation given above, now it is possible to obtain an expression for a density dependent external potential acting on each molecule.

If we assume that the interaction term *W*, where each component species is specified by an index K, the density dependent interaction potential takes the following form:

$$W\left[\left\{\phi_K(\mathbf{r})\right\}\right] = \int d\mathbf{r}\left[\left(\frac{k_BT}{2}\sum_{KK'}\chi_{KK'}\phi_K(\mathbf{r})\phi_{K'}(\mathbf{r}) + \frac{1}{2\kappa}\left(\sum_K \phi_K(\mathbf{r}) - 1\right)^2\right)\right], \quad (13)$$

where the second addend of the integrand of Eq. (13) is the relaxed incompressibility condition and κ is the compressibility that is assumed to be sufficiently small. The corresponding mean field potential can be given by:

$$V_K(\mathbf{r}) = \frac{\delta W\left[\left\{\phi_K(\mathbf{r})\right\}\right]}{\delta\phi_K(\mathbf{r})} = k_BT\sum_{K'}\chi_{KK'}\phi_{K'}(\mathbf{r}) + \frac{1}{\kappa}\left(\sum_K \phi_K(\mathbf{r}) - 1\right). \quad (14)$$

In the case of a mixture of two components ***A*** and ***B***, the mean field potential acting on a particle of type ***A*** at position **r** is given by:

$$V_A(\mathbf{r}) = k_BT\left[\chi_{AA}\phi_A(\mathbf{r}) + \chi_{AB}\phi_B(\mathbf{r})\right] + \frac{1}{\kappa}\left(\phi_A(\mathbf{r}) + \phi_B(\mathbf{r}) - \phi_0\right). \quad (15)$$

In a similar way can be derived the expression for the mean field potential acting on a particle of type ***B***. Then the force

acting on a particle ***A*** at position **r**, due to the interaction with the density field is:

$$F_A(\mathbf{r}) = -\frac{\partial V_A(\mathbf{r})}{\partial \mathbf{r}} = \\ -k_B T\left(\chi_{AA}\frac{\partial \phi_A(\mathbf{r})}{\partial \mathbf{r}} + \chi_{AB}\frac{\partial \phi_B(\mathbf{r})}{\partial \mathbf{r}}\right) - \frac{1}{\kappa}\left(\frac{\partial \phi_A(\mathbf{r})}{\partial \mathbf{r}} + \frac{\partial \phi_B(\mathbf{r})}{\partial \mathbf{r}}\right). \quad (16)$$

2-2 Implementation scheme

As described by Milano and Kawakatsu[7,8], the implementation scheme for such approach is briefly described in follow. What is necessary in order to connect particle and field models is a scheme to obtain a smooth coarse-grained density function $\phi(\mathbf{r})$ directly from the particle positions Γ. Let us denote this procedure as:

$$\overline{S}\left\{\hat{\phi}(\mathbf{r},\Gamma)\right\} = \phi(\mathbf{r}), \quad (17)$$

where $\overline{S}$ is a symbolic name of the mapping from the particle positions to the coarse-grained density $\phi(\mathbf{r})$**.** The iteration scheme used, in the described particle-field approach, is reported in Figure 2-1.

The starting value of the density dependent mean field

potential is obtained from the initial configuration of the system (at the starting time t_0). The external potential due to the density dependent mean field potential can be evaluated. The potential energy is the sum of the intramolecular interaction potentials (bond, angle, torsion and intramolecular non bonded).

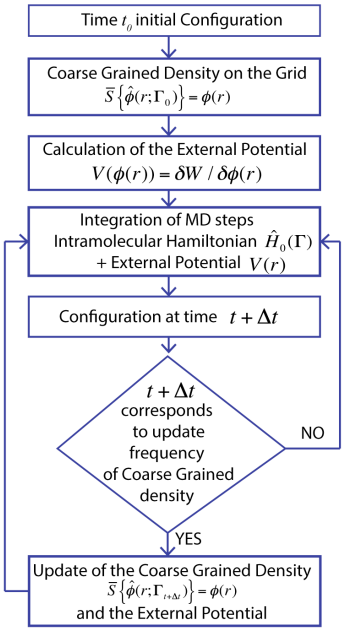

Figure 2-1. Iteration scheme proposed for the hybrid MD-SCF simulations.

A new configuration is obtained by integrating the equation of the motion of the particles from time t_0 to time $t_0+\Delta t$. At every prefixed density update time (Δt_{update}) the density is updated according to the new position of the particles in the system.

From the updated value of the density, a new value of the potential energy is calculated and then new forces acting on particles are obtained. The iteration scheme converges when the density and the potential become self-consistent.

It is immediately clear that the way to obtain a coarse-grained density, from the particle positions, is crucial in such approach. As shown by Milano and Kawakatsu[7,8], a simple and efficient way to obtain a coarse-grain density consist in to divide into *n*cell=*nx***ny***nz* cells (where *nx, ny, nz* are the number of cells in the *x, y* and *z* directions) the simulation box. According to their positions in the simulations box, all the particles are distributed among these cells. In the implementation proposed, the cell structure has been obtained using the method of "linked lists" that assures a rapid sorting of the particles.

The density and its derivatives used for the calculation of the forces and the potential energy due to particle-field interactions are both defined on three-dimensional lattice points obeying the periodic boundary conditions. The values of the density function at position **r** between lattice points are evaluated using linear interpolation of the values at neighbor lattice points.

Fractions of a particle are assigned to its neighbor mesh points according to the distances from the particle to the mesh points. There are several choices for this procedure. The

lowest order choice is to assign each particle to its nearest neighbor mesh point. This procedure means that the system is divided into cubic cells whose centers locate at the lattice points and assign all the particles inside a cell to its center lattice point. A higher order alternative is to consider also the position of each particle inside the cell and to assign a fraction of this particle to each vertex of the cell.

In order to explain such procedure, a simpler two-dimensional case is reported in Figure 2-2A. As example we consider a phospholipid molecule depicted on a grid used to evaluate the coarse-grained density.

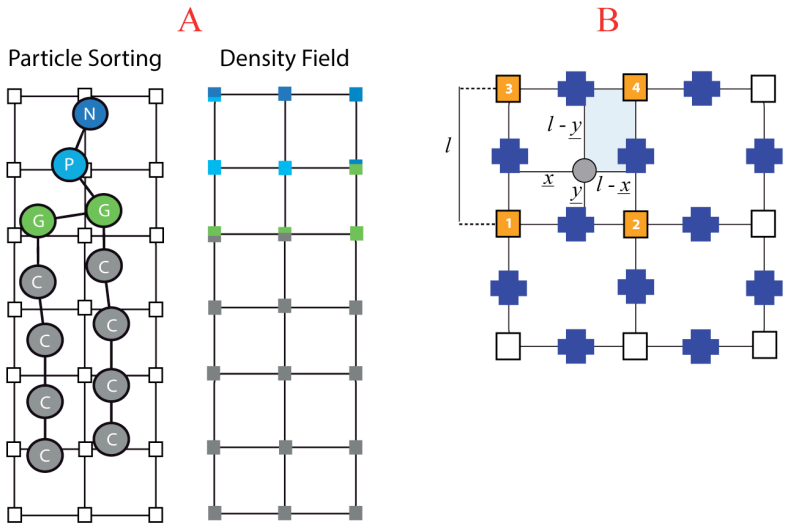

Figure 2-2. (A) Assignment of coarse-grained density to the lattice points for a molecule of phospholipid. (B) Criterion for assignment to a particle fraction to lattice points.

As shown in Figure 2-2B, the fraction of a particle assigned to

a given lattice point is proportional to the area of a rectangle showed in the figure. For example, for a particle with coordinates x and y a fraction $(l-x)*(l-y)/l^2$ will be assigned to the mesh point 1 and a fraction of $x*y/l^2$ at mesh point 4 (for simplicity l is the length of the cell both in x and y directions). Thus, the density at every mesh point is the sum of all fractions assigned from all the cells that share a given lattice point. According to the procedure described above, the size of the cell l is a parameter defining the density coarse-graining. Larger is the value of l, more particles will be included in every cell and coarser will be the calculated density.

Once the coarse-grained density has been calculated from particle positions, the spatial derivatives of the density field can be evaluated. Spatial derivatives can be obtained by differentiation of the density lattice. In this way the lattice where the derivatives are defined is staggered with respect to the lattice where the density is defined. As schematized in Figure 2-2B, the squares indicate the lattice points where the density is defined. Correspondingly, the density gradients are defined on the centre of each edge (staggered lattice points indicated by crosses in Figure 2-2B) of the square surrounding the density lattice points.

Once that both density and derivatives have been computed on their corresponding lattices, the potential energy and forces acting on the particles can be calculated using values obtained

by interpolation of the density and of its spatial derivatives in equations 15 and 16.

It is worth noting that the most time consuming part of the simulation (i.e. the evaluation of intermolecular forces calculated in a double loop over particle pairs) has been skipped completely; it is replaced, as pointed at the begin of the chapter, by an evaluation of a particle–field interaction term originating from the interaction of individual molecules with the density field $\varphi(\mathbf{r})$. Furthermore, due to the coarse grain nature of a collective field, it is possible to fix a time interval update without loss of accuracy. This choice is in agreement with the concepts behind the quasi-instantaneous field approximation discussed by Daoulas *et al* in the framework of SCMF Monte Carlo simulations[5]. The main assumption is that the field, as a collective variable with respect to particle coordinates, has a slow change with respect to a particle's displacement in one or more time-steps.

In this way, in MD-SCF simulations there are two time- steps. The first '*microscopic time-step*' is the usual one for the particle's displacement used in MD simulations and the second '*mesoscopic time-step*' is for the field update. The quasi-instantaneous field approximation can be compared with methods using different time-integration steps for 'stiff' and 'soft' degrees of freedom, albeit not in the context of a field-theoretical representation of interactions. A popular

example of this is MD algorithms with multiple time scales, introduced by Tuckerman *et al*[11]. The optimal value of the updated frequency depends on the density resolution (i.e. the size of the subcell where the particles are grouped), the system's nature and its conditions.

References:

(1) Leermakers, F.; Rabinovich, A.; Balabaev, N. *Physical Review E* **2003**, *67*, 011910.

(2) Muller, M.; Schick, M. *Physical Review E* **1998**, *57*, 6973.

(3) Szleifer, I.; Carignano, M. A. In *Advances in Chemical Physics*; John Wiley & Sons, Inc.: 2007, p 165.

(4) Daoulas, K. C.; Cavallo, A.; Shenhar, R.; Muller, M. *Soft Matter* **2009**, *5*, 4499.

(5) Daoulas, K. C.; Muller, M. *J. Chem. Phys.* **2006**, *125*.

(6) Daoulas, K. C.; Muller, M.; de Pablo, J. J.; Nealey, P. F.; Smith, G. D. *Soft Matter* **2006**, *2*, 573.

(7) Milano, G.; Kawakatsu, T. *Journal of Chemical Physics* **2009**, *130*, 214106.

(8) Milano, G.; Kawakatsu, T. *Journal of Chemical Physics* **2010**, *133*, 214102.

(9) Sevink, G. J. A.; Charlaganov, M.; Fraaije, J. G. E. M. *Soft Matter* **2013**, *9*, 2816.

(10) Kawakatsu , T. *Statistical Physics of Polymers. Springer: Berlin, 2004*

(11) Tuckerman, M. E.; Glenn, J. M.; Bruce, J. B. *J. Chem. Phys.* **1990**, *93*, 5.

3
Polymer Nanocomposites

3-1 Generation of Well Relaxed Atomistic Models of Polymer Melt.

High molecular weight polymer chains are difficult to relax. The longest relaxation of an entangled polymer melt of length N scales at least as N^3, giving at last N^4 in CPU time, which is only feasible for relatively short chain lengths. Although computational power increases 10-fold every five years, the huge number of degree of freedom limits fully atomistic approaches when it comes to investigating long polymer chains.

One way to circumvent this problem is to reduce the degree of freedom by coarsening the models and keeping only those degree of freedom that are deemed relevant for the particular range of interest. Simple models for the study of meso- and macroscale phenomena in polymers have been used

extensively[1,2].

On a larger length scale, dissipative particle dynamics (DPD) and smoothed particle dynamics (SPD) are frequently used to tackle hydrodynamic problems. The main drawback of these models is connected with their generic nature. Most of them, in fact, do not distinguish between chemically different polymers.

A useful method that is able to reproduce highly accurate physical properties is base on the mapping of atomistic features to mesoscopic models. Such approach, called "Coarse-graining" is able to keep the physical properties of different length scale of a polymer by adjusting force fields to relative length scale of interest. This approach have been applied, with success, to various polymers[3-7]. The most drawback of such approach is that for every length scale in which we are interested to simulate our polymer systems, the relative force-field must be adjusted. This request limits the applicability of the method to different length scales and, the procedure to tune the force-field at different length scales, is not trivial.

We report in the following section an application of particle-field approach to obtain well relaxed configurations of polymer melt at atomistic level. Differently from the standard "Coarse-grained" approach, the advantage of this approach

consists in easy way in which the scale length can be chose.

3-1.1 Procedure to obtain well-relaxed polymer melt configuration

To illustrate the procedure to obtain a well-relaxed configuration of a polymer melt, the atactic poly(methyl methacrylate) PMMA has been chose. The chemical structure of the PMMA, jointly with atoms definition, is reported in Figure 3-1.

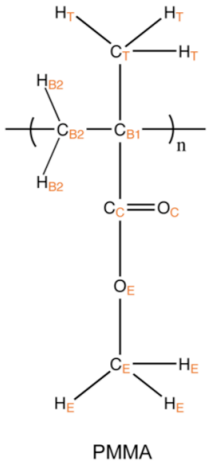

Figure 3-1. chemical structure of poly(methyl methacrylate).

We chose to apply the following procedure to four different molecular weights: 500 MW (corresponding to 5 repeating

units of PMMA), 1000 MW, 2000 MW and 180000 MW (corresponding to 180 repeating units), respectively. The composition of all simulated systems is reported in Table 3-1.

Table 3-1. Composition of simulated systems.

System	**M.W.** (g/mol)	**Rep. units**	**Nr. Particles**	**Box Size** x=y=z (nm)	**Temp.** (K)	**Time** (ns)
I	500	5	4620	3.63	500	20.0
II	1000	10	4560	3.68	500	20.0
III	2000	20	4530	3.65	500	20.0
VI	18000	180	8106	4.45	500	40.0

In order to validate this procedure we compared the results of standard atomistic simulation with the results obtained from particle-field simulations. Each system reported in Table 3-1 has been simulated with standard particle-particle atomistic model and with particle-field model. The force-field of particle-particle reference model has been took from the model of Maranas[8,9]. All intramolecular parameters, such

bond and angle interactions terms, of the particle-particle model have been used also for the particle-field model.

According to the spirit of the particle-field approach, as described in Chapter 2, the pair-pair intermolecular interaction are replaced by particle-field interactions. In such way each particle interacts with a field. According to the position of the particles in the system, a field is build and defined on a grid. Tuning the resolution of the grid, the representation of a molecule interacting with field changes. In other words, tuning the mesh size of the grid we can tune the smoothness of the intermolecular interactions. In particular, bigger is the mesh size and smoother is the intermolecular potential.

With this picture in mind, we performed for all systems in Table 3-1 three particle-field simulations by decreasing the mesh size from 0,8 nm to 0,4 until 0,2 nm. We studied the systematic effect of the grid size in the reproduction of properties, dynamics and statics, of the polymer bulk in comparison with particle-particle reference model.

3-1.2 Results and discussion

In order to compare the results of particle-field simulations with the particle-particle reference model, several properties,

statics and dynamics, have been calculated.

As important structural property, the radius of gyration (RG) has been calculated for all simulations of PMMA melts at *T*= 500 K with different chain lengths. In Figure 3-2, as function of molecular weight, the RG of particle-field and particle-particle simulations compared with experimental values are reported.

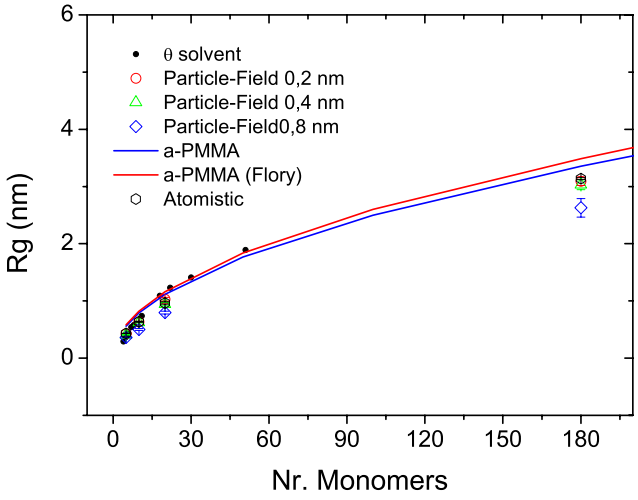

Figure 3-2. Radius of gyration for particle-field simulation, with different grid size, compared with particle-particle and experimental values.

The behaviour of the RG as function of molecular weight for the particle-field simulations show that smaller is the mesh size of a particle-field simulation and better is the agreement with particle-particle reference model. Starting from a mesh

size of 0.4 nm the agreement of RG of particle-field simulations is strictly close to particle-particle simulations. A small difference is found with a mesh size of 0.8 nm.

To characterize the efficiency of the particle-field approach in the global relaxation of the chains, the relaxation time τ of the autocorrelation function of the end-to-end vector, ***R***, was calculated. In Figure 3-3 the time τ is reported for all simulations.

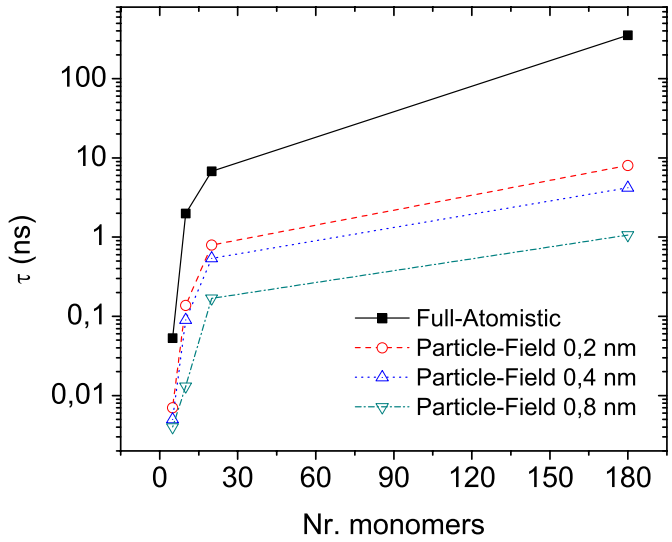

Figure 3-3. End-to-End relaxation time for particle-field and particle-particle simulations.

The behaviour of relaxation time as function of molecular weight shows that for the particle-field simulation the relaxation process is faster compared whit particle-particle

simulation. In particular, for high molecular weight the difference, in terms of τ, between particle-particle and particle-filed is about two orders of magnitude. In other words, this means that practically a standard particle-particle model is inaccessible to relax long chains.

Look at the fine structuration of the polymer melt, we can compare the reproduction of that one, for particle-field and particle-particle simulation, in terms of radial distribution function (RDF). In Figure 3-4 a comparison between particle-field, at different grid size, and particle-particle RDF calculate for the backbone is reported.

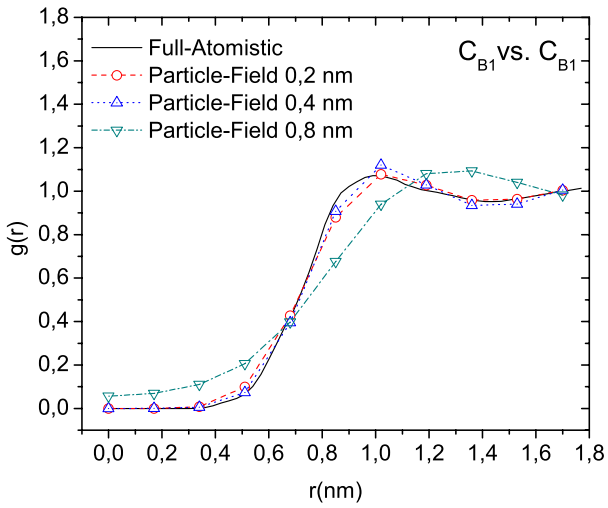

Figure 3-4. comparison of radial distribution function of the backbone calculate for particle-field (0.2 , 0.4 , 0.8 nm) and particle-particle. The definition of type of atom is reported in Figure 3-1.

What we found is that with small mesh size the particle-field simulations show a good agreement in the reproduction of local structure (non continuous red and blue curve of Figure 3-4).

In conclusion, considered all static and dynamic properties calculated for the particle-field simulations, we can select, by tuning the mesh size, the time scale that we want to relax. For example, with mesh size of 0.8 nm we are able to efficiently relax the end-to-end autocorrelation function. If we are interested to obtain a very accurate reproduction of local structuration of chains, we can achieve it by reducing the mesh size. Differently from a standard "coarse-grained" approach, the particle-field approach does not need to adjust ad-hoc the force-field to keep the properties of different length scale of a polymer.

In the following sections a particular application of particle-field approach, to obtain a well-relaxed melt polymer embedding a silica nanoparticle, will be show.

3-2 Study of interface of Polymer matrix with Silica Nanoparticle

Polymer reinforced with nanoparticles comprises an emerging class of materials due to their extraordinary enhanced properties. Compared to neat polymers, certain polymer nanocomposites exhibit a significant increase in tensile modulus and strength without loss of impact resistance and heat temperature[10]. Polymer nanocomposites offer new multifunctional properties, which are not observed with micrometer size fillers. For example, compared to the pure poly(methyl methacrylate) (PMMA), a higher transparency, an increase in the tensile strength, storage elastic modulus and surface hardness, an improvements in the thermal stability in the PMMA-silica nanocomposites, are reported[11]. Also, addition of such fillers as carbon nanotubes to the PMMA increases the Young modulus, and the hardness of the composite[12].

Among polymers, PMMA is the most commercially important acrylic polymer, used in many applications. Because of its high transparency and low density, PMMA is an ideal replacement for glass. Being compatible with human tissue makes PMMA an important material for transplants and

prosthetics, especially in the field of ophthalmology. Also because of similarity of its elastic modulus to natural bone, PMMA is used as bone cement on orthopaedic surgery. Due to the widespread applications of PMMA, nanocomposites have been prepared from it by the addition of nanoparticles such as organically modified clays, layered double hydroxides[13], layered hydroxyl salts[14], silica[15] and carbon nanotubes[16]. Despite the improvements achieved, the development of polymer nanocomposites is still largely empirical. Therefore, a better understanding of structure-property relationships between polymer and filler is still needed in the improvement of different classes of nanocomposites.

Computer modelling and simulation play an important role in predicting and designing material properties, and guiding synthesis and characterization. These methods are of particular importance in elucidating the molecular understanding of the structure and dynamics at the interface between nanoparticles and polymer matrix and, hence, the molecular origins of such phenomena as reinforcement, and the impact on the mechanical, thermal, fire, and barrier properties. Although Monte Carlo (MC) and Molecular Dynamics (MD) simulation methods have been widely applied to study the structure and dynamics of model bead-

spring polymer chains in contact with model (spherical) nanoparticles[17], simulations of realistic polymer-nanoparticle systems are relatively scarce.

Of the limited reports on the MC and/or MD simulations of realistic polymer chains in contact with particle surface we may address to the works by Barbier et al.[18] od the MD simulation of interface between poly(ethylene oxide) and silica, MD simulations on the interphase structure and dynamics of polystyrene near bare and coated Au nanoparticles, by Milano et al.[19,20] and that of polyimide near a silica nanoparticle, by Komarov et al.[20]. In addition some study about atomistic[21] and coarse-grained[22] MD simulations of polystyrene-silica nanoparticle have been recently published.

The results of all of these studies indicate that the filler modifies the polymer structure in its neighbourhood.

We performed detailed atomistic simulations of PMMA and its monomer MMA in contact with spherical silica nanoparticles.

3-2.1 Models: MMA, PMMA and Silica Nanoparticle

MD simulations were performed on both, MMA and PMMA systems containing a spherical Silica nanoparticle of diameter

of 3 nm. The spherical Silica nanoparticle were made according to the crystal structure of α-quartz applying the same procedure described by Brown[22,23] and Muller-Plathe[22]. In such way all silicon atoms lying outside a spherical surface as well as oxygen atoms not bonded to the retained silicon atoms were deleted. All surface silicon atoms bonded with three surface oxygen atoms were deleted and all the remaining surface oxygen atoms were saturated with hydrogen to satisfy their chemical valence.

The PMMA chains were composed of 5 repeating units, for which the chemical structure is shown in Figure 3-1. The force-field parameter were taken from Maranas[8,9].

For the MMA molecule a starting set of parameters based on the OPLS-AA have been considered. The starting set of parameters has been tuned to better reproduce both, the density of bulk and the enthalpy of vaporization.

For both systems, MMA/NP and PMMA/NP, the simulations have been performed at 303 K. The temperature and pressure (101.3 kPa) were kept constant by coupling the system to a Berendsen thermostat and barostat. All nonbonded interactions were truncated at 0.80 nm and the Culombic interactions are evaluated by reaction field correction. All simulation have been performed with GROMACS(ver. 4.5.4). The composition of the systems is reported in table 3-2.

Table 3-2. Details about Simulated Systems

Composition					
No. of MMA	**No. of PMMA**	**No. of Silica NP**	**Total No. of Particles**	**Temp. (K)**	**Simulated time (ns)**
3981	-	1	61116	303	60
-	757	1	59690	303	60

3-2.2 Discussion and Results

Due to the complexity of the system, a key point to study the polymer/NP structure in the interphase is to obtain a well-relaxed initial configuration. Differently from all examples reported in the introduction section, we prepared the initial configuration using the particle-field approach. As shown in the section 3-1 the particle-field approach allows us to obtain well-relaxed structure, with atomistic detail, of polymer melts. A similar procedure has been applied to obtain the initial configuration of both systems, PMMA/NP and MMA/NP. From those initial configurations, standard NPT simulations have been preformed.

For the systems tabulated in Table 3-2, the radial distribution function (RDF) are reported in Figure 3-5. The RDF are calculated considering both, the center of mass (CoM) of each PMMA repeating units and the CoM of each MMA molecule. The results are time-averaged (over the last 2 ns of

trajectories) and reported as a function of distance, *d*, from the CoM of silica nanoparticles.

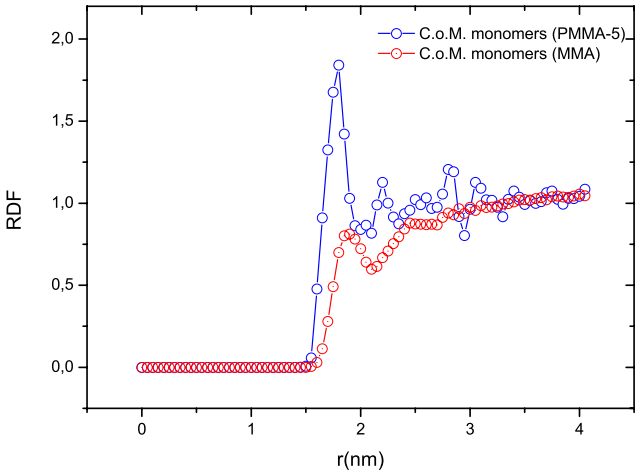

Figure 3-5. Radial distribution function for PMMA (blue curve) and MMA (red curve). 0 nm corresponds to the center of mass of silica nanoparticle.

The plot in Figure 3-5 indicates that a bigger adsorption of PMMA, respect to the monomer MMA, on the silica surface is found. At 1.5 nm of the plot, corresponding to the surface of silica nanoparticle, the value of RDF for the MMA is less than the bulk density (1 corresponds to the bulk density). The PMMA, instead, shows a bigger structuration on the silica surface, more than those one present in bulk.

The interface region between silica NP and polymer bulk can

be evaluated from the RDF in Figure 3-6, in which is clear that the external hydrogen atoms are located in a narrow region of about 0.5 nm. Such hydrogen atoms on the surface are able to interact with polymer bulk.

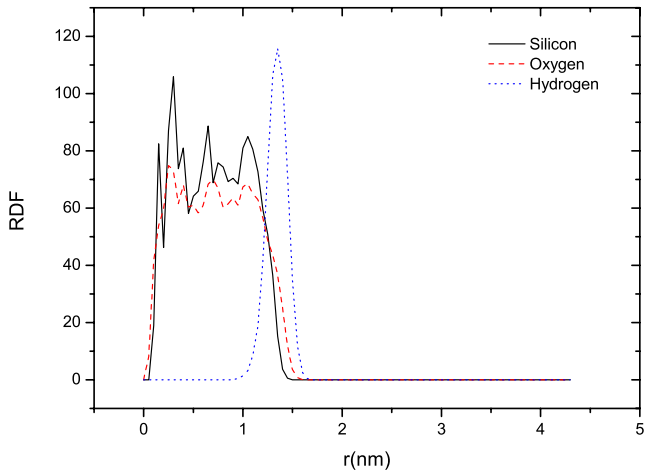

Figure 3-6. Radial distribution function of: silicon atoms (black continuous curve), oxygen atoms (red curve) and hydrogen atoms (blue curve) calculated respect the center of mass of silica nanoparticle.

A distinct feature of the polymer/monomer nanocomposite reported is the possibility of hydrogen bond (HB) formation between the O-H hydrogens of the silica nanoparticle surface and the carbonyl oxygen atoms O of both, PMMA and MMA. In our study the hydrogen bonds are counted based on a geometric criterion in which H•••O bond distance is 0.35 nm and the *donor-acceptor* angle $\theta_{OH\cdots O}$ is 130°. Based on these

criteria, we have counted the number of hydrogen bonds between silica-nanoparticle and both, PMMA and MMA. In Figure 3-7 the comparison between PMMA and MMA is reported. To better understand the behaviour of hydrogen bonds formation, we performed two additional simulations at higher temperature (333 and 353K).

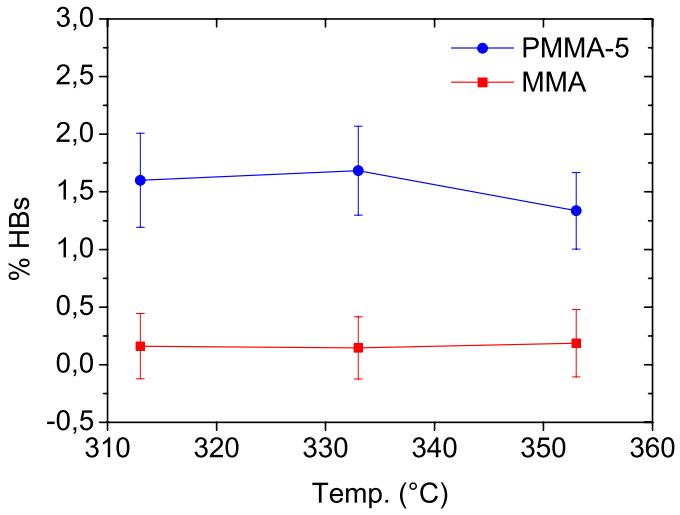

Figure 3-7. Percentage of HB normalized respect to the number of hydrogen donors present on the silica surface.

Only few papers are present in literature about simulation, at atomistic detail, of polymer-nanoparticle systems capable to form HB's[18,24]. Moreover, to our knowledge, none of them investigated and compared the hydrogen bond formation

between silica nanoparticle surface of both, PMMA and its monomer MMA. What we found, as confirm of RDF comparison, is the presence of HB's only in PMMA/silica NP system. In fact the MMA is less adsorbed on the silica surface not only respect to the PMMA but also compared with its bulk density. These results have been preliminary confirmed by experimental FTIR-ATR spectra in which the presence of broad peak at 1719 for the silica NP/PMMA and the absence of the same peak in silica NP/MMA (Figure 3-8). This is a strong indication of the different between the polymer and the monomer molecules.

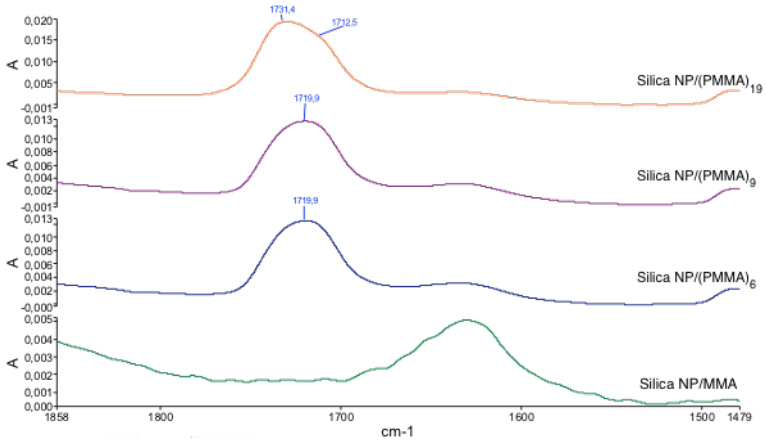

Figure 3-8. Experimental FITR-ATR spectra of silica nanoparticle in: MMA, $PMMA_6$, $PMMA_9$ and $PMMA_{19}$.

3-3 Conclusions

Atomistic molecular dynamics simulation for a nanoparticle in poly(methyl methacrylate) and methyl methacrylate, for a long time, up to 60 ns, are performed. The simulated systems contain a nanoparticle of diameter 3 nm. Polymer chains have been found in a more structured layer closer to the silica nanoparticle surface, compared with the monomer molecules. Moreover, we found that polymer chains form hydrogen bonds with the surface. Differently the monomers have been found to form not hydrogen bonds. The results obtained from the atomistic simulations have been preliminarily confirmed by experimental FTIR performed on similar system.

Thanks to the particle-field approach, the hardest task, that is the obtaining of an initial configuration well relaxed at the correct density, can be easily got. In such way also a very complex system as nanocomposite made by nanoparticle in a polymer matrix can be prepared at atomistic detail in a very easy way. This approach opens the way to study at the different levels (time and length scales) complex nanocomposite systems at atomistic detail.

References:

(1) De Gennes, P.-G. *Scaling Concepts in Polymer Physics Cornell University Press: Ithaca, New York, 1979*.
(2) Doi, M. E., S. F. *The Theory of Polymer Dynamics; Oxford University Press: New York, 1986*.
(3) Reith, D.; Pütz, M.; Müller-Plathe, F. *Journal of Computational Chemistry* **2003**, *24*, 1624.
(4) Muller-Plathe, F. *Chem. phys. chem.* **2002**, *3*, 754.
(5) Milano, G.; Muller-Plathe, F. *Journal of Physical Chemistry B* **2005**, *109*, 18609.
(6) Carbone, P.; Karimi-Varzaneh, H. A.; Muller-Plathe, F. *Faraday Discuss* **2010**, *144*, 25.
(7) Chen, X.; Carbone, P.; Santangelo, G.; Di Matteo, A.; Milano, G.; Muller-Plathe, F. *Physical Chemistry Chemical Physics* **2009**, *11*, 1977.
(8) Chen, C.; Maranas, J. K.; Garcia Sakai, V. *Macromolecules* **2006**, *39*, 9630.
(9) Depa, P. K.; Maranas, J. K. *The Journal of Chemical Physics* **2005**, *123*, 094901.
(10) Ramanathan, T.; Stankovich, S.; Dikin, D. A.; Liu, H.; Shen, H.; Nguyen, S. T.; Brinson, L. C. *Journal of Polymer Science Part B: Polymer Physics* **2007**, *45*, 2097.
(11) Sugimoto, H.; Daimatsu, K.; Nakanishi, E.; Ogasawara, Y.; Yasumura, T.; Inomata, K. *Polymer* **2006**, *47*, 3754.
(12) Luo, J.-T.; Wen, H.-C.; Wu, W.-F.; Chou, C.-P. *Polymer Composites* **2008**, *29*, 1285.
(13) Wang, G.-A.; Wang, C.-C.; Chen, C.-Y. *Polymer Degradation and Stability* **2006**, *91*, 2443.
(14) Majoni, S.; Su, S.; Hossenlopp, J. M. *Polymer Degradation and Stability* **2010**, *95*, 1593.
(15) Rittigstein, P.; Priestley, R. D.; Broadbelt, L. J.; Torkelson, J. M. *Nat Mater* **2007**, *6*, 278.
(16) Lee, W.-J.; Lee, S.-E.; Kim, C.-G. *Composite Structures* **2006**, *76*, 406.
(17) Starr, F. W.; Schrøder, T. B.; Glotzer, S. C. *Macromolecules* **2002**, *35*, 4481.
(18) Barbier, D.; Brown, D.; Grillet, A.-C.; Neyertz, S. *Macromolecules* **2004**, *37*, 4695.
(19) Milano, G.; Santangelo, G.; Ragone, F.; Cavallo, L.; Di Matteo, A. *The Journal of Physical Chemistry C* **2011**, *115*, 15154.

(20) Komarov, P. V.; Mikhailov, I. V.; Chiu, Y. T.; Chen, S. M.; Khalatur, P. G. *Macromolecular Theory and Simulations* **2013**, *22*, 187.
(21) Ghanbari, A.; Böhm, M. C.; Müller-Plathe, F. *Macromolecules* **2011**, *44*, 5520.
(22) Eslami, H.; Rahimi, M.; Müller-Plathe, F. *Macromolecules* **2013**, *46*, 8680.
(23) Brown, D.; Mélé, P.; Marceau, S.; Albérola, N. D. *Macromolecules* **2003**, *36*, 1395.
(24) Hong, B.; Panagiotopoulos, A. Z. *The Journal of Physical Chemistry B* **2012**, *116*, 2385.

4
Particle-Field Model of Phospholipids

4-1. Introduction to Phospholipid Bilayer

Phospholipids are an important class of biomolecules. Their amphiphilic nature allows them, when they are dissolved in water, to self-assemble into a lipid bilayer with lipid tails shielded from water and polar head groups exposed to the polar environment. In living organism, lipid bilayers form cellular membranes. Biological membranes are complex structures, and despite the considerable amount of information accumulated, experimental methods able to follow their dynamics with details at the atomic level are not yet available[1-5]. For these reasons, lipid bilayers have attracted the interest of the computational biophysics community, and atomistic molecular dynamics (MD) simulations of these systems have been performed for a long time[6-9]. However, these simulations are still computationally very expensive to

study processes occurring on the mesoscopic time (> μs) and length scales (> 100 nm)[10]. Therefore, to overcome this problem, alternative computational methods aiming to bridge the time and length scales involved in the relevant phenomena are constantly proposed. In the past few years, coarse-grained (CG) simulations became a very popular method for studying these systems. The CG approach involves the reduction of degrees of freedom in the atomic model of the simulated system by combining several atoms to a single particle ("effective bead"). CG methods have been successfully applied to several problems involving polymers,[11] biomolecules[2], and more in general soft matter[12].

For phospholipids, different types of CG models have been developed. Sintes and Baumgartner[13,14] developed a coarse-grained model for lipid bilayers where the solvent is implicitly taken into account. Later, Lenz and Schmid developed this implicit-solvent model to pure lipid bilayers composed of saturated lipids[15]. On the other hand, Goetz and Lipowsky[16] introduced an explicit-solvent CG model for lipid membranes where a binary Lennard-Jones fluid for the solvent and a short chain of beads for the amphiphilic molecules are used.

The degree of coarse-graining of a simulated system is related to the type of process that one wants to investigate. Minimalist CG models (e.g., having a very low discrimination

of the chemical details of the molecule) can be successfully applied to study self-assembly phenomena involving many molecules when the structure and dynamics on atomistic length scales can be considered irrelevant for the process, and systems can be conveniently described by only a small number of key properties, e.g., the amphiphilic nature of the molecule. Usually for membrane systems, a clear separation in length, time, and energy scales assumed by this approach is often missing, and the chemical specificity of the models have to be taken into account. Furthermore, these simple models can fail to reproduce more complex phenomena involving specific interactions of membrane with other molecular systems (e.g proteins, polymers). In these cases, the generic nature of the minimal coarse-grain models limits their application.

To possibly avoid these problems, more specific CG models can be developed. These CG models usually employ several different types of beads (not just hydrophobic and hydrophilic). A successful and very widely explored example of this approach is the MARTINI CG model developed by Marrink and co-workers[17]. In the MARTINI force field, beads having different Lennard-Jones interactions, that can smoothly modulate their hydrophobic/hydrophilic character, describe the phospholipids. In addition, water molecules are

treated explicitly with a coarse-grained reduction scheme of four molecules to one. Despite its simplicity, the MARTINI force field is able to reproduce with surprisingly good accuracy the properties of the self-assembly of lipid bilayers[7,18,19].

On the other hand, different computational approaches based on field representations have been proposed to model soft matter systems. In particular, in the framework of the self-consistent field (SCF) theory, the model systems are not represented by particles but by density fields, and the mutual interactions between segments are decoupled and replaced by an interaction between the segments and static external fields[20]. In the SCF theories, these external fields depend on the statistical average of the spatially inhomogeneous density distributions of segments of independent molecules, which are interacting only with these fields. Such external fields and the particle density distributions have to be determined self-consistently.

Several models have been reported in the literature to study mixtures of phospholipids and water using a field-based approach. Marcelja[21] proposed the first field model. In this model, the head groups of the lipid molecules are modeled as a boundary to which the tails of the lipid molecules are anchored. The intramolecular degrees of freedom are sampled

using the rotational isomeric state (RIS) model, where the segments interact through an anisotropic aligning potential[21]. The inequivalence of tail, head, and solvent segments allows the modeling of bilayers as preassembled structures, and it does not allow the study of self- assembly. Later, a fully self-consistent framework that is capable of describing stable, tensionless, self-assembled bilayers has been proposed. Both random-chain and the RIS-chain models result in membranes with qualitatively similar segment distributions and with similar thermodynamic properties[22]. Quantitatively, however, this approach underestimates the experimentally measured membrane thickness by about 50%[23]. More recently, molecular-level SCF theories that are able to treat phospholipids have been proposed[24]. The main point of these SCF techniques is to split up the calculation of multibody interactions into two procedures: i.e., to find the ensemble averaged conformation distribution and to find the segment potentials based on the segment distribution. For these purposes, differential equations have to be solved numerically using lattice approximations, and a discrete set of coordinates onto which segments can be placed has to be defined. Layers are defined imposing reflecting boundary conditions to mimic a multi-lamellar system. Parameters are defined so that the results of the MD simulations match those of the SCF

simulations. Müller and Schick[25] proposed an alternative approach developing an off-lattice representation of the field theory and obtained the single-chain partition function via a partial enumeration[26] over a large set of molecular conformations of a lipid chain with the RIS statistics. As the partition function of a single lipid in an external field cannot be obtained analytically for a realistic molecular architecture, one has to approximate the probability distributions of the conformations of non-interacting lipid molecules by a representative sample of single lipid conformations.

More recently, Müller and Smith[27] introduced a hybrid approach in the framework of SCF theory by combining it with a Monte Carlo simulation of a coarse-grained model of polymer chains to study phase separation in binary polymer mixtures. This approach has been widely and successfully applied by Müller and co-workers to coarse-grained models of diblock copolymer thin films[28] and polymer nanocomposites[29]. One of the advantages of this hybrid approach is the lack of any limitation in treating complex molecular architectures and/or intramolecular interactions.

Particle-based CG models like MARTINI are still computationally expensive compared to SCF approaches. In the following, we will refer to these models as particle-particle (PP) models. On the other hand, SCF approaches

ensure accessibility to definitely larger length and time scales but at the cost of very low chemical specificity. The idea behind the combined MD- SCF method is to obtain a strategy, as far as will be possible, having the main advantages and avoiding the main disadvantages of both techniques.

In this chapter, will be reported the development of coarse-grained specific models for biologically relevant phospholipids that are suitable for the hybrid MD-SCF techniques. In the following, we will refer to these models as particle-field (PF) models.

In the Chapter 2, a description of the theoretical approach of the hybrid MD-SCF method is reported.

4-2. Particle Field Models of Phospholipids

As described in Chapter 2, according to the formulation of hybrid PF models, the intramolecular bonded interactions (bond, angles) can be modeled using usual force fields suitable for molecular simulations. Our choice is to develop a hybrid PF model based on a description able to retain the chemical specificity. The coarse-graining scheme proposed by Marrink and co-workers is suitable for this purpose. The advantages of this model are that the parameterization of the interaction potentials is not tailored to a specific lipid and different phospholipids can be modeled from a small set of bead types.

In Figure 4-1, the MARTINI coarse-graining mapping scheme of the atomistic structures is exemplified for the phospholipid dipalmitoylphosphatidylcholine (DPPC).

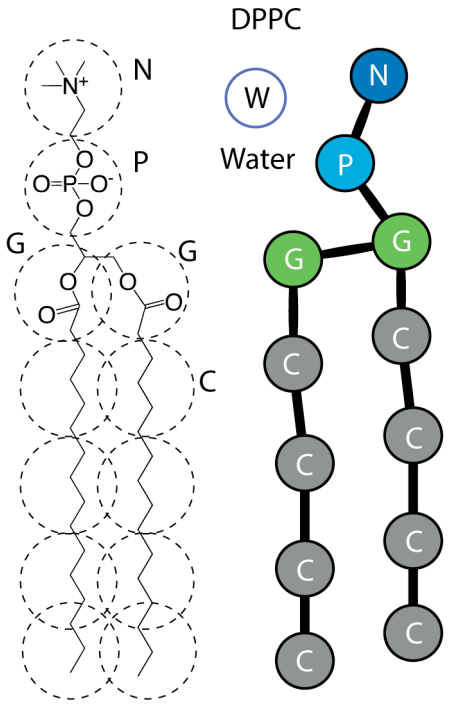

Figure 4-1. Adopted CG mapping scheme for the DPPC phospholipid. One CG bead corresponds about to 4 atoms.

According to the formulation of the MD-SCF method, bond and angle interaction potentials have the same functional form and parameters as those in the original MARTINI force field[17]. All types of nonbonded intramolecular interactions are assumed to be repulsive, while the intermolecular interactions are calculated using the assumption that each coarse-grained bead interacts with the density fields. According to Eq. (1), in order to calculate the PF potential, several mean field

parameters $\chi_{KK'}$ between a particle of type K with the density field due to particles of type K' are needed. A simple choice of these parameters can be obtained by following the Flory Huggins approach for the calculation of χ parameters for lattice models:

$$\chi_{KK'} = \frac{Z_{CN}}{K_B T}\left[\frac{2u_{KK'} - (u_{KK} + u_{K'K'})}{2}\right]. \qquad (1)$$

Where $u_{KK'}$ is the pairwise interaction energy between a pair of adjacent lattice sites occupied by the beads of types K and K'. These interaction energies have been set as $u_{KK'} = -\varepsilon_{KK'}$, where $\varepsilon_{KK'}$ is the Lennard-Jones ε parameter for the corresponding PP interactions. The parameter Z_{CN} in Eq. (1) is the coordination number, which takes a value of 6 for a three-dimensional lattice. Another way to obtain the coordination number is from integration of the radial distribution function between all possible pairs. As the initial state for the MD simulations, we prepare a randomly mixed state of 208 DPPC and 1600 CG water molecules. Then, this mixture is subjected to an energy minimization procedure in order to avoid particle overlapping. This procedure gives an average number of neighbors per particle calculated at a

distance equal to 1.20σ close to 6.0. With the choices described above, it is possible, given the particle-particle ε parameters and the value of Z_{CN}, to obtain the corresponding PF parameters. According to our choice, the χ parameters have been obtained considering the interactions between the different particle types classified according to the four types polar, nonpolar, apolar, and charged interactions considered in the MARTINI force field[17].

Using the models and the PF parameters described above, we simulated a system of DPPC and water using small values of both grid size (l = 0.587 nm, corresponding to 1.25σ) and update frequency (0.3 ps, corresponding to 10 time steps).

In order to determine the value of the parameter κ, which regulates the strength of the incompressibility condition imposed in Eq. (14) of the Chapter 2, we analyzed the behavior of density fluctuations in the reference PP simulation. The criterion is the reproduction of the value of the average density fluctuations, calculated as mean square deviation between the average total density and instantaneous value averaged over all lattice points using the same grid size used in PF simulations. In particular, using values of 1/κ of about $8RT$ (where R is the gas constant and T temperature), average density fluctuations, in agreement with the reference PP simulation, are found to be smaller than 1%.

The system has been simulated for 60 ns. In Figure 4-2, snapshots of the simulations together with calculated electron density profiles are reported. Here, the electron density profiles are obtained by multiplying the particle number density by the number of electrons contained in a given bead. As shown in Figure 4-2C, similarly to the reference PP simulation, the hybrid PF simulation leads to a successful formation of a lipid bilayer. Further comparisons between the results of PP and PF MD simulation have been used to refine the set of initial χ parameters obtained using Eq. (1).

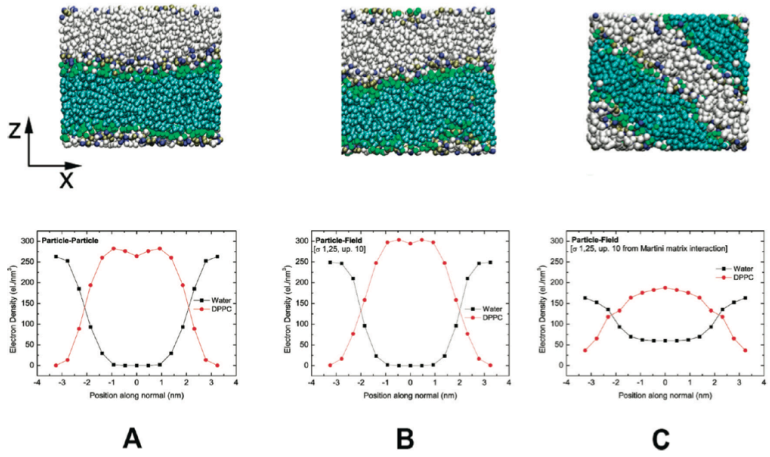

Figure 4-2. Water and DPPC density profiles and snapshots for (A) reference PP simulation, (B) PF simulation using a χ_{CW} parameter 2.5 times larger than the value calculated by Eq. (1), (C) PF simulation using χ_{CW} parameter calculated by Eq. (1).

In Figure 4-2, electron density profiles calculated by PP and PF MD simulations for the DPPC/water system (bottom panel

of Figure 4-2) have been compared.

From a comparison of the density profiles of Figures 4-2A and B, it is clear that the PF model gives a weaker phase separation between DPPC and water molecules with respect to the MD simulation. Furthermore, the snapshot of Figure 4-2C shows that, for the system simulated with the hybrid PF method, the phospholipid plane lies along the diagonal of the simulation box. This indicates the tendency of the lipid molecules to occupy a larger area for the lipid. This tendency can be connected to a different size of the lipid molecules in the PF simulations from that of the PP simulations. To show this, the radius of gyration and the angle between two tails obtained from PP and PF simulations have been compared.

As a result, both weak phase separation between the lipid and water and the tendency to occupy a larger area per lipid can be mainly ascribed to an underestimation of repulsion between the DPPC molecules and water in PF models with respect PP ones. Following this idea, several simulations were conducted to refine the interaction parameter between the hydrophobic tails of lipids and water molecules (namely the χ_{CW} parameter). Test simulations show that starting from values of χ_{CW} parameter 2.5 times larger than the value calculated by Eq. (1), the lipid bilayer does not occupy a larger area per lipid than the PP simulations and lies parallel

to the *xy* plane of the simulation box. In Figure 4-3, density profiles of DPPC, water, and the phosphate group (P) obtained from simulations, in which the repulsion between water and hydrophobic tail is further increased to 3 times that obtained with Eq. (1), are reported.

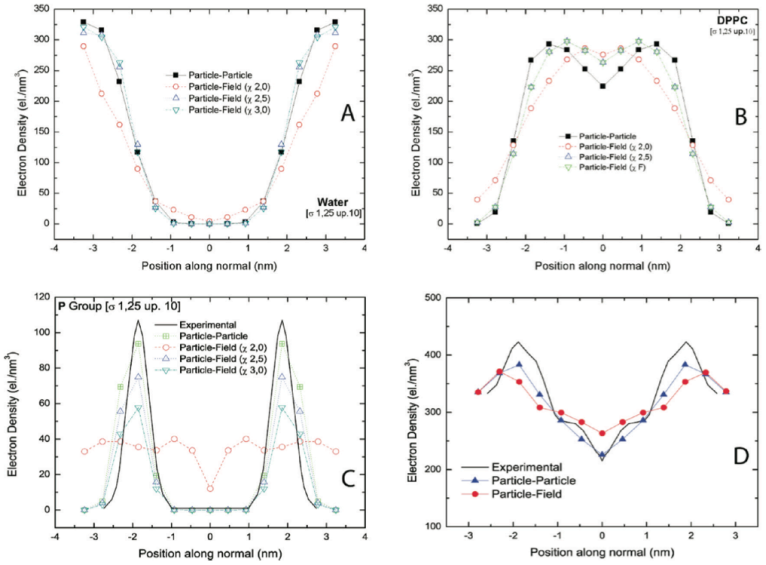

Figure 4-3. Comparison between reference PP and PF simulations using different values of the χ_{CW} parameter for electron density profiles of water (A), DPPC (B), and the phosphate group (C). Total density profiles for DPPC water system calculated from PP (red circles) and PF (blue triangles) simulations in comparison with experiments (black curves; D) are shown. The density profiles evaluated using the χ_{CW} parameter, which is scaled 2 to 3 times the value obtained from Eq. (1), are compared with those of the reference PP simulation.

From Figure 4-3, it is clear that using a value of the χ_{CW} parameter that is 2.5 times larger than that evaluated by Eq. (1) gives electron density profiles very close to that in the reference PP simulations. In Figure 4-3D, the total electron

density profiles of the DPPC/water system calculated from PP and PF simulations are compared with those obtained by fitting X-ray diffraction experiments of Kucerka and co-wokers[30]. The behavior of the calculated density profiles is smoother than the experimental one. In particular, in both PP and PF density profiles, the height of the peaks located at about 2 nm from the center of the bilayer is slightly underestimated. This effect, similar in PP and PF simulations, can be ascribed more to the coarse-grained nature of the models (reduction of degrees of freedom into one effective bead) than to the field description in the hybrid PF models; a similar behavior is found comparing the behavior of the calculated and experimental density profiles for the phosphate group (Figure 4-3C). The optimized set of χ parameters for all PF interactions is reported in Table 4-2.

According to Eq (1), the interaction matrix is symmetric, and the χ parameter between the same type of particles is zero.

In Figure 4-4, self-assemblies of DPPC/water systems simulated using PP and PF models are compared. For simulations, the initial configuration and the simulation conditions are the same (see Table 4-1). The starting configuration for both simulations is made up of randomly mixed DPPC and water molecules.

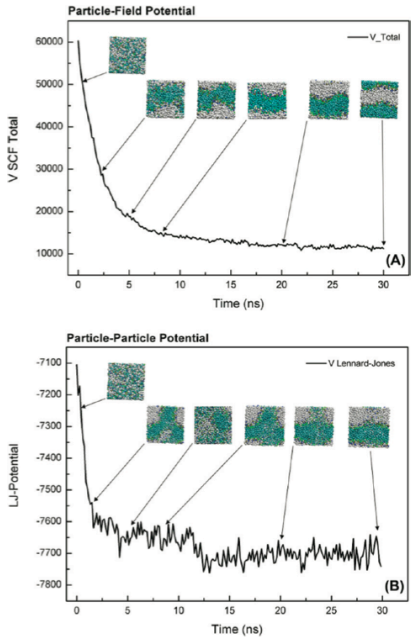

Figure 4-4. Comparison of the self-assembly process of DPPC and water in a bilayer phase obtained from PF (A) and PP simulations (B). In the figure, the time behavior of particle-field intermolecular potential in the PF MD simulation is compared with the behavior of the non-bonded Lennard Jones potential in the PP simulation. Potential units are kilojoules per mole.

It is worth noting that in the PF simulations the formation of the lipid bilayer as stable equilibrium state, as shown by the snapshots reported in Figure 4-4A, is observed already after about 7 ns. From Figure 4-4B it can be noted that in the same time interval the PP simulation shows only an initial stage of phase separation and a stable lipid bilayer phase is formed only after 30 ns.

4-3.1 Structural Properties

As described in Chapter 2, coarse-grained density fields $\phi_K(\boldsymbol{r})$, obtained from particle positions for every particle type K, are used to calculate PF potentials and forces.

According to the scheme described above, two parameters, the cell size l and the update frequency Δt_{update}, regulate the degree of coarse-graining of the density fields. Larger cell sizes lead to more collective density fields. As for the value of the update frequency, it has to be chosen in a way that the approximation of slow variation of the field with respect to the particle displacement is valid between two density updates. In this section, simulation results using different density update frequencies and cell sizes will be discussed and compared with the results of reference PP simulations.

Several test simulations have been performed to understand

the effect of the cell size l on the quality of calculated electron density profiles of the DPPC water bilayer. In Figure 4-5, partial density profiles corresponding to water and to the four different bead types (N, P, G, and C) present in DPPC obtained using l ranging from 1.25 and 2.5σ (corresponding to 0.59 and 1.17 nm) and using the same update frequency (Δt_{update} = 10 timesteps) are reported.

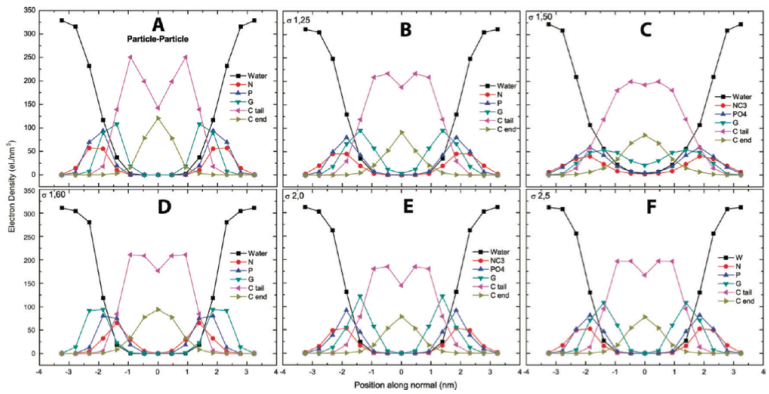

Figure 4-5. Partial density profiles for water and DPPC obtained from (A) PP simulations and PF simulations using *l*=(B) 1.25σ, (C) 1.50σ, (D) 1.60σ, (E) 2.0σ, and (F) 2.5σ. In all PF simulations, the update frequency Δt_{update} is 10 time steps.

From Figure 4-5 it is clear that PF simulations reproduce the structure of the lipid bilayer phase obtained from reference PP simulations well (Figure 4-5A). Values of l larger than 2.5σ give rise to stronger phase separation between water and DPPC with a narrowing of the density profiles. The grid size is larger, and this effect is more pronounced.

In Figure 4-6, electron partial density profiles for a mixture of water and DPPC molecules obtained for different values of the density update and using the same grid size (l = 1.25 σ) are compared with those obtained from reference PP simulations. In particular, the behaviors for Δt_{update} ranging from 10 (0.3 ps) to 1300 (39 ps) time steps are compared.

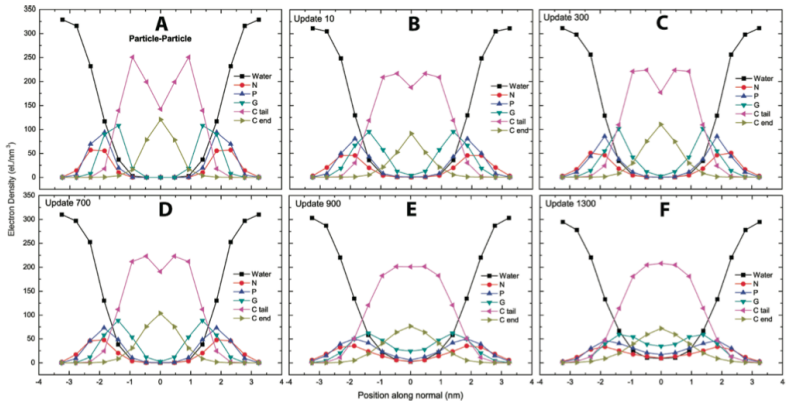

Figure 4-6. Partial density profiles for water and DPPC obtained from (A) PP simulations and PF simulations using Δt_{update} = (B) 10, (C) 300, (D) 700, (E) 900, and (F) 1300 time steeps. In all PF simulations, the grid size has been kept constant at l=1.25σ.

As expected, the agreement between PP and PF density profiles worsens as the Δt_{update} grows. For an update frequency between 10 and 700 time steps, water and DPPC density profiles are quite similar (see Figure 4-6B_D) and reproduce the behavior of the reference PP simulation well. Starting from update frequencies of 900 time steps (see Figure 4-6E), artificial undulations in the lipid bilayers are obtained.

This causes a smoothing of the calculated density profiles. In particular, when large updates are used, the central depletion in the density profile of the hydrophobic beads of type C is absent (Figures 4-6E,F). Further- more, the density profiles of the DPPC head groups N and P and of the bead types G are very shallow (Figure 4-6E,F).

The reproduction of the spatial organization of the head groups and in particular the phosphate group (type P) is important for the quality of the model. In fact, the bilayer thickness (D_{HH}), obtained by calculating the distance between the two peaks of the density profile corresponding to the phosphate group, can be compared with the values obtained from X-ray and/or neutron diffraction measurements. In the case of DPPC at 323 K, a value of D_{HH} of 3.7 nm is obtained from PF simulations using update frequencies from 10 to 700 time steps. This value is equal to the one obtained from PP simulations and close to the experimental value of 3.8 nm measured at the same temperature[31]. For larger values of density update frequency, the electron density profile of P groups becomes broader, and a correct evaluation of D_{HH} becomes unreliable.

In order to understand the behavior of the systems as a function of the frequency of the density update, it is useful to compare the mean square displacement (MSD) of the particles

as a function of time. In Figure 4-7, we present the behavior of the square root of the mean square displacement for water and the DPPC in units of cell length ($(MSD)^{1/2}/l$ where l is the cell length) as function of time for different values of update frequencies.

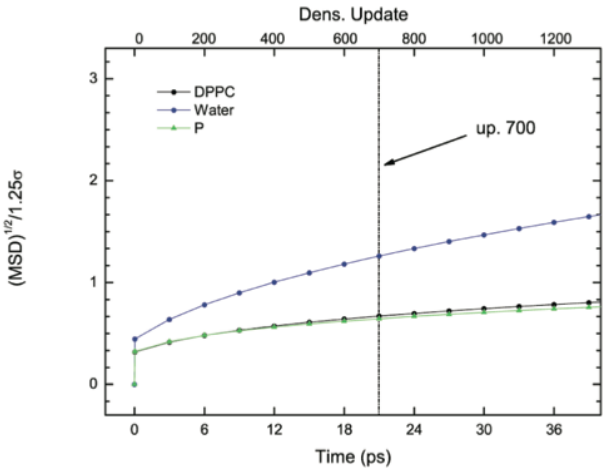

Figure 4-7. Normalized displacement of water, DPPC, and P beads as a function of time.

This is a direct way to understand the validity of the approximation of slow variation of the field with respect to the particle displacement between two density updates. In fact, the plot of Figure 4-7 quantifies how many cells a particle can cross in a given amount of simulation time. From Figure 4-7, it is clear that for update frequencies between 500 and 700 steps (corresponding to 15 and 21 ps) both water and DPPC beads have a displacement smaller than or equal to the

cell size. For larger update time intervals, the displacement is larger than the size of a cell. This result agrees well with the good reproduction of density profiles and a bilayer thickness for update frequencies smaller than 700 steps.

This kind of analysis of PF simulations can be useful in general to set a suitable value for the update frequency also in the absence of reference simulations data.

4-3.2 Dynamical Properties

From the comparison of the self- assembly processes of a lipid bilayer obtained in the simulations shown in Figure 4-4, it is clear that the dynamics of the system simulated by the PF method are faster. This is due to smoother potentials and forces characterizing the PF Hamiltonian. In particular, PF models include the effect of excluded volume interactions between particles using the incompressibility condition described in Eq (14) of the Chapter 2. Forces acting on the particles then depend on the derivatives of the density fields that change smoothly over the length scale at larger than average distances between particle pairs.

In order to compare more quantitatively the different dynamics in PP and PF simulations, diffusion coefficients have been calculated from the MSD behaviors of water and

DPPC particles as functions of time.

In Figure 4-8, values of the ratio D^* between the diffusion coefficients calculated from the PF simulations using different update frequencies and the one calculated from the reference PP simulation are reported. In all of the cases and for both water and DPPC, the diffusion coefficients calculated from the results of PF simulations are larger than those obtained from the results of the PP simulation.

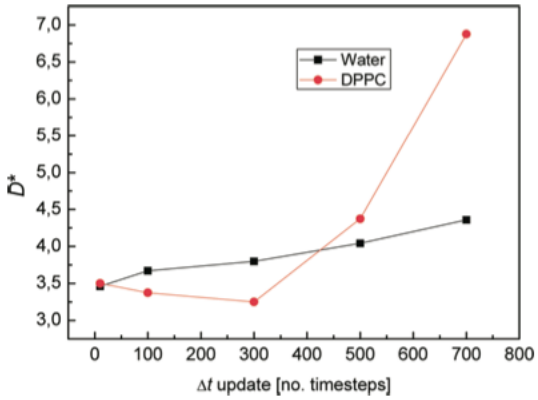

Figure 4-8. Ratio between PP and PF diffusion coefficients as a function of the update frequency calculated for water (black curve) and DPPC (red curve).

The diffusion of water is 3.5 to 4 times faster for PF simulations. The increase of the diffusion coefficient of the DPPC lipid ranges from about 3.5 to 7 times the value obtained from the reference PP simulation. This behavior is in agreement with the faster formation of a stable lipid bilayer as obtained from the comparison between PF and PP simulations

reported in Figure 4-4.

In Table 4-3, the values of diffusion coefficients and their components calculated from PP and PF simulations using different density update frequencies are reported.

Results of the test simulations obtained using different grid sizes l and the same update frequency (300 time steps) are reported in Figure 4-9. In particular, the values of the diffusion coefficients of water and DPPC increase according to the increase in the grid size. This is reasonable because a coarser density will give rise to smoother particle-field potentials and forces.

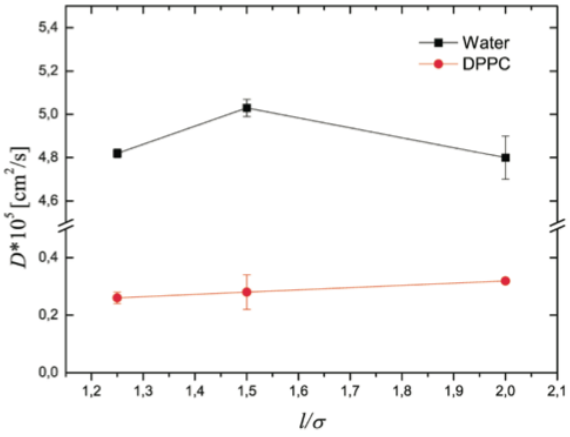

Figure 4-9. Diffusion coefficients of water and DPPC *vs.* the CG density grid size.

In the case of water, there is a small decrease in the diffusion coefficient for the largest grid sizes (2.0σ). This effect is due to the deviation from the reference density profile obtained

when a larger grid size is used. As described in the previous paragraph, large grid sizes give rise to stronger phase separation between water and DPPC. The *x* and *y* components of the diffusion tensor of the water parallel to the bilayer plane show small variation as a function of the grid size, and they are practically constant within the error bar. In contrast, the *z* component of the diffusion tensor of water going from a grid size of 1.5 to 2.0σ is reduced by a factor of 2.

4-3.3 Extension to other Phospholipids

One of the advantages of our reference PP coarse-grained model is that the parameterization of the interaction potentials is not tailored to a specific lipid, and different phospholipids can be modeled, taking into account different chemical structures, using a small set of bead types.

In this section, simulations aiming to test the transferability of the model developed for DPPC and the relative PF $\chi_{KK'}$ parameters are reported. Electron density profiles and bilayer thickness are compared between PF and PP models and with experiments.

In particular, further test simulations are conducted for three biologically relevant lipids, i.e. dimyristoyl-phosphatidylcholine (DMPC), distearoyl-phosphatidylcholine

(DSPC), and dioleoylphosphatidylcholine (DOPC). In Figure 4-10, the chemical structures of these three phospholipids are shown along with the structure of DPPC.

The advantage of our reference PP coarse-grained models lies in the straightforward way in which the corresponding atomistic structure can be represented.

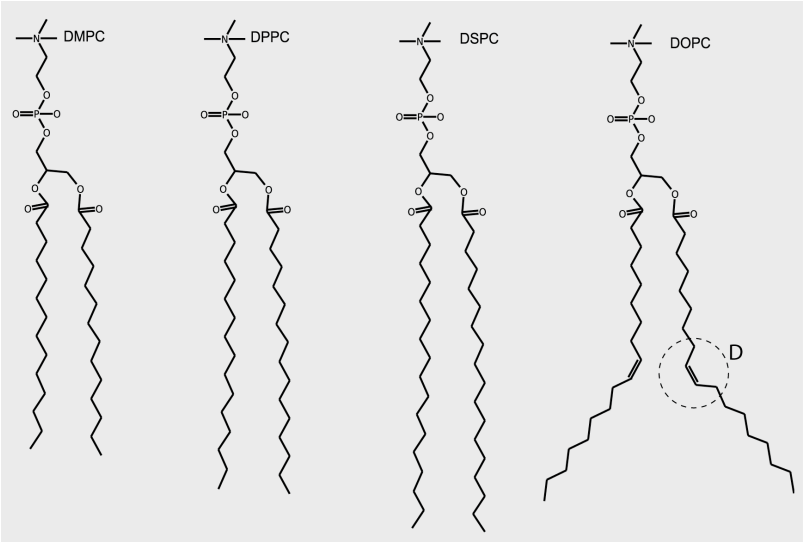

Figure 4-10. Structure formulas of the four phospholipids considered in the present study. The mapping scheme adopted for the CG models is the one depicted in Figure 4-1. For the DOPC phospholipid, the mapping for beads of type D including carbon atoms involved in double bonds is shown.

The differences between lipids depend on the molecular structure on the atomistic level. For instance, the main difference between DMPC, DPPC, and DSPC is in the numbers of carbon atoms present in the hydrophobic tails. In this case, at the CG level, the PP models differ only in the

number of beads of type C (see Figures 4-1 and 4-10) that compose the tails, while the parameters for the nonbonded bond and angle potentials are the same. Differently, in the case of DOPC, the presence of a double bond in each hydrophobic chain requires an extra particle type corresponding to four atoms including a double bond (see Figure 4-10, particle type D). For this reason, in the DOPC CG model, some of the angles and nonbonded potentials are different. In particular, the C-C-C harmonic angle potential has a minimum at 180°, while the C-D-C harmonic angle potential has a minimum at 120°. In the same way, nonbonded interactions of beads of types C and D are different.

Correspondingly, the particle-field models of DMPC, DPPC, and DSPC have the same bonded, intramolecular nonbonded, and the χ (see Table 4-2) parameters, and they differ only in the number of beads. In the case of DOPC, having an extra bead type D and particle-field interactions involving only this new bead type introduces the use of different χ parameters. Of course, the interactions involving beads of type C are treated in the same manner as in DMPC, DPPC, and DSPC lipids.

Other details about simulated systems are reported in Table 4-1. Simulation temperatures have been chosen according to the available experimental data; temperatures of both experiments and simulations are listed in Table 4-4.

From these simulations, total electron density profiles and bilayer thicknesses (D_{HH}) have been calculated and compared with those of the reference PP simulations and available experimental data. In Table 4-4 the calculated values of D_{HH} are reported together with the reference PP simulations and experimental data. We want to stress that experimental values of D_{HH} lie in a very narrow range going from the smallest value of 3.6 nm for DPPC to the largest one of 4.0 nm for DSPC, and good reproduction of these values can be proof of the transferability of the chosen PF model. As previously discussed, DSPC and DOPC give very similar density profiles with both PP and PF models. This leads to the calculation of the same values of D_{HH} = 4.1 nm for these two lipids using PP models. Using PF models, according to the experimental trend, a larger value is obtained for the D_{HH} of DSPC (4.4 nm) and a smaller one for DOPC (4.0 nm).

In Figure 4-11, the total electron density profiles obtained by Kucerka et al. from X-ray scattering data for DOPC[32] and DMPC[33], the ones obtained from PP and PF simulations, are plotted. In particular, the behavior of electron density of DOPC and DMPC is compared. As already found for DPPC (see Figure 4-3D), the behavior of the calculated density profiles is smoother than the experimental ones. Furthermore, for DOPC, the position of the maximum of electron density

profile of both PP and PF is shifted of about 0.5 nm. This is consistent with an overestimation of the D_{HH} (4.1 and 4.0 nm for PP and PF, respectively) with respect to the experimental value of 3.6-3.7 nm. For DMPC, the position of the maximum of the electron density profile of both PP and PF simulations is similar to the experimental one. In this case, the experimental value of D_{HH} is well reproduced (see Table 4-4).

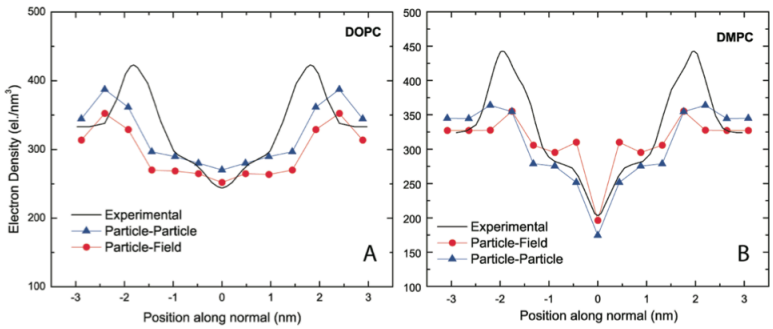

Figure 4-11. Total electron density profiles for (A) DOPC and (B) DMPC phospholipid bilayers.

4-3.4 Simulation Details

Classical MD simulations used to obtain reference PP simulations have been performed using the program GROMACS (ver. 3.3). The time step used for the integration of the equations of motion was 0.03 ps. The temperature and pressure were kept constant using Berendsen's weak coupling

method (τ_T = 0.1 ps and τ_P = 1 ps). Target temperatures have been chosen according to the available experimental data and are listed in Table 4-1. A cutoff of 1.5 nm has been used to truncate nonbonded interactions. To equilibrate the system with *NPT* simulations, the target pressure was fixed to 1 bar, and semi-isotropic coupling has been employed. In order to achieve a better comparison between the results of PP and those of *NVT* PF simulations, *NVT* MD simulations have been performed using the average box lengths (see Table 4-1) obtained from the equilibrated *NPT* simulations. In particular, *NPT* simulations were performed for all systems for at least 120 ns. In the case of the DPPC lipid, the equilibrium area/lipid at 323 K for the PP model is 0.64 nm^2. This value was reported by Marrink et al.[34] and is in agreement with the experimental value reported by Nagle et al.[35] and later by Kucerka et al.[30] In order to simulate systems having a correct value of area/lipid, *NVT* PF simulations have been performed using average box lengths (see Table 4-1) that are corresponding to those obtained in the reference PP simulations.

The molecular dynamics program OCCAM[36] was used for hybrid particle-field MD simulations. PF simulations have been performed using a time step of 0.03 ps. *NVT* simulations have been conducted keeping the temperature constant using

an Andersen thermostat with a collision frequency of 5 ps^{-1}. All density profiles, for both PP and PF simulations, have been calculated from simulations equilibrated at least for 10 ns. Density profiles have been averaged over further 2 ns after equilibration. The composition of lipid water systems has been set in the range of stability of the bilayer phase. Details about systems sizes and compositions are summarized in Table 4-1.

Table 4-1. Details about Simulated Systems

Lipid Type	Box length[a] (nm)			Composition		
	x	***y***	***z***	**No. of lipids**	**No. of CG water**	**T (K)**
DPPC	8.18	8.18	6.95	208	1600	325
DMPC	6.60	6.60	9.47	208	1600	303
DOPC	7.21	7.21	9.63	208	1600	303
DSPC	8.03	8.03	7.76	208	1600	335

[a]values of box length in *x*, *y*, and *z* directions have been fixed using averages obtained from *NPT* simulations of the reference PP models.

Table 4-2. Particle-Field Interaction parameters

χ	N	P	G	C	W
N	0.00	-1.50	6.30	9.00	-8.10
P	-1.50	0.00	4.50	13.50	-3.60
G	6.30	4.50	0.00	6.30	4.50
C	9.00	13.50	6.30	0.00	33.75
W	-8.10	-3.60	4.50	33.75	0.00

$\chi_{K'} \times RT$ (kJ/mol) for particles of type K interacting with fields due to particle of type K'.

Table 4-3. Diffusion coefficients calculated using different Update Freq.[a]

Update Freq. [timesteps]	**Water ($cm^2/s \times 10^5$)**				**DPPC ($cm^2/s \times 10^5$)**			
	Total	***x***	***y***	***z***	***Total***	**x**	**y**	**z**
PP	1.27	1.63	1.63	0.43	0.08	0.13	0.12	0.01
10	4.40	6.5	6.6	0.04	0.28	0.45	0.43	0.03
100	4.67	7.1	6.8	0.04	0.27	0.43	0.44	0.03
300	4.82	7.3	7.1	0.04	0.26	0.38	0.38	0.04
500	5.13	7.6	7.6	0.05	0.35	0.52	0.50	0.03
700	5.53	8.4	8.4	0.05	0.55	0.079	0.078	0.09

[a]The grid size l is equal to 1.25σ for all simulations.

Table 4-4. Calculated Bilayer Thickness

Phospholipid	**D_{HH} PP** (nm)	**D_{HH} PF** (nm)	**D_{HH} Experimental** (nm)
DMPC	3.7 (303 K)	3.7 (303 K)	3.8[37]-3.5[33] (303 K)
DPPC	3.5 (323 K)	3.5 (323 K)	3.6[37] (323 K)
DOPC	4.1 (303 K)	4.0 (303 K)	3.7[37]-3.6[32] (303 K)
DSPC	4.1 (333 K)	4.4 (333 K)	4.0[37]-4.1[38] (333 K)

4-4 Particle-Field CG Model of Phospholipids in Non-lamellar Phase.

In this section the validation of particle-field models of phospholipids in non bilayer phases is reported. In particular, the transferability of the model to systems different water contents has been validated against reference simulations.

4-4.1 Simulation Details

For the use of a reference system for the CG simulations, classical PP MD simulations have been performed using the program GROMACS[39] (ver. 3.3). The timestep used for integration of equation of motion was 0.03ps. The temperature was kept constant using the weak coupling method with τ_T=0.1 ps, where the target temperatures are listed in Table 4-2. A cut-off of 1.5 nm has been used to truncate the non-bonded interactions.

The parallel molecular dynamics program OCCAM[36] was used for PF MD simulations. PF MD simulations have been performed using a timestep of 0.03ps with the *NVT* ensemble by keeping the temperature constant using Andersen thermostat with a collision frequency of $5ps^{-1}$.

Details on the systems size and composition used in the simulations in the present study are summarized in Table 4-5.

Table 4-5. Composition of systems used to investigate phases different from lamellar one.

System	**Box Size** (nm)	**Composition**				***T*** (K)
	x=y=z	**No. of Particles**	**No. of DPPC**	**No. of Water**	**Water/DPPC[a] Ratio**	
1	7.923	3,876	20	3,636	182	325
2	8.176	4,096	320	256	0.8	325
3	12.964	21,216	1,664	1,248	0.75	318
4	13.486	24,128	1,664	4,160	2.5	318
5	12.376	18,600	300	15,000	50	318
6	17.309	42,588	208	40,092	192.7	318

[a]In the reference PP model each CG water bead corresponds to 4 molecules, in the text of the manuscript and in the figures this factor has been taken into account.

4-4.2 Model Validation: PP vs. PF simulations

According to the coarse-graining strategy explained in the section 4-2, pair interactions between particles are replaced by the calculation of the interactions of single particles in an external field. In principle, coarse-grain parameters are not always transferable, in particular, χ parameters can be temperature and composition dependent. This dependency cannot be known *a priori* and needs to be investigated for

every coarse-grained model. This feature of coarse-grained models is general and is relevant also for particle-particle coarse-grained models.

In order to validate the PF MD-SCF simulations, the results between PF and PP simulations are compared.

In Figure 4-12 self assemblies of DPPC/water systems simulated using PP and PF models at two different water contents (systems **1** and **2** of Table 4-5, respectively) are compared. In the reference PP model each CG water bead corresponds to 4 real water molecules. In the present study, this factor has been taken into account. For example, ratio between CG water beads and DPPC molecules reported in table 4 is for system **1** is 182 and for system **2** is 0.8. In terms of real water molecules these ratios would be 728 and 3.2.

For both of these simulations the initial configuration and the simulation conditions are the same. The starting configuration used in both simulations is a random mixture of DPPC and water molecules. For high water concentration (system **1**), for PP and PF simulations, the formation of a micelle is observed.

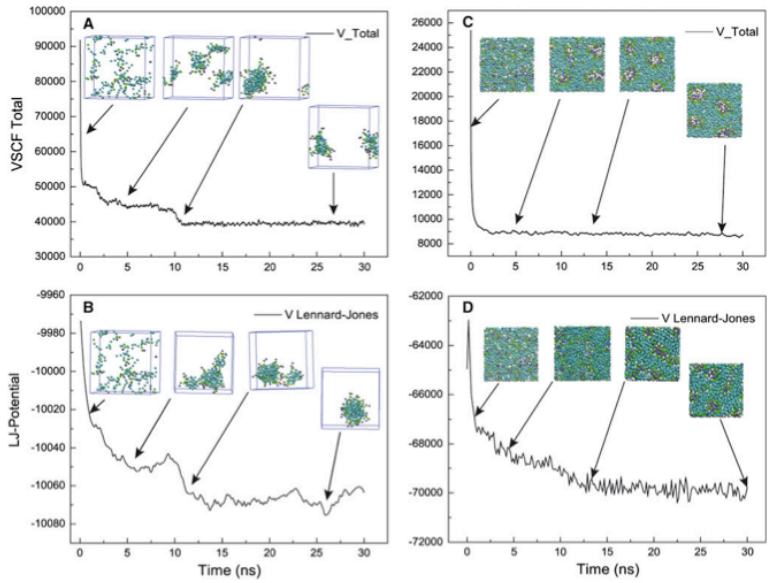

Figure 4-12. Comparison of the self assembling process of a DPPC micelle in water for PF (A) and PP simulations (B). Comparison of self assembling process of a reverse micellar phase for PF (C) and PP simulations (D) is given. In the figures the time behavior of particle-field intermolecular potential in the PF MD simulation are compared with the behavior of the non-bonded Lennard-Jones potential in the PP MD simulation. Potential units are kJ/mol.

In the case of PF simulation the self assembling process of the micelle takes about 15 ns, which is faster than the PP simulation (see Fig. 4-12A), where the micelle is obtained after 25ns (see Fig. 4-12B). In Figure 4-13 the radial density profiles of the micelle obtained in the PF (Fig. 4-13A) and PP (Fig. 4-13B) simulations are compared.

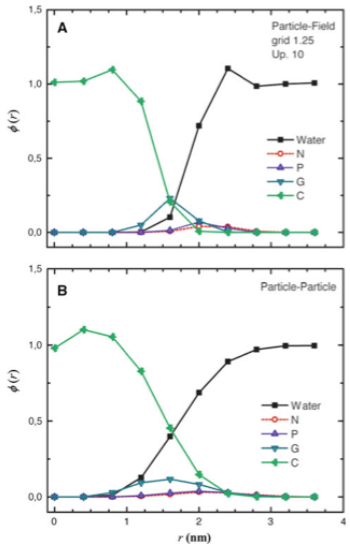

Figure 4-13. Radial density profiles of the micelle obtained in the PF (A) and PP (B) simulations on system **1**.

Radial density profiles obtained in the PP and PF simulations are similar. The main difference is observed in the slopes of the curves. A further validation of the proposed particle-field models can be done calculating the average number of lipid per micelle. These calculations can be reliable only using larger systems in which two more micelles are in equilibrium with free lipid molecules.

The system at low water concentration (system **2**) shows a different behavior; in both PP and PF simulations a formation of reverse micelles is observed. In particular, from Fig. 4-12C it is clear that at about 12ns the system reaches a stable reverse micellar phase. In this reverse micellar phase, polar

head groups of the lipids and the water molecules form cylinders included in the hydrophobic majority phase made of lipid tails. This result is in agreement with the formation of a hexagonal reverse-cylindrical phase. The formation of this phase structure is more clearly observed in Fig. 4-14A where structures obtained from PF and PP simulations are compared. Differently from PF simulations, the cylinders obtained in the PP simulation are less regular and the water beads are not included in the cylinders but they form clusters with different sizes inside the hydrophobic phase formed by the lipid tails. We expect that, in this case, the simulated system is "trapped" in a metastable phase and the slower dynamics of PP simulations does not allow the system to escape from such a metastable phase to become more stable hexagonal structure. In order to confirm this point, the equilibrium structure obtained in the PF simulation is used, after a short energy minimization is performed, as the initial state for the PP simulation.

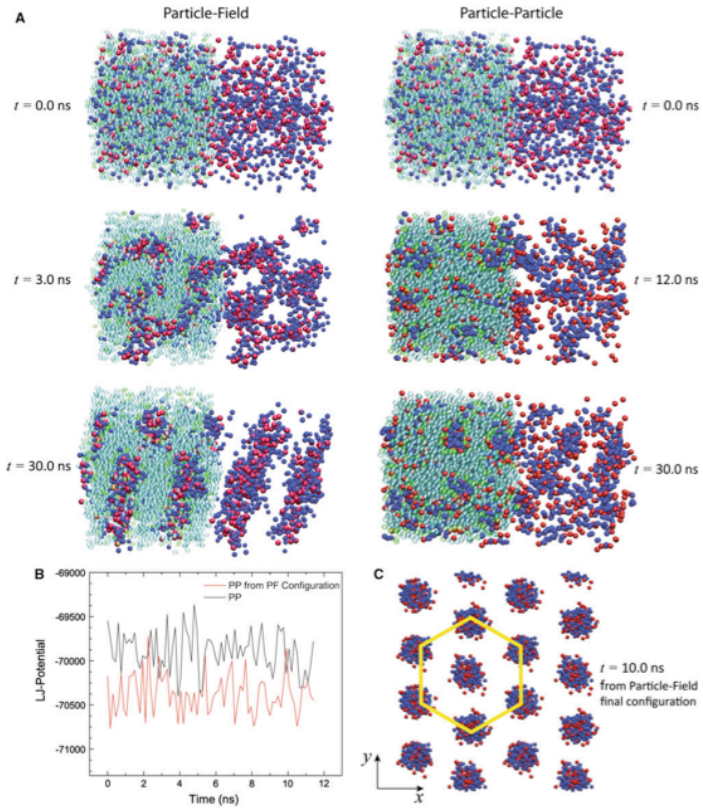

Figure 4-14. Comparison of self-assembling process of cylinders in the reverse micellar phase obtained in the PF and PP simulations (A). Comparison between time behavior of Lennard-Jones non-bonded potential (kJ/mol) of PP simulations obtained in a spontaneous assembling process from a uniformly mixed state (black curve) and that of PP simulation starting from the self-assembled structure obtained in the PF simulation (red curve) (B). Snapshot of the system showing the hexagonal arrangement of cylinders in the reverse micellar phase (C).

In this case, as shown in Fig. 4-14B the non-bonded interaction energy is lower and the structure is stable during all the simulations. In Figure 4-14C this structure is depicted in a view showing the hexagonal arrangement.

4-4.3 Effects of Density Coarse Graining on Structure and Dynamics

According to the theoretical formulation described in Chapter 2, two parameters, i.e. the cell size l and the update frequency Δt_{update}, regulate the degree of coarse-graining of the density fields. Larger cell sizes lead to more collective density fields. As for the value of the update frequency, it has to be chosen in a way that the approximation of slow variation of the field with respect to the displacements of the particles is valid between two density updates.

In Figure 4-15 the structures obtained using different density update frequencies and cell sizes are summarized. In particular, for high and intermediate water concentrations the formation of a micelle and lipid bilayer is always observed using large values of field update interval (up to 900 timesteps) and the grid size (up to 2.5σ = 1.175 nm). Differently, the hexagonal phase expected at low water concentration can be obtained for grid sizes smaller than 2σ ($l \approx$ 1 nm) and update interval shorter than 500 timesteps. For larger values of the update interval or of the grid size, the cylinders are not formed and instead irregular reverse micelles are obtained as shown in Figure 4-15 (labeled as *im*).

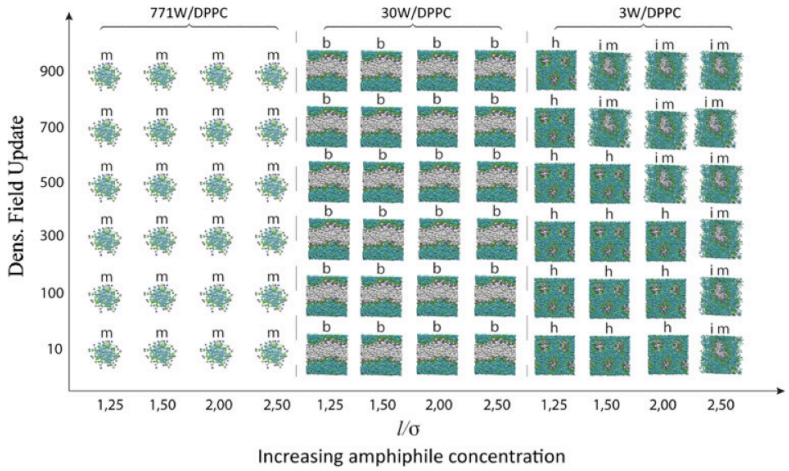

Figure 4-15. Graphical matrix summarizing the structures obtained using different density updates intervals (*y* axis, time steps unit) and cell sizes *l* (*x* axis, unit of σ).

This behavior can be explained by comparing the size of the grid with the lengthscale of the self-assembling structure. The diameter of the micelle and the bilayer thickness are both about 4 nm, while the diameter of the tubes present in the hexagonal phase is smaller (≈ 1 nm). Then in this case when the size of the grid used for the density coarse-graining starts to approach the size of the cylindrical tubes, these structures cannot be described correctly. Similar considerations can be made for the density update interval. In figure 6 is reported the behaviour of the mean square displacement as a function of time for different values of the density update intervals for the two different systems reported in Figure 4-12. In particular, in order to compare the displacements with the size

of the structures, the square root of the mean square displacement (MSD) normalized by the grid size is reported.

This is a quantitative way to understand the validity of the approximation of slow variation of the field with respect to the particle displacement between two density updates. In fact the plots showed in Figure 4-16 quantify how many cells a particle can across in a given amount of simulation time.

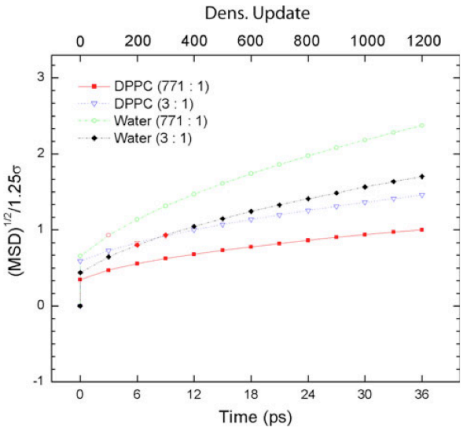

Figure 4-16. Square root of normalized the mean square displacement of water, DPPC and water beads as function of time.

From Figure 4-16 it is clear that for update intervals between 500 and 900 steps (corresponding to 15 and 36 ps) both water and DPPC beads undergo a displacement equal to or larger than a cell size (i.e. larger than 0.6 nm).

From the comparison of the self assembling processes obtained in the simulations shown in Figure 4-12, it is clear

that the dynamics of the system simulated in the PF method is faster than the PP method. This is due to the smoother potentials and forces characterizing the PF Hamiltonian. In particular, the models used in the PF simulation include the effect of excluded volume interactions between particles by using incompressibility condition as described in Eq. (14) of Chapter 2. Then, forces depend on the derivatives of the density fields with a change much more smoother than distances between particles pairs.

In order to compare more quantitatively the different dynamics in PP and PF models, diffusion coefficients have been calculated from the behaviour of the MSD for water and DPPC particles versus time. In particular in Figure 4-17 the ratio D^* between diffusion coefficients calculated in the PF simulations (update interval of 300 timesteps and grid size $l = 2.0\sigma$) and the one calculated in the reference PP simulation are reported. From the figure it is clear that for all considered systems the diffusion coefficients calculated in the PF simulations are always larger than ones calculated in the PP simulations. In particular, for DPPC they are from 4 to 6 times larger than those in the PP simulations and for water they are from 1.25 to 2.5 larger.

Absolute values of diffusion coefficients calculated using different grid sizes and update interval for both water and

DPPC are reported in tables 4-6 to 4-9.

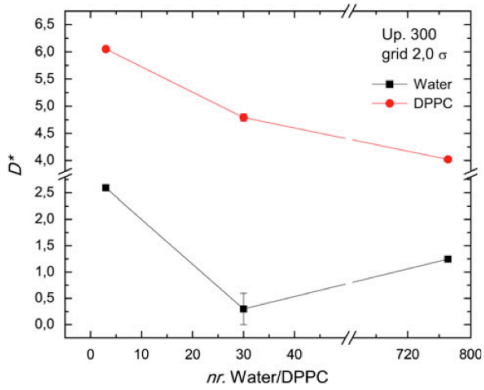

Figure 4-17. Ratio between PF and PP diffusion coefficients as function of water/DPPC ration calculated for water (black curve) and DPPC (red curve).

The ratios between the diffusion coefficients obtained in the PF and PP simulations can be regarded as scaling factors to connect the dynamics of the PF simulations with that of the reference PP ones. This kind of comparison has been made also for the reference PP simulations to connect their dynamics with atomistic ones and according to this comparison we can estimate that the reference PP models have a dynamics that is about 4 times faster than atomistic simulations. Considering this point, the dynamics in PF simulations should about 20-25 times faster than that in the atomistic simulations. It is interesting to note that the scaling factors between the PP and PF simulations are functions of water concentrations. In particular, they become larger as the

water content becomes smaller. This behaviour, from practical purposes, is very convenient because we can simulate with a largely improved efficiency the very slow dynamics in atomistic systems whose equilibration is difficult with the PP coarse-grained or the atomistic simulations.

Table 4-6. Diffusion coefficients calculated using different update intervals and different grid sizes for water in system **1**

Update Freq.	**Water**			
[time steps]	[$cm^2/s \times 10^5$]			
	l* = 1.25 *σ	***l* = 1.50 *σ***	***l* = 2.0 *σ***	***l* = 2.5 *σ***
Particle-Particle	2.45 ± 0.06	-	-	-
10	3.04 ± 0.06	3.02 ± 0.02	3.04 ± 0.02	2.93 ± 0.07
100	3.06 ± 0.07	3.07 ± 0.01	2.9 ± 0.1	2.94 ± 0.06
300	3.05 ± 0.01	3.12 ± 0.02	3.05 ± 0.05	3.04 ± 0.03
500	3.15 ± 0.03	3.18 ± 0.05	3.08 ± 0.04	3.06 ± 0.01
700	3.23 ± 0.02	3.02 ± 0.05	3.12 ± 0.05	3.08 ± 0.05

Table 4-7. Diffusion coefficients calculated using different update intervals and different grid sizes for DPPC in system **1**

Update Freq.	**DPPC**			
[timesteps]	[$cm^2/s \times 10^5$]			
	$l = 1.25\ \sigma$	$l = 1.50\ \sigma$	$l = 2.0\ \sigma$	$l = 2.5\ \sigma$
Particle-Particle	0.024 ± 0.003	-	-	-
10	0.085 ± 0.004	0.090 ± 0.003	0.132 ± 0.002	0.093 ± 0.001
100	0.12 ± 0.01	0.118 ± 0.008	0.091 ± 0.002	0.992 ± 0.008
300	0.09 ± 0.02	0.12 ± 0.04	0.14 ± 0.05	1.01 ± 0.03
500	0.076 ± 0.004	0.14 ± 0.02	0.089 ± 0.003	1.03 ± 0.03
700	0.089 ± 0.006	0.088 ± 0.003	0.096 ± 0.001	1.14 ± 0.09

Update Freq. **Water**

[timesteps]	[$cm^2/s \times 10^5$]			
	l* = 1.25 *σ	***l* = 1.50 *σ***	***l* = 2.0 *σ***	***l* = 2.5 *σ***
Particle-Particle	0.3813 ± 0.0007	-	-	-
10	1.02 ± 0.06	0.85 ± 0.02	0.98 ± 0.05	1.42 ± 0.02
100	0.957 ± 0.005	0.61 ± 0.08	0.84 ± 0.06	1.61 ± 0.04
300	0.88 ± 0.09	0.90 ± 0.07	0.6 ± 0.3	1.36 ± 0.06
500	0.87 ± 0.08	0.8 ± 0.2	0.859 ± 0.003	1.02 ± 0.04
700	1.07 ± 0.04	0.46 ± 0.03	0.936 ± 0.008	1.340 ± 0.007

Table 4-8. Diffusion coefficients calculated using different update intervals and different grid sizes for water in system **2**

Table 4-9. Diffusion coefficients calculated using different update intervals and different grid sizes for DPPC in system **2**

Update Freq.	**DPPC**			
[timesteps]	[$cm^2/s \times 10^5$]			
	l* = 1.25 *σ	***l* = 1.50 *σ***	***l* = 2.0 *σ***	***l* = 2.5 *σ***
Particle-Particle	0.032 ± 0.002	-	-	-
10	0.12 ± 0.01	0.14 ± 0.02	0.20 ± 0.01	0.24 ± 0.05
100	0.132 ± 0.002	0.148 ± 0.004	0.196 ± 0.004	0.24 ± 0.01
300	0.135 ± 0.002	0.155 ± 0.008	0.183 ± 0.001	0.25 ± 0.01
500	0.153 ± 0.007	0.158 ± 0.002	0.16 ± 0.02	0.24 ± 0.01
700	0.16 ± 0.01	0.156 ± 0.003	0.186 ± 0.001	0.25 ± 0.04

4-4.4 Simulations on Larger Systems

On the basis of the results presented in the previous subsection, PF MD simulations on larger systems have been performed using a grid size l=1.5σ and the density update interval of 300 timesteps. In particular, we simulated the spontaneous self-assembling processes in several DPPC/water systems for 1.2μs using a cubic box with the side lengths that are about double of those used in the simulations reported in the previous subsections. For all considered systems the starting configuration is made up of randomly mixed lipid and water molecules.

In Figure 4-18 the time behaviors of PF potential together with some snapshots for four DPPC/water systems at different water concentration have been shown (systems **4-6**), while the details of these systems are shown in Table 4-5.

For all of the systems shown in Figure 4-18 after 500ns the equilibrium is achieved and a stable phase-separated structure is formed. In particular for the system at lower water concentration shown in Figure 4-18A (system **3**, 3 water/lipid) after 400 ns a stable reverse hexagonal phase is formed. At intermediate water content (system **4**, 10 water/lipid) a stable bilayer phase is formed before 500ns (Figure 4-18B).

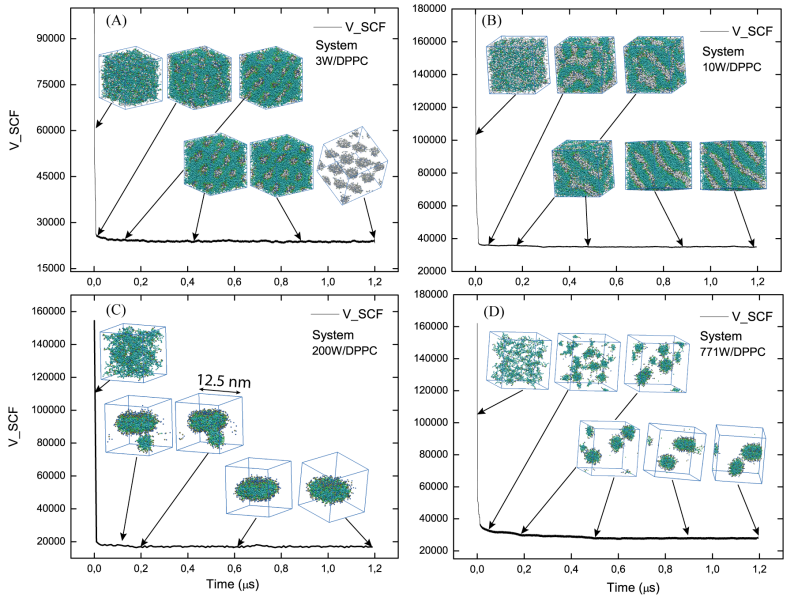

Figure 4-18. Time behaviors of the PF potential together with some snapshots for (A) system **3** forming a reverse-micellar hexagonal phase, (B) system **4** forming a lipid bilayer phase, (C) system **5** forming a single bicelle, and (D) system **6** forming a micellar phase.

Differently, in system 5 (Figure 4-18C), where the water content is higher, after a rapid initial local clustering after 100ns there is a coalescence to a bilayer structure with curved edges (bicelle) leaving a small single spherical micelle beside it. Between 100 and 200ns a process of fusion starts to give a stable bilayer structure with curved edges involving all 300 DPPC molecules present in the simulation box. Finally, the simulation of the system 6 with the water content of 771 water/lipid, after an initial clustering, the formation of two

nearly spherical micelles is obtained.

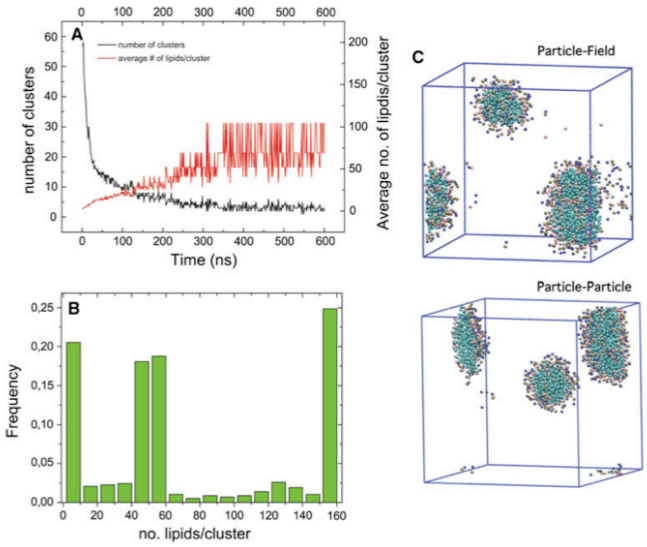

Figure 4-19. Time behaviours of number of clusters (black line) and average number of lipids per cluster/micelle (red line) (A). Number of lipids/cluster distribution system (B) Snapshots of PF and PP micellar systems (C).

A further validation of the proposed models can be done considering the average number of lipids/micelle. In the Figure 4-19A is reported the time evolution of the number of clusters together with the average number of lipid per cluster for a system having 771 water/lipids. Two lipids are considered to be in the same cluster if at least one distance between their beads is smaller than 1.2 nm. According to this choice the average number of lipids/cluster (micelle) is about 80. This value has been averaged starting from 400 ns, when

the system shows to be in equilibrium. As for available experimental data, Sodium dodecyl sulfate (SDS) in physiological conditions forms micelles with an aggregation number ranging from 50 to 80. In Figure 4-19B, the micelle size distribution, averaged from 400 to 600 ns has been also reported. From the figure it is clear that the distribution is trimodal, showing three peaks, the first one corresponding to free lipid molecules, a second one corresponding to a smaller micelle of about 50 lipids and a bigger one of about 150 lipids. This distribution can be also visualized looking at some representative simulation snapshot like the one depicted in Figure 4-19C. Analogous behavior has been found from particle-particle simulations, very similar structures can be obtained as shown in Figure 4-19C.

4-5. Conclusions

Specific CG models for phospholipids and water suitable for hybrid particle field molecular dynamics simulations have been developed. These models and the set of parameters needed to evaluate interactions of particles with density fields are optimized to reproduce structural properties of reference PP simulations. These parameters are transferable also to other phospholipids, different from the DPPC, in the reproduction of lipid bilayer structure properties. The transferability, depending on the temperature and water/lipid content, has been already tested and validated in the reproduction of phases different from the lamellar one. As expected, due to the smoothness of the PF interactions, the dynamics is faster in PF simulations. In particular, the ratio between diffusion coefficients calculated from PP and PF simulations, for the bilayer systems, goes from 3 to 7 depending on the degree of coarse-graining of the density field.

The proposed model is also able to correctly describe morphologies, different from lamellar one, i.e. from micelles (at high water concentration) to reverse micelles (at low water concentration), obtained by varying the water content.

The lower computational costs of the hybrid MD-SCF approach, together with a faster dynamics due to the smoothness of the potentials and forces, enable us to perform simulations with a considerably improved efficiency. The hybrid MD-SCF scheme is particularly efficient in parallel simulations, especially for large systems when the use of a large number of CPUs is efficient.[36]

In conclusion, the development of specific coarse-grained models suitable for hybrid PF simulation opens the way toward the simulation of large-scale systems employing models with chemical specificity.

References:

(1) Venturoli, M.; Sperotto, M. M.; Kranenburg, M.; Smit, B. *Physics Reports-Review Section of Physics Letters* **2006**, *437*, 1.
(2) Marrink, S. J.; de Vries, A. H.; Tieleman, D. P. *Biochimica et Biophysica Acta, Biomembranes* **2009**, *1788*, 149.
(3) Gurtovenko, A. A.; Anwar, J.; Vattulainen, I. *Chemical Reviews* **2010**, *110*, 6077.
(4) Psachoulia, E.; Marshall, D. P.; Sansom, M. S. P. *Accounts of Chemical Research* **2010**, *43*, 388.
(5) Lyubartsev, A. P.; Rabinovich, A. L. *Soft Matter* **2011**, *7*, 25.
(6) Bandyopadhyay, S.; Tarek, M.; Klein, M. L. *Journal of Physical Chemistry B* **1999**, *103*, 10075.
(7) Faller, R.; Marrink, S.-J. *Langmuir* **2004**, *20*, 7686.
(8) Pal, S.; Milano, G.; Roccatano, D. *Journal of Physical Chemistry B* **2006**, *110*, 26170.
(9) Bennett, W. F. D.; MacCallum, J. L.; Hinner, M. J.; Marrink, S. J.; Tieleman, D. P. *Journal of the American Chemical Society* **2009**, *131*, 12714.
(10) Brannigan, G.; Lin, L. C. L.; Brown, F. L. H. *European Biophysics Journal with Biophysics Letters* **2006**, *35*, 104.
(11) Muller-Plathe, F. *Chemphyschem* **2002**, *3*, 754.
(12) Peter, C.; Kremer, K. *Soft Matter* **2009**, *5*, 4357.
(13) Sintes, T.; Baumgartner, A. *Biophysical journal* **1997**, *73*, 2251.
(14) Sintes, T.; Baumgaertner, A. *Journal of Physical Chemistry B* **1998**, *102*, 7050.
(15) Lenz, O.; Schmid, F. *Journal of Molecular Liquids* **2005**, *117*, 147.
(16) Goetz, R.; Lipowsky, R. *Journal of Chemical Physics* **1998**, *108*, 7397.
(17) Marrink, S. J.; de Vries, A. H.; Mark, A. E. *Journal of Physical Chemistry B* **2003**, *108*, 750.
(18) Marrink, S. J.; Mark, A. E. *Journal of the American Chemical Society* **2003**, *125*, 15233.
(19) Marrink, S.-J.; Mark, A. E. *Biophysical Journal* **2004**, *87*, 3894.
(20) Kawakatsu , T. *Statistical Physics of Polymers. Springer: Berlin, 2004*
(21) Marcelja, S. *Nature* **1973**, *241*, 451.
(22) Leermakers, F. A. M.; Scheutjens, J. *Journal of Chemical Physics* **1988**, *89*, 3264.
(23) Mueller, M.; Katasov, K.; Schick, M. *Physics Reports* **2006**, *434*,

113.
(24) Leermakers, F.; Rabinovich, A.; Balabaev, N. *Physical Review E* **2003**, *67*, 011910.
(25) Muller, M.; Schick, M. *Physical Review E* **1998**, *57*, 6973.
(26) Szleifer, I.; Carignano, M. A. In *Advances in Chemical Physics*; John Wiley & Sons, Inc.: 2007, p 165.
(27) Muller, M.; Smith, G. D. *Journal of Polymer Science Part B: Polymer Physics* **2005**, *43*, 934.
(28) Daoulas, K. C.; Muller, M.; Stoykovich, M. P.; Park, S. M.; Papakonstantopoulos, Y. J.; de Pablo, J. J.; Nealey, P. F.; Solak, H. H. *Physical Review Letters* **2006**, *96*.
(29) Detcheverry, F. A.; Kang, H. M.; Daoulas, K. C.; Muller, M.; Nealey, P. F.; de Pablo, J. J. *Macromolecules* **2008**, *41*, 4989.
(30) Kucerka, N.; Tristram-Nagle, S.; Nagle, J. F. *Biophysical Journal* **2006**, *90*, L83.
(31) Katsaras, J.; Tristram-Nagle, S.; Liu, Y.; Headrick, R. L.; Fontes, E.; Mason, P. C.; Nagle, J. F. *Biophysical Journal* **2000**, *78*, 116Plat.
(32) Kucerka, N.; Nagle, J. F.; Sachs, J. N.; Feller, S. E.; Pencer, J.; Jackson, A.; Katsaras, J. *Biophysical Journal* **2008**, *95*, 2356.
(33) Kucerka, N.; Liu, Y.; Chu, N.; Petrache, H. I.; Tristram-Nagle, S.; Nagle, J. F. *Biophysical Journal* **2005**, *88*, 2626.
(34) Marrink, S.-J.; Risselada, H. J.; Yefimov, S.; Tieleman, D. P.; de Vries, A. H. *J Phys Chem B* **2007**, *111*, 7812.
(35) Nagle, J. F.; Zhang, R.; Tristram-Nagle, S.; Sun, W.; Petrache, H. I.; Suter, R. M. *Biophysical Journal* **1996**, *70*, 1419.
(36) Zhao, Y.; De Nicola, A.; Kawakatsu, T.; Milano, G. *Journal of Computational Chemistry* **2012**, *33*, 868.
(37) Nagle, J. F.; Tristram-Nagle, S. *Biochimica et Biophysica Acta (BBA)-Reviews on Biomembranes* **2000**, *1469*, 159.
(38) Balgavı, P.; Dubniková, M.; Kuerka, N.; Kiselev, M.; Yaradaikin, S.; Uhríková, D. *Biochimica et Biophysica Acta, Biomembranes* **2001**, *1512*, 40.
(39) Van der Spoel, D.; Lindahl, E.; Hess, B.; Groenhof, G.; Mark, A. E.; Berendsen, H. J. C. *Journal of Computational Chemistry* **2005**, *26*, 1701.

5
Particle-Field Models of Block-Copolymer

5-1 Particle-Field model of Pluronic® Block-Copolymers to study phase morphologies

The triblock-copolymers of poly(ethylene oxide)$_m$-poly(propylene oxide)$_n$-poly(ethylene oxide)$_m$ (PEO_m-PPO_n-PEO_m), are an important family of amphiphilic polymers. They are commercially known and available as Pluronic® or Poloxamer. The hydrophilic-lipophilic character of these block-copolymers can be tuned varying the blocks length and the molecular weight of both, PEO and PPO blocks. Such adaptability allowed to employ these copolymers in many fields, like foaming, detergency, dispersion stabilization, emulsification[1], lubrication, cosmetic formulation, modification of surface for biocompatibility for medical applications[2]. The Pluronic micelles used for the drug delivery are one of the most studied for medical applications[2]. Such

micelles have the capability to include hydrophobic drugs inside the PPO core[3] and transport them in the body. Recently, the Pluronic micelles have been also used in the cancer therapy[4]. For these reasons the micellar phase has been investigated in deep by numerous experimental techniques. For example, critical micelle concentration (CMC) and critical micelle temperature (CMT) have been studied with dynamic light scattering and fluorescence spectroscopy[5]. Extensive experimental studies of Pluronic phase behavior in water has been reported by Alexandridis[6-9] and Zhou[10,11].

A study of the kinetic process of micellization of Pluronic L64 in water, measured with dynamic light scattering technique, shows that the self-assembly process is a complex multistep phenomenon that occurs on a time scale of the order of μs[12]. Atomistic simulations, due to the large length and timescale involved, cannot be directly applied to study these self-assembly phenomena. Just to have an idea about the size, if we consider a simulation of 300 Pluronic L62 chains hydrated by 56,000 water molecules, i.e. the smallest system reported in the present investigation, it would involve about 200,000 particles. Atomistic simulations, due to their computational costs, usually are confined to systems on time and length scales of ns and few nm.

On the other hand, different computational approaches based

on mean field density functional theory have been proposed for these systems[13,14]. Fraaije[15] proposed a model to study the morphologies of non dilute water/Pluronic solution. In the framework of self-consistent field (SCF) theory, the model systems are not represented by particles but by density fields, and the mutual interactions between the segments are decoupled and replaced by interaction between the segments and static external fields. Such approaches are computationally less expensive and reach time and length scales able to reproduce the morphologies of different phases. Their disadvantage is that in such models the chemical specificity and the link with atomic structure are difficult to achieve.

A different approach, based on reference atomistic data, using a coarse-grained (CG) implicit solvent model has been reported by Bedrov[16], while a similar CG model for symmetric triblock-copolymers, but having explicit water beads, has been reported by Faller[17]. Such CG models are computationally less expensive compared with atomistic models but are still expensive compared with SCF approaches and are of quite limited use for the investigation of phase patterns formation.

We present a computational study of the phase behavior of binary Pluronic-water mixtures, based on the hybrid particle-

field (PF) molecular dynamics method[18,19]. The idea behind the hybrid PF molecular dynamics approach is to obtain a strategy, as far as will be possible, having a similar accessibility to large time and length scales of pure SCF methods, and including at the same time the chemical specificity of atomistic and CG models. As shown in Chapter 3, PF models of phospholipids have been reported to study the phase behaviour of phospholipid/water mixtures. In particular, we investigate the phase behaviour, as function of the composition and temperature, for the Pluronics PEO_6-PPO_{34}-PEO_6 (L62) and PEO_{13}-PPO_{30}-PEO_{13} (L64).

At low polymer concentration, in a water solution, Pluronic chains self-assembly in micellar phases. The micelles are formed by a hydrophobic core, mainly composed by PPO blocks, and by a hydrophilic corona, formed by hydrated PEO blocks. At higher polymer wt% content the Pluronic chains self-assembly in different phases, passing through the lamellar phase to isotropic solutions at high polymer contents[6].

In the next subsections we want to present and validate the PF coarse-grained model for micellar and non-micellar phases. In particular, the transferability of the model to systems at different polymer content has been investigated.

5-1.2 Model and Parameters

The CG model used in this study is parameterized on the basis of the results of atomistic models reported by some of us in a previous paper[20]. Moreover we tested the reproduction of structural properties of a single micelle of Pluronic L64 compared with experimental data.

The model of Pluronics employed in this study can be considered an extension of the GC model reported in reference[21], from which the bonds and angle distributions have been used to parametrize the intramolecular interactions. Differently from the models already reported, in the framework of PF models, here the intermolecular interactions have been evaluated using a field theoretic approach[18,19] (see the Chapter 2).

The mapping scheme adopted for the CG model in the present work is depicted in Figure 5-1. Each bead of the CG model for EO and PO corresponds to three (C-O-C) and four (C(CH3)-O-C) heavy atoms, respectively. Oxygen atoms (depicted in red in Figure 5-1) were considered as centers of each bead for both EO and PO repeating units.

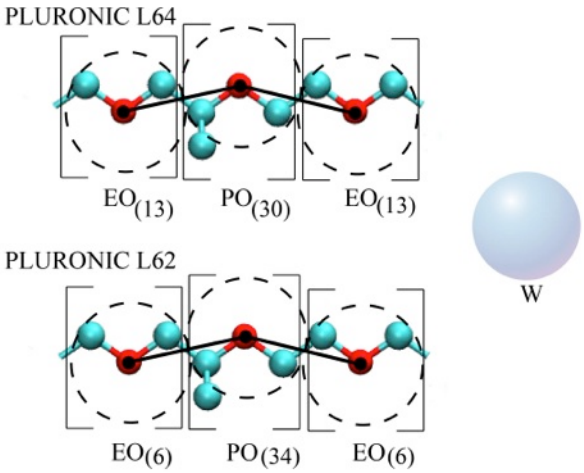

Figure 5-1. The mapping scheme used for the model of Pluronic. Each EO bead corresponds to three heavy atoms. For PO, each bead corresponds to four heavy atoms. The effective beads are centered on oxygen atoms (depicted in red) for both EO and PO types. The bead type W corresponds to four real water molecules.

According to this, the bond length between two beads corresponds to distance between two oxygen atoms of two consecutive repeating units. The angle formed between two adjacent vectors corresponds to angle formed between three consecutive oxygen atoms of three consecutive monomers. The target distributions of bond and angle are calculated from atomistic simulations[20].

The force field parameters of the CG model, for intramolecular part, were taken from the references[20-22]. Such CG force field has been based on the reproduction of both, bond and angle distributions, of atomistic simulations[23,24], in which small oligomers of PEO and PPO have been simulated

in water and different solvents. Force-field parameters for intramolecular interactions are summarized in Tables 5-1 and 5-2. In particular, the bond is described by a harmonic potential of the form:

$$V_{bond}(r) = \frac{1}{2} K_{bond}(r - r_{bond})^2 \qquad (1)$$

where r_{bond} is the equilibrium bond length and K_{bond} is the force constant. The stiffness of the chains is also taken into account by a harmonic bending potential $V_{\text{angle}}(\theta)$ that depends on the cosine of the angle θ between two successive bonds.

$$V_{angle}(\theta) = \frac{1}{2} K_{angle} \left\{ \cos(\theta) - \cos(\theta_0) \right\}^2 \qquad (2)$$

where K_{angle} is the force constant and θ_0 is the equilibrium bond angle. Angle parameters adopted for the models of this paper are reported in Table 5-2.

The particle-field parameters $\chi_{KK'}$ required to calculate the interactions between a particle of type K and the density field due to the particles type K' are listed in Table 5-3.

The particle-field interaction parameters between PEO/water and PPO/water have been tuned to reproduce the radius of

gyration of aqueous solution of PEO and PPO polymer, at different molecular weights[21].

Table 5-1. Parameters for bond potential.

Bond Type	$\mathbf{r_{bond}}$ (nm)	$\mathbf{K_{bond}}$ (kJ mol^{-1} nm^{-2})
PEO-PEO	0.28	8000.00
PPO-PPO	0.28	5000.00
PEO-PPO	0.28	6500.00

Table 5-2. Parameters for angle potential.

Angle Type	$\boldsymbol{\theta}$ (deg)	$\mathbf{K}\boldsymbol{\theta}$ (kJ mol^{-1})
PEO-PEO-PEO	155.00	40.00
PEO-PPO-PPO	140.00	40.00
PEO-PEO-PPO	140.00	30.00
PPO-PPO-PPO	140.00	30.00

Table 5-3. Particle-field interaction matrix. $\chi_{KK'}RT$ (kJ mol^{-1})

χ	**Water**	**PEO**	**PPO**
Water	0.00	1.50	4.60
PEO	1.50	0.00	16.00
PPO	4.60	16.00	0.00

5-1.3 Computational Details

The parallel program OCCAM was used for molecular dynamics simulations. All simulations have been performed using a time steep of 0.03 ps, with *NVT* ensemble by keeping the temperature constant using Andersen thermostat with a collision frequency of 7 ps^{-1}. Details about the composition of the systems are summarized in Table 5-4.

Table 5-4. System Compositions

Systems	**Composition** (no. of molecules)				**Polymer wt%**	**Temp.**	**Box size**	**Simulated time**
	L62	L64	Water	Particle no.		(K)	(nm)	(μs)
I	304	0	56016	70000	20	303	20x20x20	2.7
II	791	0	33614	70000	52	303	20x20x20	3.3
III	1065	0	21010	70000	70	303	20x20x20	3.5
IV	1370	0	6980	70000	90	303	20x20x20	3.5
V	0	250	56000	70000	20	303	20x20x20	3.5
VI	0	650	33600	70000	52	303	20x20x20	3.7
VII	0	875	21000	70000	70	303	20x20x20	4.3
VIII	0	1125	7000	70000	90	303	20x20x20	3.3
IX	0	1	8500	8556	24	303[a]	10x10x10	0.3
X	0	3696	23000	230000	90	303	30x30x30	6.0

[a]The system IX has been simulated also at the temperature of: 288, 293, 298 K.

5-1.4 Morphology of different phases

In principle, the parameters of a coarse-grained model are not easily transferable. In particular, $\chi_{KK'}$ parameters required to calculate the interactions between a particle of type *K* and the density field due to the particles type *K'* can depend on composition and temperature. This dependency cannot be known a priori and need to be investigated for every coarse-grained model.

The main purpose of this study is to study and validate the PF model for both micellar and non micellar phases corresponding to low and high block-copolymer contents, respectively. In particular, two different block-copolymers, Pluronic L62 and Pluronic L64, have been chosen. Although the molecular weights of Pluronic L62 and L64 are comparable (~2900) the ratio PEO/PPO is quite different, and consequently the Hydrophobic Lipophilic Balance (HLB), that summarizes the structural differences, assumes values of 7 for L62 and 15 for L64. The HBL is defined as the ratio of lengths of the EO on PO blocks. It can be expressed by the following empirical form:

$$HBL = -36.0\frac{N_{PPO}}{N_{PEO}+N_{PPO}} + 33.2 \qquad (3)$$

We investigate a binary block-copolymer/water system of

both, Pluronic L62 and L64, to observe the spontaneous formation of different morphologies as function of concentration and temperature. To this aim, four different polymer concentrations have been considered (20, 52, 70, 90 wt% of polymer content).

Micellar and Hexagonal Phases: The time behaviour of SCF potentials of systems at different concentrations is reported in Figure 5-2.

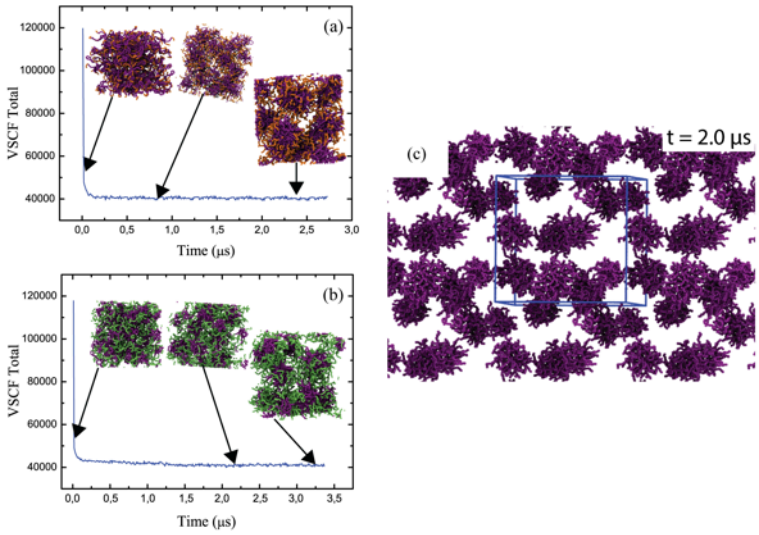

Figure 5-2. Time behavior of SCF potential for the composition of 20 wt% polymer content. (a) System I of Pluronic L62 (b) System V of Pluronic L64 (c) Representative snapshot of micellar phase in which the system has been extended in the xy plane. Only hydrophobic PPO blocks are depicted. The different colors, orange and green, assigned to the PEO beads of Pluronic L64 and L62 has been done to easily distinguish the L62 and L64 in the snapshots of simulations. No difference in the mapping scheme or interaction parameters exists. The water beads W are omitted for clarity.

Representative snapshots of systems are included above the plots. The compositions of the simulated systems are reported in Table 5-4. At low concentration of Pluronic (20 wt%), in agreement with experimental phase behavior[9], a micellar morphology has been found. At that concentration the block-copolymer molecules self-assemble into spherical micelles for both L62 and L64 (Figure 5-2a and 2b). The micellar phase reproduction is not surprising because the model used in this work was parameterized at similar concentration and tuned to reproduce the experimental radii, of core and corona, of a L64 micelle. In Figure 5-2c a representative snapshot of micellar phase has been reported. To favor the visualization, the system has been extended in the one plane.

The time behaviors of both, number of clusters and number of chains/cluster (i.e. aggregation number, N_{agg}), are reported in Figure 5-3. From the plots is clear that starting from 2 μs for both L62 and L64 the number of clusters and the aggregation number are fluctuating around a constant value. The time needed for the formation of stable micellar structures is of the same order of magnitude of the one reported from experiments[25].

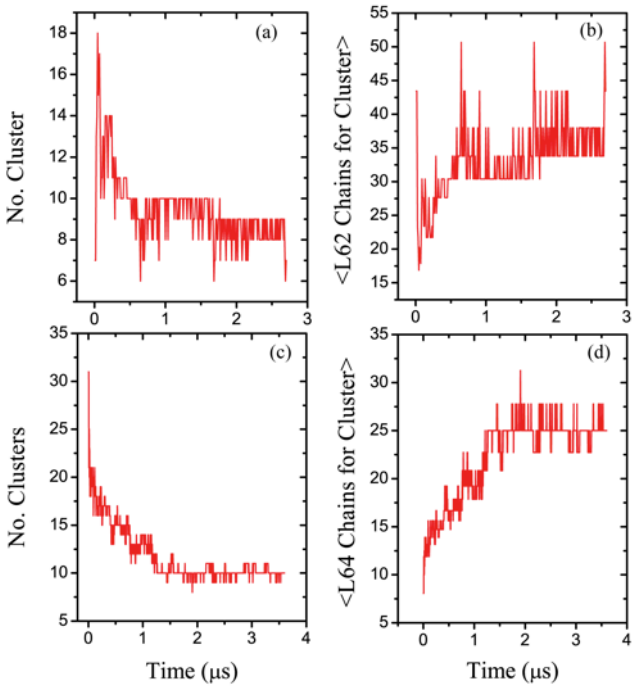

Figure 5-3. Time behavior of: (a) Number of Pluronic L62 clusters for the system I. (b) Number of Pluronic L62 chains per cluster for the system I. (c) Number of Pluronic L64 clusters for the system V. (d) Number of Pluronic L64 chains per cluster for the system V. The number of cluster is calculated on the basis of a cut off value (1 nm) on the shortest distance between PPO units of two different L64 chains.

The temperature dependence of the cluster size has been also investigated. The calculated N_{agg} 24 at 303 K is comparable with the experimental value of 19 found at the same temperature[8,26] . As reported by Alexandridis[6,8,9,25] for a diluite solution of Pluronic L64 (2.5 wt%) the $N_{agg.}$ increases from 37 to 54 in the temperature range 37-55 °C. In non diluite water/L64 solution (31.9 wt%) an increase of $N_{agg.}$ from 1 up to 69 in the temperature range 8-35°C has been reported by

Wu[26]. A similar behavior of temperature dependency of $N_{agg.}$ has been found for different Pluronics, P85, F88, F68, F127.

As pointed out by Alexandridis *et al*. the hydrophobic block of the Pluronics (PO) is responsible for the micellization due to diminishing hydrogen bonding between water and (PO) with increasing temperature. Correspondingly the PEO-water and PPO-water χ interaction parameters increase with tempereature[27] and the PEO-PPO interaction parameter decreases[28].

We found a different behavior for our model, in fact, as shown in the Figure 5-4a, the average number of Pluronic L64/cluster decreases by increasing the temperature. The same behavior has been found for the Pluronic L62. The origin of this disagreement between experiments and simulations can be ascribed to the use of fixed $\chi_{KK'}$ parameters at different temperatures. A better agreement could be obtained using a more flexible model allowing the correct temperature dependency of $\chi_{PEO,W}$ and $\chi_{PPO,W}$ (of the type $\chi = \chi_0\left(A_1 - \frac{B_1}{T}\right)$) and for the $\chi_{PEO,PPO}$ (of the type $\chi = \chi_0\left(A_2 - \frac{B_2}{T}\right)$), where A_i and B_i can be tuned to reproduce the correct experimental behavior.

In addition the R_g of a single L64 chain in water has been calculated at different temperatures, and the results have been

compared with experimental value[29]. In Figure 5-4b the temperature behavior of R_g is reported. The red cross represents the experimental value of R_g measured by light scattering for a water solution of Pluronic L64 with a concentration below the CMC. We found for our model at 283K a R_g of 2.3 nm, larger than the experimental one (1.8 nm)[29]. Also in this case, temperature dependent χ parameters would lead to a better agreement.

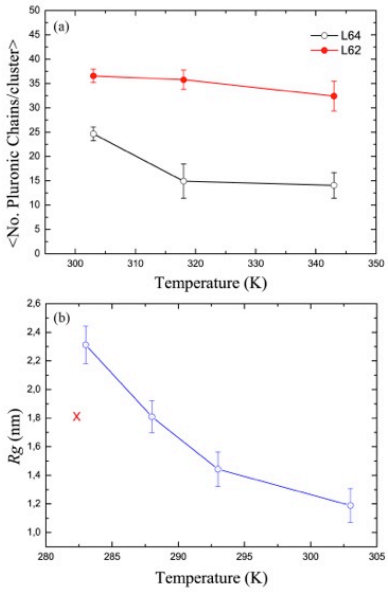

Figure 5-4. (a) Average number of Pluronic chains per cluster depending on the temperature for both, L62 and L64. (b) Radius of gyration of a L64 single chain in water calculated at different temperatures (system IX). The red cross represents the experimental value.

The experimental phase diagram[9] of both, Pluronic L62 and Pluronic L64, shows that the morphologies corresponding to

phases in the range of 50~80 wt% are different for L62 and L64. In particular, for the Pluronic L62 the lamellar morphology is stable in a range of 60~70 wt%. Differently, the Pluronic L64 having similar PPO block to that of L62 but longer PEO blocks, shows the presence of an additional hexagonal phase that is rather narrow and extends from 46~52 wt% L64 content. Although the wt% content of the system II for the Pluronic L62 is not representative of a hexagonal phase, we studied that composition for both, L62 and L64, to test the specificity of our model in the reproduction of this peculiar phase behavior.

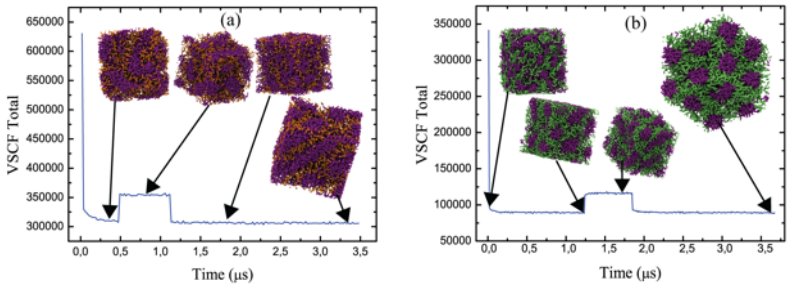

Figure 5-5. Time behavior of SCF potential for the composition of 52 wt% polymer content. (a) System II of Pluronic L62 (b) System VI of Pluronic L64

In Figure 5-5a and 5b the time behaviors of SCF potential are reported. In order to speed up the self-assembly process, an annealing procedure has been applied for both Pluronics. The systems have been heated up to 830 K and cooled down to

303 K in about 0.6μs for both. Then the temperature of the systems has been kept constant, by Andersen thermostat, at 303 K. The temperature time behaviors, together to significant snapshots of the systems, are reported in Figure 5-6a and 6b.

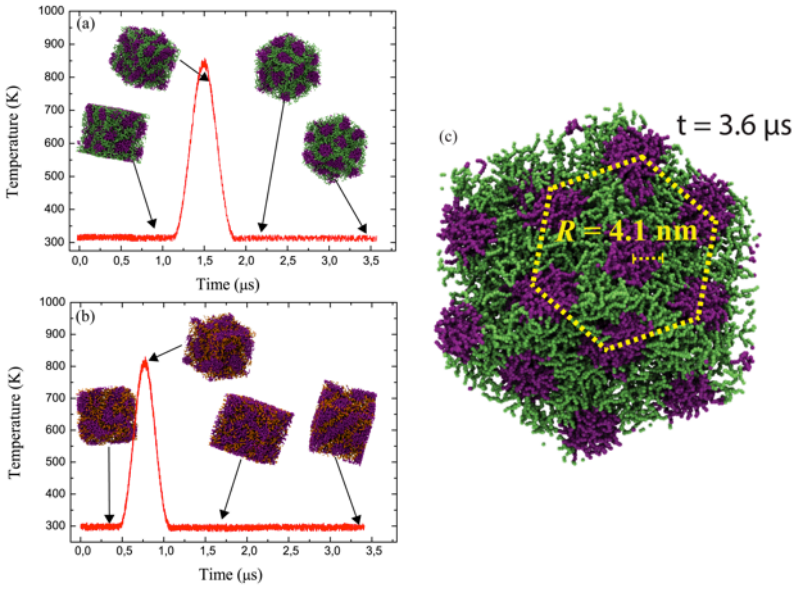

Figure 5-6. Temperature time behavior: (a) System VI Pluronic L64 forming a hexagonal morphology. (b) System II Pluronic L62 forming a lamellar morphology. (c) Detail of hexagonal morphology obtained for the Pluronic L64. The experimental value[45] of apolar cylinder radius *R* is reported on the picture.

For the Pluronic L62, according to experimental phase behavior, the hexagonal morphology is not obtained. Differently, for the Pluronic L64 a hexagonal morphology, according to experimental phase diagram[9], is reached after 2.1 μs. In that phase the Pluronic chains self-assemble in cylindrical structures with a well defined periodicity. A

structural parameter of the hexagonal morphology, depending on the periodicity, is the apolar cylinder radius (R) of the PPO block. In Figure 5-6c is clear that simulated structure well agrees with the experimental value of R = 4.1 nm reported by Alexandridis[9].

Lamellar phase and High Polymer content isotropic solution: According to the phase diagram, the composition of 70 wt% of polymer has been chosen, for both Pluronics. In Figures 5-7a and 7b time behavior of SCF potential is reported. During the simulations, the SCF potential quickly reaches the equilibrium and a well structured lamellar morphology, according to experimental behavior,[8] has been found for both Pluronic L62 and L64. We extended the investigation of phase behavior reproduction of our model also in the phase with polymer content higher than 70 wt%. To this aim the composition of 90 wt% of polymer has been chosen. In the Figure 5-7c and 7d the time behaviors of SCF potential are reported for both Pluronics. For the L62 we obtain, at equilibrium, a lamellar morphology instead of complex interconnected structures as postulated from the experiments. Similarly, for the Pluronic L64 we obtained a morphology close to the lamellar one, but with defects. Probably, these results are affected by finite size effects, due

to periodic boundary conditions (PBC) favoring the lamellar morphologies.

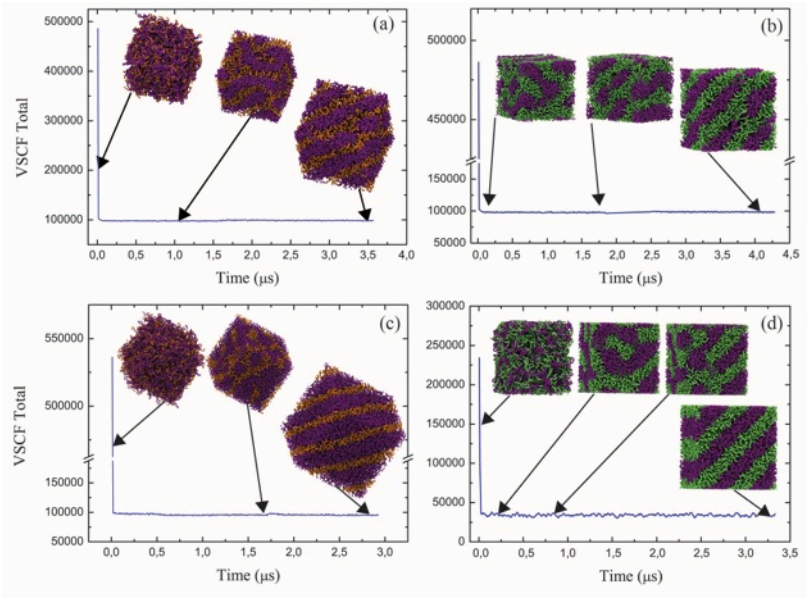

Figure 5-7. Time behavior of SCF potential for the compositions of 70 and 90 wt% polymer content. (a) Sistem III of Pluronic L62 (b) System IV of Pluronic L64 (c) System VII of Pluronic L62 (d) System VIII of Pluronic L64.

The behavior of the radius of gyration (R_g) as function polymer composition has been also investigated. In particular, we report in Figure 5-8 the R_g of the entire chain of Pluronic and the partial R_g calculated for PEO and PPO segments separately. As expected, the high water content of the systems I and V plays a strong role in the PPO segregation, resulting in the smallest R_g found for all composition studied. Instead, at higher block-copolymer content we observe an increasing

of total R_g and PPO. Not a significant variation of R_g of the PEO blocks has been observed (Figure 5-8c).

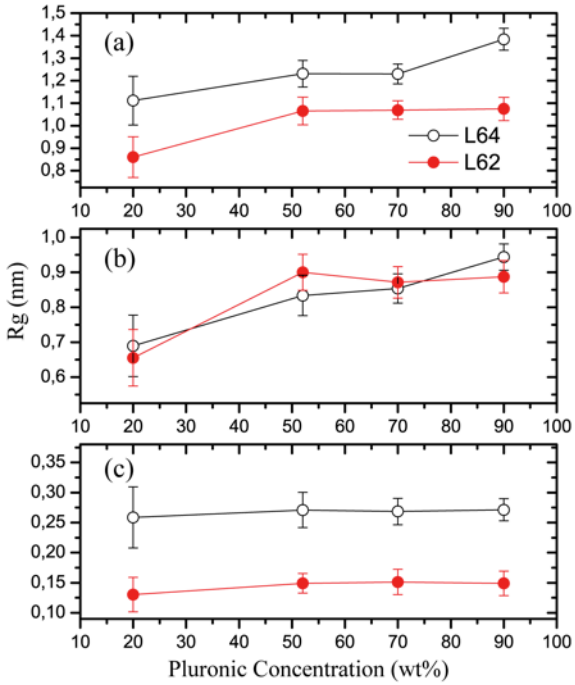

Figure 5-8. Average radius of gyration, depending on the wt% polymer content, of: (a) total chain of Pluronic. (b) PPO block. (c) PEO blocks. The empty black circle represents the Pluronic L64. The red whole circle is used to the Pluronic L62.

All the morphologies obtained at different contents of polymer and different temperatures for both Pluronic L62 and L64, together with the experimental phase diagram are depicted in Figure 5-9.

For the Pluronic L62 the morphologies found at 303 K are in agreement with the experimental phase diagram[9]. In fact, at

low polymer content we found spherical micellar morphology, as expected. A lamellar morphology has been observed at 52, 70 and 90 Pluronic L62 wt% content, as expected. Differently from the phase diagram, for the 90 wt% we still found the lamellar morphology instead of complex interconnected structures.

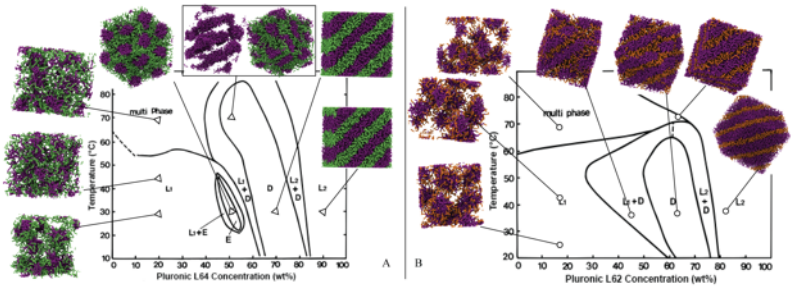

Figure 5-9. Phase diagrams for Pluronic L62 in (A) and Pluronic L64 in (B). For any composition and temperature studied, a snapshot of the obtained morphology has been depicted on the diagram. The phase diagrams are redrawn from the ref.[8].

For the Pluronic L64 a similar figure has been shown. At 303 K we found micellar, hexagonal and lamellar morphologies according to phase diagram[9]. At temperature higher than 303 K we found a stable micellar morphology for 20 wt% of L64. Instead, at 52 wt% the hexagonal morphology is not stable, according to phase diagram, and a lamellar morphology with defects has been observed.

At 90 wt% of L64 content, as observed for L62, we found a lamellar morphologies instead of the more complex structures postulated from experiments. Probably, as discussed above,

simulation results are affected by finite size effects, due to PBC favoring the lamellar morphologies. In order to reduce such effect we simulated a system in which the box lengths are increased by a factor 1.5 (system X in Table 5-4). In Figure 5-10 snapshots at different times for the system X are depicted. The water beads and PEO blocks are excluded from the snapshots. Complex and interconnected structures at 1.5 and 3.0 μs start to be formed.

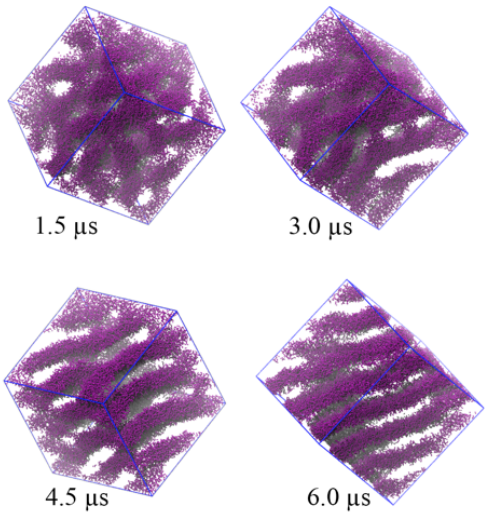

Figure 5-10. Snapshots of the system X (see Table 5-4) taken at different time. The box lengths is 1.5 times (30x30x30 nm) larger than those ones used for systems studied in the present work.

The system evolves, in 6 μs, in a morphology having interconnected lamellae formed by PPO blocks. These complex structures, probably, are characterized by

lengthscales of the same order of the box size and further investigation with systems larger than those ones studied in the present work should be considered.

One of the important uses of CG models is to obtain well-relaxed structures useful for generating configurations at a higher level of chemical detail. An example is the generation by local relaxation of structure of dense polymer melts at the atomistic level starting from mesoscale models[30,31].

The Pluronic CG model presented in this work has been based on the atomistic models. The mapping scheme proposed for that model is strictly connected to atomistic scale. In fact, every EO and PO bead includes 3 and 4 heavy atoms, respectively. Differently from Pure SCF or DPD approaches, our model is still very close to an atomistic one. Such feature allows reintroducing, by reverse-mapping procedures, the atomistic details. More detail about the reverse-mapping procedure can be found in the Appendix A.

Moreover, as shown previously, we are able to obtain morphology patterns typically of the mesoscale length. Combining the possibility of our model to reintroduce atomistic detail with morphologies obtained from the CG model on the scales of μs and nm, we report an example of reverse mapping for the hexagonal morphology. The full atomistic configuration obtained is formed by ~600.000

particles. In Figure 5-11a both structures, atomistic and coarse-grained, are depicted. From the atomistic structure the scattering factors (q) are calculated and compared with SAXS spectrum[9] as shown in Figure 5-11b.

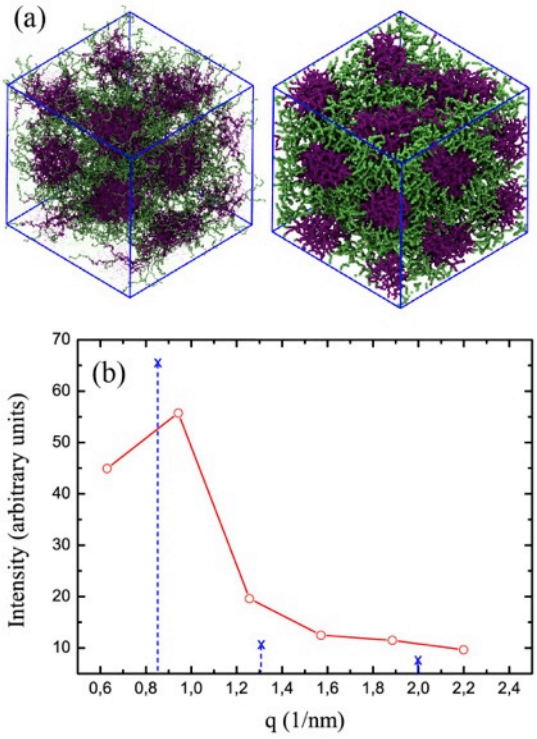

Figure 5-11. (a) Atomistic structure, obtained after backmapping procedure, and CG structure of the hexagonal morphology for the Pluronic L64. Each EO and PO beads correspond to 3 and 4 heavy atoms, respectively. (b) Calculated scattering factor q for the atomistic structure of hexagonal morphology obtained for the Pluronic L64. The blue points represent the experimental values of SAXS spectra[9].

5-2 Interaction Between Pluronic Micelle and Biomembranes

In medicine the use of nanosized tools for the diagnosis, prevention and treatment of diseases is becoming more and more popular[32]. First generation nanomedicines, nowadays, are in routine clinical use and include both "blockbuster" drugs and certain specific products[33]. In this context the use of polymeric materials is very broad[34] and polymer based formulations are among the most successful nanomedicines[34-38].

Among several diseases, cancer is a major target of the development of new drugs with many clinical trials ongoing and involving nanomedicines[39]. Technologies include liposomes[40-42], polymer conjugates[34-36] and block copolymer micelles[2,37,38,43]. Tumor angiogenesis creates the gateway for tumor access of nanosized objects. Matsumura and Maeda described the enhanced permeability and retention effect (EPR) in the 1980s[44], the "gaps" created by angiogenesis can be much larger (100 nm to 2 μm) than those reported in normal tissues. For this main reason, nanosized drugs tend to accumulate in tumor tissue much more than they do in normal tissues. Due to EPR effect, for these drug vectors, it is clear

that the smaller is considered to be the better and constructs in the size range of 5-30 nm are considered optimal, and thus the control of the size of systems for drug delivery is very important.

Block copolymer micelles including drugs by physical entrapment are undergoing phase I/II studies as anticancer agents[32]. Pluronics as micellar aggregates have been employed to store several drugs[45-48]. Pluronics are amphiphilic linear triblock copolymers having the central block of hydrophobic polypropylene oxide (PPO) covalently bond with two blocks of hydrophilic polyethylene oxide (PEO). An example of successful Pluronics application is the doxorubicin formulation SP1049C developed using a combination of two Pluronics, L61 and F127[49].

Despite the large interest in Pluronics block copolymers in cancer therapy, only recently they became the subject of molecular simulation studies involving biomembranes[21,23,24,50-52]. The understanding of the interaction mechanisms of these synthetic polymers with biomolecules needs a description at atomic level of both structure and dynamics of the systems. Atomistic models can provide very accurate descriptions by using suitable force fields are potentially able to give consistent information. Atomistic models suitable for Pluronics have been proposed and validated in water and

several solvents[20,22,53] and in several organic solvents[20,22]. These models have been used to study the percolation and distribution of PEO chains using steered molecular dynamics, PEO and PPO oligomers[23,50] and Pluronics inside model biomembranes[51,52]. So far, none of these simulation studies have been addressed to understand the interaction of Pluronics self-assembled structures like micelles with models of cell membranes. These studies are difficult because they involve the simulation of systems on length and time scales not accessible by the current atomistic simulation methods. To this aim specific coarse-grained models that are able to keep molecular specificity can be used in order to reach time and length scales relevant for this systems. The dynamics of these processes at molecular level is so far not easily accessible also to experimental measurements and therefore many questions are still undisclosed on the molecular details of the interaction mechanisms.

We report the development and validation of coarse-grained models of Pluronics that are able to describe micellar assemblies and their interactions with phospholipids. These models have been employed for large scale simulations of Pluronic L64 micelles interacting with dipalmitoylphosphatidylcholine (DPPC) lipid bilayers. Due to the relevance of these block-copolymers assembled

nanostructures for drug delivery applications, the role of embedded drug molecules has been also considered. In particular, we focused on the interplay between the interactions of drug molecules with the hydrophobic core of the micelle and their mutual influence on the micelle and lipid bilayer structures.

5-2.1 Models and Parameters

Hybrid models, due to their computational efficiency are gaining popularity also for biomembranes modeling. In particular, solvent-free, a coarse-grained model for lipid bilayer membranes where nonbonded interactions were treated by a weighted-density functional has been introduced by Hömberg and Müller.[54] Very recently, Sevink et al.[55] introduced a hybrid scheme, combining Brownian dynamics (BD) and dynamic density functional theory (DDFT), that is able to model efficiently complete vesicles with molecular detail. The coarse-grained model adopted in this study for lipids has been extensively described and validated in two previous papers[56,57]. For the models used in this work for Pluronics, intramolecular bonded interactions, bond and angle potentials have been taken from the ones reported in reference[21], while non-bonded interactions are described using

a field theoretic approach.

The parametrization of the hybrid particle-field models of Pluronics has been done considering different reference systems. Models of PEO and PPO chains have been developed considering effective particles each of them grouping the atoms of one repeating unit. The mapping scheme adopted in this work is depicted in Figure 5-12. The scheme can be considered a 4:1 mapping, i.e. four atoms are grouped in one bead. Bonds and angles are described by a harmonic potentials, respectively Eq. (1) and Eq. (2). Parameters adopted for all bond and angle types are reported in Table 5-5 and Table 5-6.

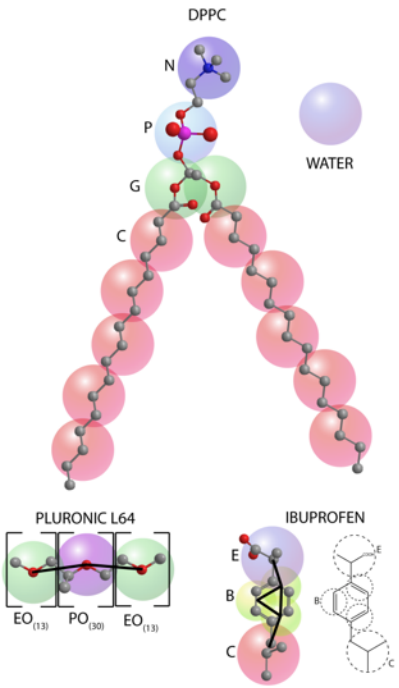

Figure 5-12 Mapping scheme adopted for the models of DPPC, Pluronic L64, Water and Ibuprofen. Basically the mapping scheme can be considered as 4:1.

In order to calculate the MD-SCF potential, several mean field parameters $\chi_{KK'}$ between a particle of type *K* with the density field due to particles of type *K'* are needed.

In Table 4–7 the set of $\chi_{KK'}$ parameters used in this study are reported. Lipid bilayers models have been full validated in references 56 and 57. Mean field $\chi_{KK'}$ parameters for the interaction of ethylene oxide (EO) and propylene oxide (PO) repeating units with water and lipid bilayers have been tuned to reproduce several reference data from atomistic

simulations[23]. More details about the parameterization will be given in following.

Table 5-5. Force field bond parameters according to the Eq. (1)

Bond type	r_{bond} (nm)	K_{bond} (kJ mol^{-1}nm^{-2})
N-P	0.470	1250.0
P-G	0.470	1250.0
G-G	0.370	1250.0
G-C	0.470	1250.0
C-C[a]	0.470	1250.0
EO-EO	0.280	8000.0
PO-PO	0.280	5000.0
EO-PO	0.280	6500.0
E-B	0.310	7500.0
B-B	0.270	8000.0
B-C	0.310	7500.0

[a] These parameters have been used also for trimer model.

Table 5-6. Force field angle parameters according to Eq. (2)

Angle type	θ (deg)	K_θ (kJ mol^{-1})
P-G-G	120.0	25.0
P-G-C	180.0	25.0
G-C-C	180.0	25.0
C-C-C	180.0	25.0
EO-EO-EO	155.0	40.0
EO-PO-PO	140.0	40.0
EO-EO-PO[a]	140.0	30.0
PO-PO-PO	140.0	40.0
E-B-B	150.0	50.0
B-B-B	120.0	50.0
B-B-C	150.0	50.0

[a] These parameters have been used also for trimer model

Table 5-7. Particle-field interaction matrix. $\chi_{AB} \times$ RT(kJ mol^{-1}) for Systems I-III.

	N	P	G	C	Water	EO	PO
N	0.00	-1.50	6.30	9.0	-8.10	-5.25	2.60
P	-1.50	0.00	4.50	13.50	-3.60	-0.75	7.55
G	6.30	4.50	0.00	6.30	4.50	5.00	0.00
C[a]	9.00	13.50	6.30	0.00	33.75	7.80	-1.60
Water	-8.10	-3.60	4.50	33.75	0.00	1.50	4.60
EO[b]	-5.25	-0.75	5.00	7.89	1.50	0.00	16.00
PO	2.60	7.55	0.00	-1.60	4.60	16.00	0.00

a) same parameters have been used for the particle of type B of IBU molecules. b) same parameters for particle of type E of IBU molecules

5-2.2 L64 Single Chains and Micelle in Water

Mean field interaction parameters ($\chi_{KK'}$, Table 5-7) between EO and PO beads and water have been tuned to reproduce the behavior of the gyration radius with respect to the chain length obtained from atomistic simulations. An initial set of parameters for the interaction of EO and PO with water ($\chi_{PEO,W} \times RT = 2.1$ and $\chi_{PPO,W} \times RT = 3.4$ kJ/mol) has been taken starting from a_{ij} parameters used in Dissipative Particle Dynamics (DPD) models reported by Cao et al.[58] and using the linear relation introduced by Groot and Warren[59] connecting χ and a (χ'=0.286 Δa). These initial values have been adjusted to the values reported in Table 5-7 to reproduce chain dimensions obtained from atomistic simulations of PEO and PPO single chains in water. In Figure 5-13A the

behaviors of gyration radius as function of molecular weight (MW) calculated using MD simulations of atomistic and particle field coarse-grained models of PEO and PPO are reported.

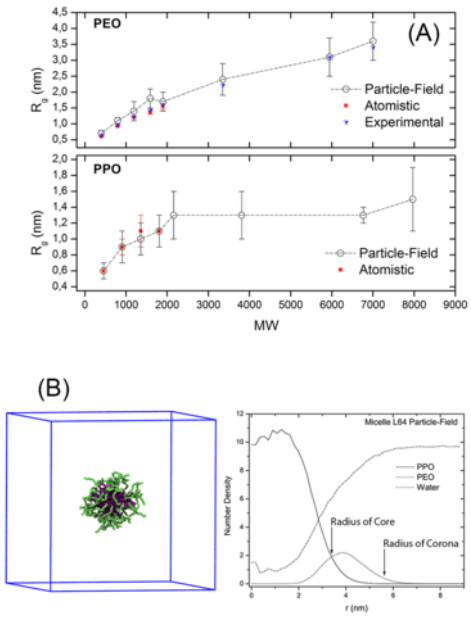

Figure 5-13. (A) Radius of gyration vs. molecular weight for PEO (upper) and PPO (bottom) chains in water. In the plots values obtained from atomistic (red squares), experiments (blue triangles) and coarse-grained MD-SCF models (empty circles) are compared. (B) Radial density profile calculated for a L64 micelle (system I) after 4.5 ms of MD-SCF simulation. Arrows indicate experimental values of core and corona radii.

A further validation of the proposed models has been done considering the size and the stability of micelles. In particular, the Pluronic L64 represented by the formula $(EO)_{13}$-$(PO)_{30}$-$(EO)_{13}$ has been considered. In Figure 5-13B, together with a

snapshot of simulated system I of the Table 5-8, the radial density profiles calculated for a L64 micelle having 38 block copolymer chains (corresponding to the experimental aggregation number) is reported. Experimental values of core and corona radius[8] are indicated by arrows in the plot.

Table 5-8. Simulated Systems

Systems	**Composition (no. of molecules)**					**Box size**	**Simulated time**
	L64	Water	DPPC	Embedded Molecule	Particle no.	(nm)	(μs)
I	38	222200	0	0	224328	30x30x30	6
II	38	222200	2812	0	258072	30x30x34	5
III[a]	38	222200	2812	5	258097	30x30x34	13
IV-A[b]	38	222200	2812	8	258096	30x30x34	5
IV-B[b]	38	222200	2812	8	258096	30x30x34	5
IV-C[b]	38	222200	2812	8	258096	30x30x34	6
IV-D[b]	38	222200	2812	8	258096	30x30x34	21
IV-E[b]	38	222200	2812	8	258096	30x30x34	15
IV-F[b]	38	222200	2812	8	258096	30x30x34	18
IV-G[b]	38	222200	2812	8	258096	30x30x34	18

[a]Embedded molecules used for this system are Ibuprofen. [b]System IV having embedded trimers of increasing hydrophobicity λ ranging from 0.16 (IV-A) to 1 (IV-G).

The radial density profiles of PO and EO blocks calculated from a simulation of a system I at 2.5 wt % of L64 in water well compare with the experimental values of core and corona radius obtained in the same conditions[8].

The critical micelle concentration (CMC) of the L64 model has been investigated considering the stability of the system as function of L64 concentration. In particular, fractions of assembled L64 chains have been calculated for systems at

different concentrations (Table 5-9). In Figure 5-14 the fraction of assembled L64 chains compared with the experimental value of the CMC are reported.

Table 5-9. Composition of systems used for the CMC calculation.[a]

System	Composition				Box Size
	no. L64	**no. Water**	**no. Particles**	**[mM]**	(nm)
A	19	223264	224328	1.122	30x30x30
B	9	223824	224328	0.532	30x30x30
C	6	223992	224328	0.354	30x30x30
D	5	224048	224328	0.295	30x30x30
E	4	224104	224328	0.236	30x30x30

[a]The experimental value of CMC reported by Alexandridis[6] is 0.344mM at 313 K.

From the plot of Figure 5-14 a good agreement with the value of 0.344 mM reported by Alexandridis[6] is clear. Further validations on micelles behavior (aggregation number) are reported in the supporting information section. The Pluronics model reported here give a correct reproduction of micellar and non micellar phases for Pluronics L62 and L64 as function of water concentration. In particular, the proposed models are able to correctly describe the different morphologies (such us hexagonal micellar, lamellar and complex interconnected) that have been found experimentally.[60]

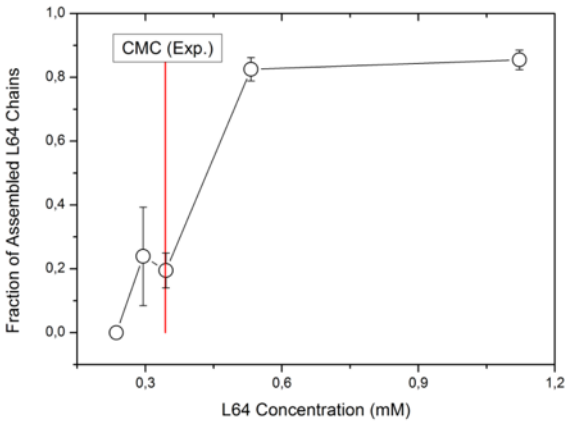

Figure 5-14 Fraction of assembled L64 chains at different concentrations, corresponding to the systems described in Table 5-9. Chains are counted as assembled if the number of neighboring chains is different from zero. The number of neighbors is calculated on the basis of a cut off criterion (1 nm) on the shorter distance between PO units of two different L64 chains. Each point in the plot corresponds to an average obtained from the last 100 ns of each simulation.

5-2.3 Micelle in contact with DPPC bilayer

The parameterization of the interaction parameters $\chi_{KK'}$ between EO and PO beads with phospholipids (Table 5-7) has been based on the reproduction of density profiles from reference atomistic simulations of PEO and PPO oligomers in contact with lipid bilayers[24]. An initial set of χ for EO and PO interactions with lipids head and tail have been obtained from a systematic DPD study of Groot on polymer-surfactant systems. In particular, set 1 (according to the notation of ref

59) for EO/lipid head and EO/lipid tail and intermediate values between sets 6 and 7 for PO/lipid head and PO/lipid tail, have been chosen. Further adjustments of these parameters have been done to better reproduce reference partial density profiles obtained from atomistic simulations.

According to the experimental data the diameter of the micelle is around 12 nm[8]. For this reason, in order to avoid large finite size effects, in the simulations reported here, a box size of 2.5 times larger than micelle diameter in the *x* and *y* directions (30 nm) and 2.8 in *z* direction (34 nm) has been considered. This implies simulations of quite large scale systems having more than 250.000 particles (see Table 5-8). In Figure 5-15A several snapshots of the MD simulation of system II made of one L64 micelle in contact with a DPPC lipid bilayer are reported (water beads are not shown for clarity). The simulation performed on the μs scale reveals that the behavior of the polymeric micelle is strongly influenced by the presence of lipid bilayer. In particular, from the beginning of the simulation chains are released from the micelle to the water phase and starting from about 1 μs insertions of triblock chains inside the bilayer can be observed. This behavior is in agreement with the experimental one reported by Pemboung et al.[61] In particular, ^{1}H-NMR and spin labeled probes results suggest a release of L64 chains

inside dodecylphosphocoline (DPC) and DPPC micelles.

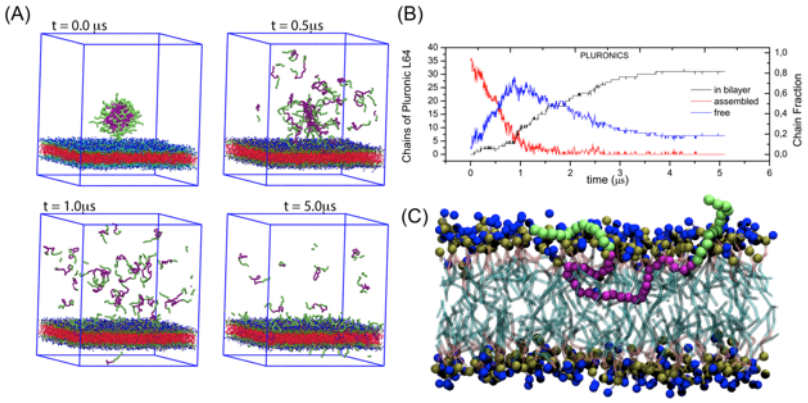

Figure 5-15 (A) Snapshots of system II (258.072 coarse-grained beads corresponding to ~ 3.000.000 of atoms) having a L64 micelle in contact with DPPC lipid bilayer (water beads are omitted for clarity) (B) Time behavior of L64 chains assembled as micelle (red curve), inside lipid bilayer (black curve) and in water (blue curve). L64 chains, for a given configuration, are counted as inside bilayer if at least one PO bead is located between the average heights of upper and lower lipid layers. The remaining chains are counted as free or assembled according to the number of neighboring chains (zero neighbors free chains, at least one neighbor assembled chains). The number of neighbors is calculated on the basis of a cut off value (1 nm) on the shortest distance between PO units of two different L64 chains. (C) Detail of insertion of a Pluronic L64 chain inside phospholipid bilayer. The green beads correspond to EO units, while the purple beads correspond to PO units. The aliphatic chains of phospholipids are shown in transparency. The head groups of DPPC are shown.

Simulations snapshots show that chains attach to the lipid bilayer inserting the segment made of PO beads in the hydrophobic portion of the bilayer. In Figure 5-14C a detail of an inserted L64 chain of system II is depicted. In agreement with the findings of Firestone et. al[62,63], chains are inserted partially inside the bilayer with the PPO block, while the PEO blocks point toward the water phase from the same side of the lipid bilayer. The chain release process continues until the micelle dissolves in the water phase. This behavior can be

ascribed to an effective concentration of L64 in the water phase lower than the CMC due to a subtraction of polymer chains from the micellar assembly and from water inside lipid bilayer. From the plot of Figure 5-15B is clear that in about 3 μs the L64 chains are unassembled with a fraction 0.2 present as free chains and the remaining L64 chains inserted inside the lipid bilayer.

For coarse-grained models, usually, the dynamics is faster because there is a reduced effective bead friction due to smaller energy barriers and/or a smoother energy landscapes. In order to connect the results with less coarse models (atomistic or CG but based on particle-particle potentials) or with experiments it is necessary to connect the timestep used in coarse-grained simulations and to derive a scaling factor for the time[64]. Methods to match time scales have been applied to quantitatively understand and predict dynamics of several systems by coarse-grained models using a comparison between dynamical properties calculated at coarse-grained and atomistic level. In particular, diffusion coefficients calculated from the coarse-grained and atomistic simulations can be compared. From comparison of diffusion coefficients a factor of about 15 can be obtained[56]. The complications in soft matter systems are the multitude of fluctuating energy barriers of similar height and a common problem is that usually all

barriers are not lowered in the exact same way that the ratios of transition times remain the same.

In order to better define a scaling factor for the process of a chain insertion into a lipid bilayer, a closer timescale connection can be done comparing the time needed for an insertion of a single chain using MD-SCF and MD using traditional models based on Lennard-Jones pair potentials. Ideally, the exchange process of L64 chains between the micelle and the lipid bilayer, reported in the present paper, can be divided in three elementary processes. In particular, we can consider three processes: Pluronic chain detachment from the micelle, chain diffusion in water, chain insertion into the lipid bilayer. Reasonably, the diffusion process is the slowest one and it governs the rate of the observed process. In order to prove this, we performed three independent simulations similar to the one reported in Figure 5-16. In particular, we analyzed the velocity of L64 chain insertion from the time behavior of z component (perpendicular to the bilayer plane) of the distance between the geometric center of the PPO block and the hydrophobic sector of the lipid bilayer. According to this analysis, chain insertion is fast (takes about 8-10 ns) and it shows similar velocities for both particle-particle and particle field simulations. More details about this are reported in the supporting information section.

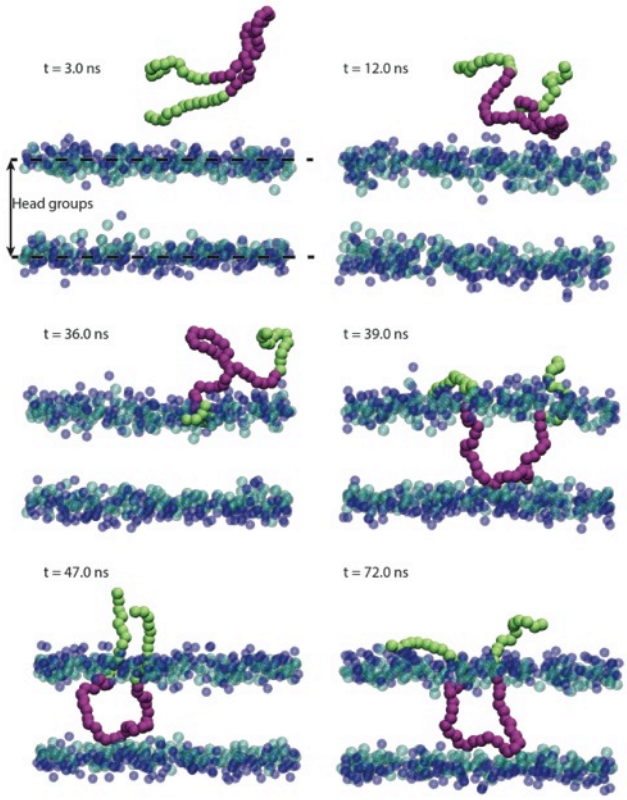

Figure 5-16. Snapshots of single L64 chain insertion process for an MD-SCF simulation. The insertion of PPO hydrophobic block is observed starting from 39 ns. The L64 chain after insertion shows the hydrophobic block inside the aliphatic region of phospholipid bilayer, while PEO blocks point toward the water phase from the same side.

We can reasonably conclude that the slowest process governing the chain exchange between the micelle and the bilayer is the diffusion of L64 chains. In this way, a reasonable estimate of the order of magnitude of the scaling factor, for the observed process, could be the ratio between diffusion coefficients of particle-particle and particle-field

simulations (a factor 15).

These feature allows to fully observe on the scale of our simulations the exchange of polymer chains between the micelle and the bilayer and the dissolution process of the micelle in presence of the lipid bilayer. Furthermore, equilibrium values of the distribution of L64 chains inserted into the bilayer and dissolved in water phase can be reached.

In absence of a lipid bilayer the micelle is stable. In particular, in Figure 5-17A, several snapshots of a MD simulation for 6 μs of a system having a L64 micelle in water (system I) are reported. Furthermore, the time behavior of radius of gyration of the micelle in water is reported in Figure 5-17B. Differently from system II the micelle is stable and an exchange of few chains between micelle and water phase is only observed.

In Figure 5-18A we report snapshots of system III, analogous to system II, but having four molecules of ibuprofene (IBU) encapsulated into hydrophobic core of the micelle. In Figure 5-12 the mapping scheme used of IBU molecule together with its chemical structure is reported. In particular, the isopropyl group has been modeled by a bead of type C, the benzene ring using three beads of type B (having the same χ parameters of beads of type C) and the carboxylic group (COOH) with a bead of type E (having the same χ parameters of beads of type

EO). Further details about intramolecular interactions (bonds and angles) of beads of type B and E are reported in Tables 5-5 and 5-6. The number of IBU molecules corresponds to 0.25wt% with respect to the quantity of L64. This value, as reported from Foster et al. is consistent with the aggregation number of 48 chains[3].

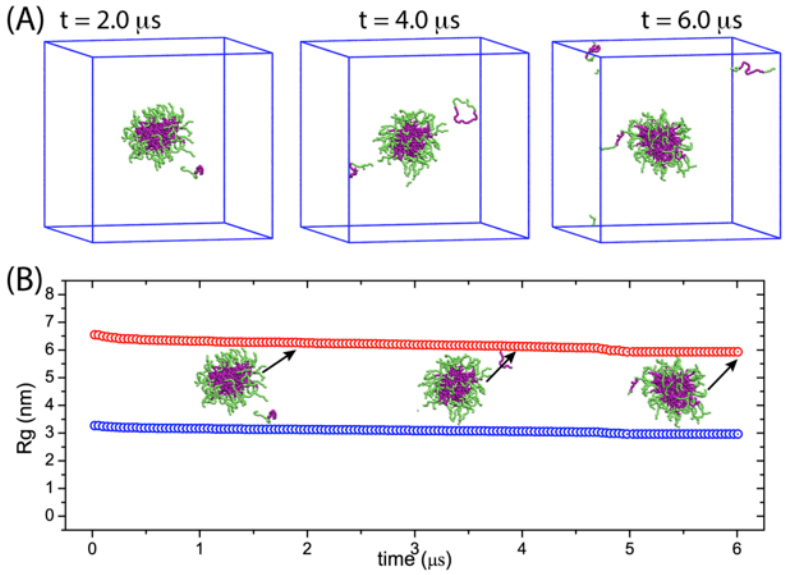

Figure 5-17. (A) Snapshots of system I having an L64 micelle in water (the beads of water are omitted for clarity). (B) Time behaviour of radius of gyration of L64 micelle in water. The red curve corresponds to the total radius of gyration of micelle while the blue curve corresponds to the radius of gyration of hydrophobic core. Snapshots of some configurations of the L64 micelle are shown at different times.

Similarly to the system II, previously described, after about 1μs (Figure 5-18B) the insertion of triblock chains into the bilayer takes place, but differently from the previous system

II, although a reduction of micelle size is observed (Figure 5-18C), the micellar assembly is not dissolved. In particular, after 5 μs the micellar aggregate becomes stable, and starting from 5 up to 8 μs only a slow repartition between chains free and in bilayer occurs. After 8 μs up to the end of simulation (about 5 μs) the system remains in equilibrium state.

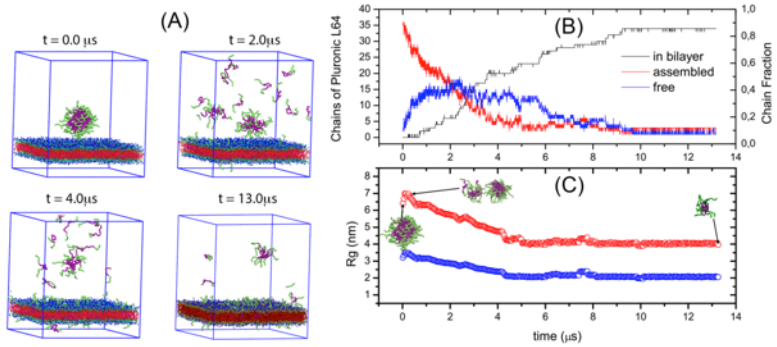

Figure 5-18. (A) Snapshots of system III (258.072 coarse-grained beads corresponding to ~3.000.000 of atoms) having an L64 micelle in contact with DPPC lipid bilayer (water beads are omitted for clarity) (B) Time behavior of L64 chains assembled as micelle (red curve), inside lipid bilayer (black curve) and in water (blue curve). For a complete definition of assembled, free and inside bilayer chains the reader can refer to the caption of Figure 5-14. (C) Time behaviour of radius of gyration of L64 micelle with ibuprofen molecules embedded in the hydrophobic core. Red curve corresponds to the total radius of gyration of micelle while the blue curve corresponds to the radius of gyration of hydrophobic core. Snapshots of relevant configuration of L64 micelle are shown at different times.

From these results it is clear that the hydrophobic nature of the encapsulated molecule influences the stability of the micellar assembly in the presence of a lipid bilayer. Small-angle neutron scattering and pulsed-field gradient stimulated-echo nuclear magnetic resonance (NMR) have shown that addition of hydrophobic molecules to solutions of Pluronics

and water changes the micellar structure. In particular, high hydrophobic molecule concentrations favor micellization, leading to an increase of aggregation numbers, fraction of polymer micellized, and core radius of the micelle.[3] This behavior can be ascribed to the hydrophobic nature of the molecule encapsulated inside the micelle and the resulting favorable interactions with the micelle core.

In our simulations the presence of the lipid bilayer changes the micelle aggregation state. In particular, in absence of IBU molecules, the 80% of L64 chains are adsorbed inside the DPPC bilayer. This causes a drop of L64 concentration in water phase and then a destabilization of micellar aggregate. In contrast, in the presence of hydrophobic IBU molecules, L64 chains are still assembled. This behavior shows a complex interplay between drug/micelle core and L64/bilayer interactions modulating the structural modifications of both micelle and bilayer. The main effect of the drug molecule seems to be related to its hydrophobicity.

Whit this in mind, further simulations aimed to study systematically the effect of the hydrophobicity of the encapsulated molecule have been performed. In particular, trimers of increasing hydrophobicity have been included in the hydrophobic core of the L64 micelles. The number of trimers included in the micelle core is 8, this choice has been

done to keep the number of particle similar to system III in which 5 IBU molecules (represented 5 by coarse-grained beads) have been included.

Table 5-10. Particle-field interaction matrix. $\chi_{AB} \times RT$(kJ mol^{-1}) for Systems IV.

λ	N	P	G	C	Water	EO	PO
1.00	9.00	13.50	6.30	0.00	33.75	7.80	-1.60
0.90	7.28	11.79	6.12	3.37	30.37	7.22	-0.98
0.80	5.57	10.80	5.94	7.75	27.00	6.64	-0.36
0.60	2.14	6.66	5.58	13.50	20.25	5.84	0.88
0.50	0.43	4.95	5.40	16.87	16.87	4.90	1.50
0.20	-4.70	-0.18	4.86	27.00	6.75	3.16	3.61
0.16	-5.39	-0.86	4.79	28.35	5.40	2.93	3.61

The hydrophobicity of the trimers has been varied changing linearly the χ parameters from the values assigned to the most hydrophobic particles (type C of lipid molecules) to those ones of water using a single parameter λ. In this way λ= 1 corresponds to a particle of type C and λ= 0 of a particle of water. For the intermediate cases, a linear combination has been used for all parameters. Simulations have been performed for seven different systems (IV-A to IV-G) having values of λ (0.16, 0.2, 0.5, 0.6, 0.8, 0.9, 1.0). In Table 5-10 the corresponding χ parameters for interaction between the beads of the trimers and the fields corresponding to the other particle types are reported.

In Figure 5-19 representative snapshots for some of these

systems have been reported. For trimers having λ larger than 0.5 the micelles are stable during MD simulations. After 10 μs the micelle aggregate does not change and it still remains stable up to the end of simulation. The behavior observed for values of λ lower than 0.5 is very similar to the one obtained for an "empty" micelle.

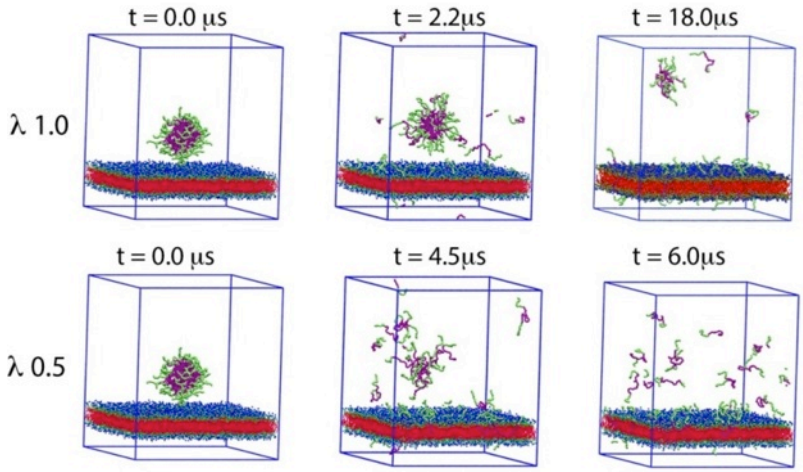

Figure 5-19. Snapshots of systems IV (258.072 coarse-grained beads corresponding to ~3.000.000 of atoms) at different values of λ having an L64 micelle in contact with DPPC lipid bilayer.

For lower values of λ (from 0.16 to 0.2) after about 10 ns all the inserted molecules diffuse out from the micelle and are stably present in the water phase. This is not surprising because the properties of the beads forming trimers at these values of λ are very close to water. In the case of λ = 0.5 a partial release of molecules is observed in the water phase,

after 4 μs the number of trimers included in the micelle is 2. For values larger than 0.5 all the included trimers are stably inside the micelle from the beginning to the end of the simulation. In Figure 5-20 the time behavior of L64 chains distributions inside the bilayer, assembled and free are reported for all systems with λ larger than 0.5 (0.6, 0.8, 0.9, 1.0). The plots of other systems are reported in the supporting information section.

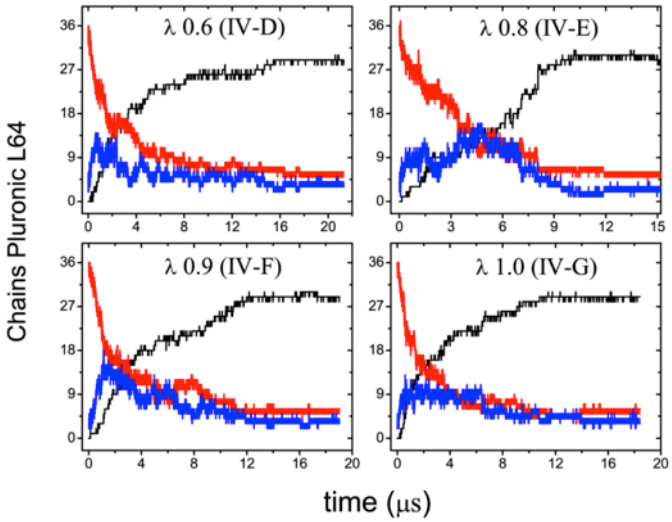

Figure 5-20. Time behaviour for systems IV D-G of L64 chains assembled as micelle (red curve), inside bilayer (black), in water (blue).

We observe that higher is the hydrophobicity and slower is the chain release process from the micelle to the water phase. In particular, for the systems at λ=0.16 and 0.20 the micelle dissolution process takes 1 and 2μs, respectively. Differently,

the systems having trimers with λ=0.5 take longer (between 4 and 5μs) to reach the equilibrium. Micelles including trimers of larger hydrophobicity (λ from 0.6 to 1.0) take 8-12 μs, depending on the system, to reach equilibrium. After that time the micelles still remain stable and slow process of chains repartition between water and lipid bilayer occurs.

It is worth noting that an increase of hydrophobicity corresponds to an increase of assembled chains. It is interesting to observe that the radius of the micelle shows an abrupt increase around λ=0.6 (Figure 5-21A). In particular, when going from λ=0.5 to λ=0.6, an increase in the micelle radius of about nine times can be obtained. Moreover, we observe that the number of assembled chains, for systems in which the micellar aggregate is present, does not change significantly (Figure 5-21B).

To better understand the role played by hydrophobicity in the shape and size of the micellar aggregate, radial density profiles have been performed. In particular, for the system III, and systems IV-(D,G), we calculate the radial density distribution on assembled chains at equilibrium together with IBU or trimer molecules (Figure 5-22). As results from the plots, the radial distribution of chains embedding IBU or trimer molecules, does not change significantly with hydrophobicity.

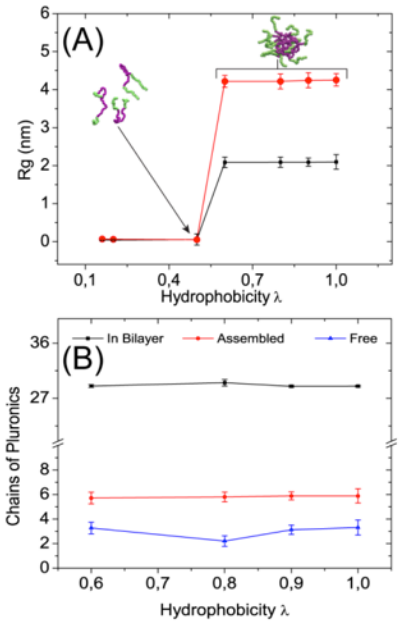

Figure 5-21. (A) Behavior of the radius of gyration of L64 micelle at different value of λ. Total radius (red curve), hydrophobic core radius (black curve). (B) Behavior of assembled (red curve), in bilayer (black curve) and free (blue curve) L64 chains as functions of hydrophobicity (λ) of encapsulated trimers.

In particular, for both, hydrophobic EO blocks and hydrophilic PO block, only slightly differences between different systems have been found (Figure 5-22A-B). Also for the IBU and trimer molecules inside the PO core the radial distributions have been calculated. From the comparison, in Figure 5-22C, we found that the position of IBU or trimer molecules inside the PO core is almost the same for all systems. In the supporting information section the density profile of all systems discussed below are reported.

In Figure 5-23 some of density profiles of lipid bilayer have been reported. In particular we compared the density profiles of the system II (without IBU), system III (with IBU molecules inside micelle) and system IV-G (with trimer molecules having λ=1.0).

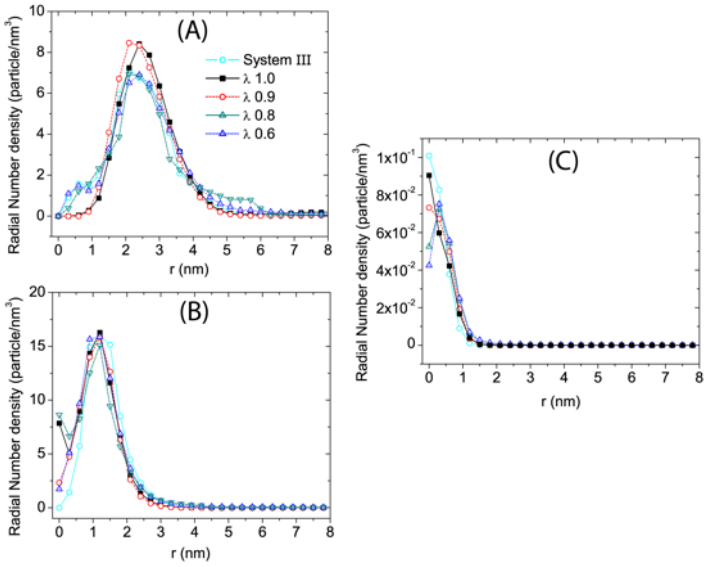

Figure 5-22. Radial density profile of: (A) EO blocks, (B) PO block, (C) IBU and trimer embedded molecules. Each profile is calculated with respect to the centre of the mass of IBU or trimer molecules. The profiles have been calculated from the data during the last 500.0 ns of the equilibrium state of each system.

Such profiles have been calculated after each system goes in equilibrium. From the plots we observe that the lipid bilayers have not strong distortion of the profile. The distributions of the head and tails of the lipids are very close each other and seem to be insensitive to the hydrophobicity. About the

distribution of pluronic chains inside the lipid bilayer we have the same behavior. No significant difference between the systems has been found (in the supporting information section are reported the others systems).

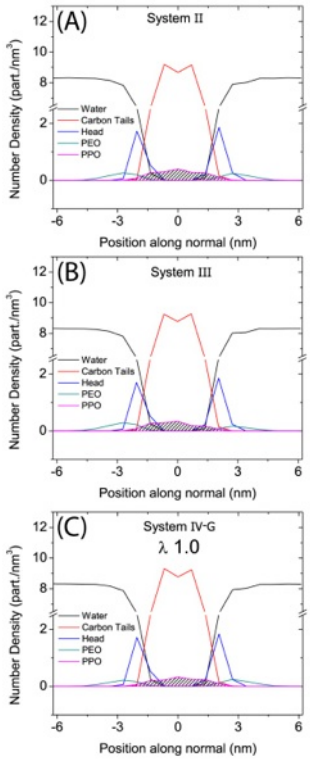

Figure 5-23. Number density profiles calculated for: (A) system II, (B) system III and (C) system IV-G with λ = 1.0. The density profiles have been calculated for the data during the last 500.0 ns of the equilibrium state of each system.

5-3 Conclusions

A hybrid PF coarse-grained model has been reported for Pluronic L62 and L64. The reproduction of morphologies depending on the concentration and temperature for water mixture solution of polymer has been tested. In particular, micellar and non micellar morphologies reproduced by the model have been found in agreement with the experimental phase diagram. Furthermore, the reproduction of the hexagonal morphology specific for the Pluronic L64 has been obtained. In fact, in a narrow range of composition, between 46~55 wt%, the hexagonal phase is stable for the Pluronic L64 and, at the same composition, is absent in the Pluronic L62 phase diagram. At polymer content higher than 52 wt% we obtain a lamellar morphology for both, L62 and L64. In particular, at 90 wt% of L64 we observe also a complex lamellar morphology. The features of the proposed model allows the possibility to link the CG configurations to the full atomistic configurations, due to the mapping 1:3 and 1:4 for EO and PO beads. An example of reverse mapping of the peculiar hexagonal morphology of Pluronic L64 has been shown to this aim.

Moreover, the development and validation of coarse-grained models of Pluronics that are able to describe micellar assemblies and their interactions with phospholipids have been reported. Molecular dynamics simulations of large scale coarse-grained models (typically ~260.000 coarse-grained beads corresponding to ~3.000.000 of atoms) of Pluronic L64 block copolymers micelles and their interactions with lipid bilayers suitable to reach time (μs) and length (nm) scales relevant for the self assembly phenomena for several systems have been reported. Simulations show, in agreement with several previous experiments, a release of triblock chains from the micelle inside the bilayer. This release changes the size of the micelles. The presence of a drug molecule inside the hydrophobic core of the micelle has a strong influence on this process. In particular, the micelle stability is a result of a complex interplay between drug/core and block-co-polymer/bilayer interactions modulating the structural modifications of both micelle and bilayer. An interesting finding is that the micelle size shows an abrupt increase (about nine times) in a very narrow range of encapsulated molecule hydrophobicity. Changes in aggregate size and structure are critical in determining the mechanism of drug delivery from micellar structures. According to the paradigm of EPR effect, the understanding of the physico-chemical

mechanism of the drug vector size and the important role of drug micelle interactions in it, is fundamental to improve the design of systems for cancer therapy. The models presented in this study are not generic, but still very close to atomistic ones and are able to represent specific molecular architectures. This important feature opens the way to a detailed understanding of the molecular mechanisms underlying the drug delivery processes.

References:

(1) Schmolka, I. *J Am Oil Chem Soc* **1991**, *68*, 206.
(2) Kabanov, A. B.; Batrakova, E. V.; Alakhov, V. Y. *Adv. Drug Delivery Rev*. **2002**, *54*, 759.
(3) Foster, B.; Cosgrove, T.; Hammouda, B. *Langmuir* **2009**, *25*, 6760.
(4) Peetla, C.; Stine, A.; Labhasetwar, V. *Molecular Pharmaceutics* **2009**, *6*, 1264.
(5) Turro, N. J.; Baretz, B. H.; Kuo, P. L. *Macromolecules* **1984**, *17*, 1321.
(6) Alexandridis, P.; Holzwarth, J. F.; Hatton, T. A. *Macromolecules* **1994**, *27*, 2414.
(7) Yang, L.; Alexandridis, P. *Langmuir* **2000**, *16*, 4819.
(8) Yang, L.; Alexandridis, P.; Steytler, D. C.; Kositza, M. J.; Holzwarth, J. F. *Langmuir* **2000**, *16*, 8555.
(9) Alexandridis, P.; Zhou, D.; Khan, A. *Langmuir* **1996**, *12*, 2690.
(10) Zhou, H.-X.; Rivas, G.; Minton, A. P. *Annual Review of Biophysics* **2008**, *37*, 375.
(11) Zhou, F.; Xing, D.; Wu, B.; Wu, S.; Ou, Z.; Chen, W. R. *Nano Letters* **2010**, *10*, 1677.
(12) Brown, W.; Schillen, K.; Almgren, M.; Hvidt, S.; Bahadur, P. *The Journal of Physical Chemistry* **1991**, *95*, 1850.
(13) Li, D.-W.; Liu, X. Y.; Feng, Y. P. *The Journal of Physical Chemistry B* **2004**, *108*, 11206.
(14) Liu, X.; He, F.; Salas, C.; Pasquinelli, M. A.; Genzer, J.; Rojas, O. J. *The Journal of Physical Chemistry B* **2011**, *116*, 1289.
(15) van Vlimmeren, B. A. C.; Maurits, N. M.; Zvelindovsky, A. V.; Sevink, G. J. A.; Fraaije, J. G. E. M. *Macromolecules* **1999**, *32*, 646.
(16) Smith, G. D.; Borodin, O.; Bedrov, D. *Journal of Computational Chemistry* **2002**, *23*, 1480.
(17) Faller, R.; Marrink, S.-J. *Langmuir* **2004**, *20*, 7686.
(18) Milano, G.; Kawakatsu, T. *Journal of Chemical Physics* **2009**, *130*, 214106.
(19) Milano, G.; Kawakatsu, T. *Journal of Chemical Physics* **2010**, *133*, 214102.
(20) Hezaveh, S.; Samanta, S.; Milano, G.; Roccatano, D. *J. Chem. Phys*. **2011**, *135*, 16450.
(21) Hezaveh, S.; Samanta, S.; De Nicola, A.; Milano, G.; Roccatano, D. *The Journal of Physical Chemistry B* **2012**, *116*, 14333.
(22) Hezaveh, S.; Samanta, S.; Milano, G.; Roccatano, D. *J. Chem.*

Phys. **2012**, *136*, 124901.
(23) Samanta, S.; Hezaveh, S.; Milano, G.; Roccatano, D. *The Journal of Physical Chemistry B* **2012**, *116*, 9286.
(24) Samanta, S.; Hezaveh, S.; Milano, G.; Roccatano, D. *The Journal of Physical Chemistry B* **2012**, *116*, 5141.
(25) Alexandridis, P.; Yang, L. *Macromolecules* **2000**, *33*, 5574.
(26) Wu, G.; Chu, B.; Schneider, D. K. *The Journal of Physical Chemistry* **1995**, *99*, 5094.
(27) Linse, P. *Macromolecules* **1994**, *27*, 6404.
(28) Malmsten, M.; Lindman, B. *Macromolecules* **1992**, *25*, 5440.
(29) Chu, B. *Langmuir* **1995**, *11*, 414.
(30) Santangelo, G.; Di Matteo, A.; Müller-Plathe, F.; Milano, G. *Journal of Physical Chemistry B* **2007**, *111*, 2765.
(31) Chen, X.; Carbone, P.; Santangelo, G.; Di Matteo, A.; Milano, G.; Muller-Plathe, F. *Physical Chemistry Chemical Physics* **2009**, *11*, 1977.
(32) Duncan, R.; Gaspar, R. *Molecular Pharmaceutics* **2011**, *8*, 2101.
(33) Duncan, R. *Current Opinion in Biotechnology* **2011**, *22*, 492.
(34) Duncan, R. *Nat. Rev. Drug Discovery* **2003**, *2*, 347.
(35) Duncan, R. *Nat. Rev. Cancer* **2006**, *6*, 688.
(36) Pasut, G.; Varonese, F. M. *Adv. Drug Delivery Rev*. **2009**, *61*, 1177.
(37) Matsumura, Y. *Adv. Drug Delivery Rev*. **2008**, *60*, 899.
(38) Matsumura, Y.; Kataoka, K. *Cancer Sci*. **2009**, *100*, 572.
(39) Farrel, D.; Ptak, K.; Panaro, N. J.; Grodzinski, P. *Pharmaceutical research* **2011**, *28*, 273.
(40) Allen, T. M. *Nat. Rev. Drug Discovery* **2002**, *2*, 750.
(41) Torchilin, V. P. *Nat. Rev. Drug Discovery* **2005**, *4*, 145.
(42) Zamboni, W. C. *Clin. Cancer Res*. **2005**, *11*, 8230.
(43) Upadhyay, K. K.; Agrawal, H. G.; Upadhyay, C.; Schatz, C.; Le Meins, J. F.; Misra, A.; Lecommandoux, S. *Crit. Rev. Ther Drug Carrier Syst*. **2009**, *26*, 157.
(44) Matsumura, Y.; Maeda, H. *Cancer Res*. **1986**, *6*, 6387.
(45) Kabanov, A. B.; Chekhonin, V. P.; Alakhov, V.; Batrakova, E. V.; Lebedev, A. S.; Melik-Nubarov, N. S.; Arzhakov, S. A.; Levashov, A. V.; Morozov, G. V.; Severin, E. S. *FEBS Lett*. **1989**, *258*, 343.
(46) Alakhov, V. Y.; Kabanov, A. V. *Expert Opin. Investing. Drugs* **1998**, *7*, 1453.
(47) Exner, A. A.; Krupka, T. M.; Sherrer, K.; Teets, J. M. *J. Control. Release* **2005**, *106*, 188.
(48) Hans, M.; Shimoni, K.; Danino, D.; Siegel, S. J.; Lowman, A. *Biomacromolecules* **2005**, *6*, 2708.
(49) Alakhov, V.; Klinski, E.; Li, S.; Pietrzynski, G.; Venne, A.;

Batrakova, E.; Bronitch, T.; Kabanov, A. *Colloids and Surfaces B: Biointerfaces* **1999**, *16*, 113.
(50) Pal, S.; Milano, G.; Roccatano, D. *Journal of Physical Chemistry B* **2006**, *110*, 26170.
(51) Nawaz, S.; Redhead, M.; Mantovani, G.; Alexander, C.; Bosquillon, C.; Carbone, P. *Soft Matter* **2012**, *8*, 6744.
(52) Redhead, M.; Mantovani, G.; Nawaz, S.; Carbone, P.; Gorecki, D. C.; Alexander, C.; Bosquillon, C. *Pharmaceutical research* **2012**, *29*, 1908.
(53) Fuchs, P. F. J.; Hansen, H. S.; Huenenberger, P. H.; Horta, B. A. C. *Journal Of Chemical Theory And Computation* **2012**, *8*, 3943.
(54) Homberg, M.; Muller, M. *The Journal of Chemical Physics* **2010**, *132*, 155104.
(55) Sevink, G. J. A.; Charlaganov, M.; Fraaije, J. G. E. M. *Soft Matter* **2013**, *9*, 2816.
(56) De Nicola, A.; Zhao, Y.; Kawakatsu, T.; Roccatano, D.; Milano, G. *Journal of Chemical Theory and Computation* **2011**, *7*, 2947.
(57) De Nicola, A.; Zhao, Y.; Kawakatsu, T.; Roccatano, D.; Milano, G. *Theoretical Chemistry Accounts* **2012**, *131*, 1167.
(58) Cao, X.; Xu, G.; Li, Y.; Zhang, Z. *The Journal of Physical Chemistry A* **2005**, *109*, 10418.
(59) Groot, R. D.; Warren, P. B. *The Journal of Chemical Physics* **1997**, *107*, 4423.
(60) De Nicola, A.; Milano, G.; Kawakatsu , T. *Macromolecular Chemistry and Physics* **2013**, *214*, 1940.
(61) Pembouong, G.; Morellet, N.; Kral, T.; Hof, M.; Scherman, D.; Bureau, M.-F.; Mignet, N. *Journal of Controlled Release* **2011**, *151*, 57.
(62) Firestone, M. A.; Seifert, S. *Biomacromolecules* **2005**, *6*, 2678.
(63) Firestone, M. A.; Wolf, A. C.; Seifert, S. *Biomacromolecules* **2003**, *4*, 1539.
(64) Fritz, D.; Koschke, K.; Harmandaris, V. A.; van der Vegt, N. F.; Kremer, K. *Phys Chem Chem Phys* **2011**, *13*, 10412.

6
Conclusions

The main result of this thesis is to show how the particle-field approach is able to reproduce the effect of chemical details in several systems properties. One of the questions I tried to answer from the beginning of the doctoral project is:

"Are particle-field models able to keep chemical details?"

This is not a trivial question because the chemical details are extremely important in specific models. The interactions that regulate the protein folding are a typical example of specific interactions. Only models with chemical details can keep the peculiar aspects of specific phenomena.

I think that the answer to this question, considering all results shown in the previous Chapters, is "yes".

For example, the models of phospholipids, reported in the Chapter 4, are able to describe correctly an important structural property like the correct reproduction of the thickness of the bilayer, as result of small differences chemical structures. Moreover, the proposed model is also able to correctly describe the phase behaviour at different

water contents.

Pluronic particle-field models give another example illustrating the role of chemical specificity on a larger scale such as the phase structures. In particular, the reproduction of the hexagonal morphology, specific for the Pluronic L64, has been obtained. This result is not obvious because only in a narrow range of composition, between 46~55 wt%, the hexagonal phase is stable for the Pluronic L64. At the same composition, instead, such phase is completely absent for Pluronic L62. It is worth noting that the difference between Pluronic L64 and L62 consists in a different length of PEO and PPO blocks. As shown in the Chapter 5, this slight difference is well reproduced by the proposed model.

Differently from pure Self Consistent Field (SCF) approach, in the hybrid MD-SCF scheme the particles are an explicit ingredient of the model. This implies that the density field and then intermolecular interaction potential, depending on the particles positions, is correlated in a straightforward way to the chemical structure of the model. With this in mind, is reasonable how we can reproduce very fine local correlations also in atomistic models. In fact, as shown in Chapter 3, by tuning the mesh size and then the density field resolution, it is possible to describe with good approximation both the local rearrangements of an atomistic structure of a polymer melt,

and to allow, at the same time, a fast relaxation of polymer chains with high molecular weight. Moreover, the explicit presence of particles in the models, gives us the possibility to reintroduce, by a reverse mapping procedure, the local pair-wise interactions that are replaced by particle-field ones. This capability is very important, basically because the pure SCF methods have not such possibility, not having explicit particles.

MD-SCF techniques are less expensive, from the computational point of view, this enable to simulate a very large system, on time scale not easily accessible to other conventional techniques with comparable chemical details. This allows us to study phenomena, with molecular detail, on the scales of μs and hundreds of nm. An example of such system, Pluronic micelle interacting with phospholipid bilayer, has been discussed in the Chapter 5.

In conclusion, the MD-SCF approach opens a route towards study complex phenomena on large time and length scales.

Appendix A

A.1 Reverse-mapping Procedure

To further details about the reverse-mapping procedure can be found at the references[1,2].

Basically, the reverse-mapping procedure is founded on rigid superposition of the target atomistic model on the coarse-grained ones obtained from the mesoscale simulations. A library of atomistic structure of the target molecule is built by independent atomistic simulation. Then, for a given coarse-grained molecule several trial of atomistic structures, belonging to the library, are superimposed and the root mean square deviation (RMSD) between the centre of the coarse-grained beads and the corresponding atomic site is calculated. If the RMSD of a trial is less than the chosen tolerance (a reasonable value of tolerance is 10^{-2} nm), the structure is accepted and the CG molecule is replaced. The procedure is complete until all CG molecules are replaced by atomistic configurations. The flow chart of the reverse-mapping procedure is reported in Figure A1.

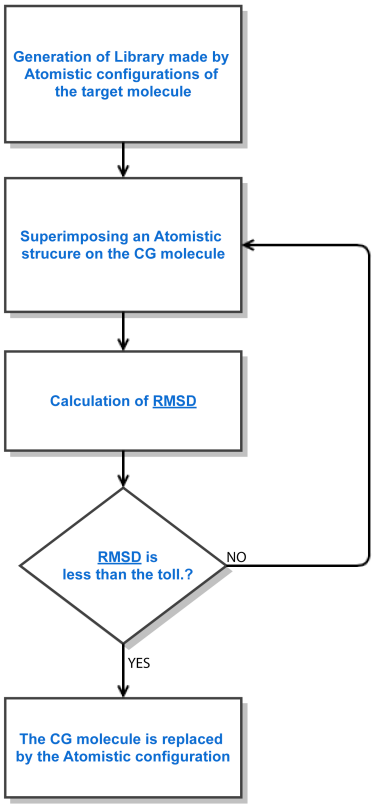

Figure A1. Flow chart of the reverse-mapping procedure

A.2 Superposition Method

As above-mentioned the reverse-mapping strategy is based on the Structure superposition methods. In particular the superposition is obtained by rigid rotation of atomistic structures on the coarse-grained ones. Such methods can give a quantitative measure of shape similarity as the RMSD of distances between corresponding atoms.

Finding the optimal orthogonal transformation can solve the Structure superposition problem. This implies that the rotation matrix **T** and a translation vector that will superimpose two sets of coordinates should be determined. A possible method, that we chose, is based on quaternions introduced by Kearsley[3].

Quaternions can be viewed as a non-commutative extension of complex numbers. They have been already used to describe rotations in classical mechanics as well as quantum and relativistic physics. It can be shown that a quaternion can be used as a rotation operator for a vector. The vector can be considered as a quaternion with zero scalar components:

$$(0,\mathbf{r}') = \hat{q}^{-1}(0,\mathbf{r})\hat{q} = \left(0, q_1^2\mathbf{r} + (\mathbf{r}\cdot\mathbf{q})\mathbf{q} + 2q_1(\mathbf{r}\wedge\mathbf{q})\right)$$

$$\mathbf{r}' = \mathbf{T}\mathbf{r}$$

$$= \begin{pmatrix} q_1^2+q_2^2-q_3^2-q_4^2 & 2(q_2q_3+q_1q_4) & 2(q_2q_4+q_1q_3) \\ 2(q_2q_3-q_1q_4) & q_1^2+q_3^2-q_2^2-q_4^2 & 2(q_3q_4+q_1q_2) \\ 2(q_2q_4+q_1q_3) & 2(q_3q_4-q_1q_3) & q_1^2+q_4^2-q_2^2-q_3^2 \end{pmatrix} \begin{pmatrix} x \\ y \\ z \end{pmatrix}.$$

As Kearsley[3] has shown, the rotation matrices that minimize the sum of the squared distances between corresponding particles for two structures can be calculated by posing a constrained least-squares problem in terms of quaternion parameters.

Considering: $x_- = x' - x$; $x_+ = x' + x$ and in a similar way we define y_, y+, z_ and z+, the resulting equations can be rewritten in the following eigenvalue problem:

$$\begin{pmatrix} \sum(x_-^2+y_-^2+z_-^2) & \sum(x_+z_- - y_-z_+) & \sum(x_-z_+ - x_+z_-) & \sum(x_+y_- - x_-y_+) \\ \sum(y_+z_- - y_-z_+) & \sum(x_-^2+y_+^2+z_+^2) & \sum(x_-y_- - x_+y_+) & \sum(x_-z_- - x_+z_+) \\ \sum(x_-z_+ - x_+z_-) & \sum(x_-z_- - x_+y_+) & \sum(x_+^2+y_-^2+z_+^2) & \sum(y_-z_- - y_+z_+) \\ \sum(x_+z_- - x_-y_+) & \sum(x_-z_- - x_+z_+) & \sum(y_-z_- - y_+z_+) & \sum(x_+^2+y_+^2+z_-^2) \end{pmatrix} \times \begin{pmatrix} q_1 \\ q_2 \\ q_3 \\ q_4 \end{pmatrix} = \lambda \begin{pmatrix} q_1 \\ q_2 \\ q_3 \\ q_4 \end{pmatrix}$$

In the elements of 4 x 4 of the equation above, the summation is made over all centers to superimpose. The eigenvalues, obtained from the diagonalization of the matrix, give the value of the residual for the rotation produced by application of the corresponding eigenvector. The RMSD is given by $(\lambda/n)^{1/2}$ where *n* is the number of atoms compared. The smallest eigenvalue gives the rotations that minimize the sum of the distances between all corresponding atoms.

A.3 Reverse-mapping code

To apply the reverse-mapping procedure described in the section A.1, specific code has been developed. The interface of the code has been completely rewritten to work as an external code. The subroutines to evaluate the superposition between atoms have been taken from the TINKER

(http://dasher.wustl.edu/ffe/) and have been written by Jay William Ponder. The complete algorithm is reported below.

```
c ################################################
c ##  written  by:  Antonio De Nicola  ##
c ################################################

  Program ReverseMapping
      IMPLICIT NONE
      include 'sizes.i'
      include 'align.i'
      include 'inform.i'

      Real*8 toll,rmsimp,c1,c2,c3,c4,c5,c6, toll1
      Real*8 x1(maxatm),y1(maxatm),z1(maxatm)
      Real*8 x2(maxatm),y2(maxatm),z2(maxatm)
      Real*8 MSE,MSEx,MSEy,MSEz,sump,p(maxatm),MSEmax
      Integer i,j,ind,n1,n2,k,nm,natomo(maxatm),ind2,
      Integer m, stbk, frms, cnt1, cnt2
      Character*5 ch1(maxatm),ch2(maxatm)
      Integer nmcg, natomocg,count, mol1, mol2
      Character*5 ch1cg,ch2cg


      integer argcount, IARGC
      character*80 wq_char
      character*80 filein0, filein1, param, fileout

      argcount = IARGC()

      do i=1,argcount
         call getarg(i,wq_char)
         if(INDEX(wq_char,'--help').ne.0) then
           write(6,*) '-t1 Atomistic traj'
           write(6,*) '-t2 CG configuration'
           write(6,*) '-param parameter file'
```

```
      write(6,*) '-toll tollerance (nm)'
      write(6,*) '-out output configuration (gro format)'
      write(6,*) '-----parameter file ------------------'
      write(6,*) 'part_CG, mol_CG'
      write(6,*) 'part_atomistic, mol_atomistic'
      write(6,*) 'number of sites to fit'
      write(6,*) 'CG_ind, atomistic_ind, w_fit'
      goto 30
    endif
    if(INDEX(wq_char,'-toll').ne.0) then
      call getarg(i+1,wq_char)
      read(wq_char,*) toll
    end if
    if(INDEX(wq_char,'-t1').ne.0) then
      call getarg(i+1,wq_char)
      read(wq_char,*)  filein1
    end if
    if(INDEX(wq_char,'-t2').ne.0) then
      call getarg(i+1,wq_char)
      read(wq_char,*)  filein0
    end if
    if(INDEX(wq_char,'-out').ne.0) then
      call getarg(i+1,wq_char)
      read(wq_char,*)  fileout
    end if
    if(INDEX(wq_char,'-param').ne.0) then
      call getarg(i+1,wq_char)
      read(wq_char,*) param
    end if
  enddo

open(1,file=fileout, status='unknown')
open(2, file=filein0, status="old")
open(3, file=filein1, status="old")
open(4, file=param, status="old")
open(7, file='log.txt', status='unknown')

read(4,*) n1, mol1
```

```
      read(4,*) n2, mol2, frms
      read(4,*) nfit

      do i=1,nfit
        ifit(1,i)=0
        ifit(2,i)=0
        wfit(i)=1
      end do

      do i = 1, nfit
         read(4,*) ifit(1,i), ifit(2,i), wfit(i)
      enddo



      write(1,400) 'TRITON'
      write(1,500) n2*mol1

      stbk = 0
      cnt1 = 0
      cnt2 = 0

      read(2,*)
      read(2,*)
      write(7,*)' Mol.   toll,    new-toll,     RMS,    atm.
struct.'
      do m = 1, mol1
         stbk = 0
         toll1 = toll
         do i=1, n1
           read(2,100)
nmcg,ch1cg,ch2cg,natomocg,x1(i),y1(i),z1(i)
c          write(*,100)
nmcg,ch1cg,ch2cg,natomocg,x1(i),y1(i),z1(i)
         end do
40       rewind 3
         do k = 1, frms
           read(3,*)
           read(3,*)
```

```
           do l = 1, mol2

             do j = 1, n2
                read(3,100)
nm,ch1(j),ch2(j),natomo(j),x2(j),y2(j),z2(j)
             end do

             if(stbk.lt.1)then
               call impose(n1,x1,y1,z1,n2,x2,y2,z2,rmsimp)
             endif

             if(rmsimp.le.toll1.and.stbk.lt.1)then
                do j=1,n2
                   write(1,300) nmcg,ch1(j),ch2(j),j+((m-
1)*n2),
     $                          x2(j),y2(j),z2(j)
                end do
                write(7,700) m, toll, toll1, rmsimp, k
c               write(*,*)
                write(*,*) 'Melecule CG nr.:', m
c               write(*,*) 'Tollerance (nm):', toll1
c               write(*,*) 'Current RMS:', rmsimp
c               write(*,*) 'Atomist str. in frame:', k
                write(*,*) '* * * backmapped * * *'
                stbk = 1
                cnt1 = cnt1 + 1
             endif
           enddo
           read(3,*)
20       enddo
             if(stbk.eq.0)then
c              write(*,*) 'Molecule', m,' * * * NOT BACKMAPPED
* * *'
               cnt2 = cnt2 + 1
               toll1=toll1 + 0.01d00
c              write(*,*) 'New toll.', toll1
               go to 40
             endif
```

```
      enddo
      read(2,600) c1,c2,c3
      write(1,600) c1,c2,c3

      Close(1)
      Close(2)
      Close(3)


      write(*,*)'-------------------------------------'
      write(*,*)' END '


100   Format(I5,2A5,I5,3F8.3,3F8.3)
300   Format(I5,2A5,I5,3F8.3)
200   Format(F8.1,6F8.4)
400   Format(A3)
500   Format(I8)
600   Format(3F10.5)
700   Format(i5, 3f8.4, 3x, i5)

30    end Program

c     ################################################
c     ##  COPYRIGHT (C)  1990  by  Jay William Ponder  ##
c     ##              All Rights Reserved              ##
c     ################################################
c
c
#################################################################
c     ##
##
c     ##  subroutine center  --  superimpose structure
centroids  ##
c     ##
##
c
#################################################################
```

```
c
c
c     "center" moves the weighted centroid of each coordinate
c     set to the origin during least squares superposition
c
c
      subroutine center
(n1,x1,y1,z1,n2,x2,y2,z2,xmid,ymid,zmid)
      implicit none
      include 'sizes.i'
      include 'align.i'
      integer i,k,n1,n2
      real*8 weigh,norm
      real*8 xmid,ymid,zmid
      real*8 x1(*),x2(*)
      real*8 y1(*),y2(*)
      real*8 z1(*),z2(*)
c
c
c     find the weighted centroid of the second
c     structure and translate it to the origin
c
      xmid = 0.0d0
      ymid = 0.0d0
      zmid = 0.0d0
      norm = 0.0d0
      do i = 1, nfit
         k = ifit(2,i)
         weigh = wfit(i)
         xmid = xmid + x2(k)*weigh
         ymid = ymid + y2(k)*weigh
         zmid = zmid + z2(k)*weigh
         norm = norm + weigh
      end do
      xmid = xmid / norm
      ymid = ymid / norm
      zmid = zmid / norm
      do i = 1, n2
```

```
         x2(i) = x2(i) - xmid
         y2(i) = y2(i) - ymid
         z2(i) = z2(i) - zmid
      end do
c
c     now repeat for the first structure, note
c     that this centroid position gets returned
c
      xmid = 0.0d0
      ymid = 0.0d0
      zmid = 0.0d0
      norm = 0.0d0
      do i = 1, nfit
         k = ifit(1,i)
         weigh = wfit(i)
         xmid = xmid + x1(k)*weigh
         ymid = ymid + y1(k)*weigh
         zmid = zmid + z1(k)*weigh
         norm = norm + weigh
      end do
      xmid = xmid / norm
      ymid = ymid / norm
      zmid = zmid / norm
      do i = 1, n1
         x1(i) = x1(i) - xmid
         y1(i) = y1(i) - ymid
         z1(i) = z1(i) - zmid
      end do
      return
      end
c     ##
##
c     ##  subroutine impose  --  superimpose two coordinate
sets  ##
c     ##
##
c
```

```
#############################################################
c
c
c     "impose" performs the least squares best superposition
c     of two atomic coordinate sets via a quaternion method;
c     upon return, the first coordinate set is unchanged while
c     the second set is translated and rotated to give best
fit;
c     the final root mean square fit is returned in "rmsvalue"
c
c
      subroutine impose(n1,x1,y1,z1,n2,x2,y2,z2,rmsvalue)
      implicit none
      include 'sizes.i'
      include 'align.i'
      include 'inform.i'
      include 'iounit.i'
      integer i,n1,n2
      real*8 xmid,ymid,zmid
      real*8 rmsvalue,rmsfit
      real*8 x1(*),x2(*)
      real*8 y1(*),y2(*)
      real*8 z1(*),z2(*)
c
c
c     superimpose the full structures if not specified
c
      if (nfit .eq. 0) then
         nfit = min(n1,n2)
         do i = 1, nfit
            ifit(1,i) = i
            ifit(2,i) = i
            wfit(i) = 1.0d0
         end do
      end if
c
c     if the weights are all zero, set them to unity
c
```

```
      do i = 1, nfit
         if (wfit(i) .ne. 0.0d0)  goto 10
      end do
      do i = 1, nfit
         wfit(i) = 1.0d0
      end do
   10 continue
c
c     find the rms fit of input coordinates
c
      if (verbose) then
         rmsvalue = rmsfit (x1,y1,z1,x2,y2,z2)
         write (iout,20)  rmsvalue
   20    format (/,' IMPOSE  --  Input Coordinates',12x,f12.6)
      end if
c
c     superimpose the centroids of active atom pairs
c
      call center (n1,x1,y1,z1,n2,x2,y2,z2,xmid,ymid,zmid)
      if (verbose) then
         rmsvalue = rmsfit (x1,y1,z1,x2,y2,z2)
         write (iout,30)  rmsvalue
   30    format (' IMPOSE  --  After Translation',12x,f12.6)
      end if
c
c     use a quaternion method to achieve the superposition
c
      call quatfit (n1,x1,y1,z1,n2,x2,y2,z2)
      rmsvalue = rmsfit (x1,y1,z1,x2,y2,z2)
      if (verbose) then
         write (iout,40)  rmsvalue
   40    format (' IMPOSE  --  After Rotation',15x,f12.6)
      end if
c
c     translate both coordinate sets so as to return
c     the first set to its original position
c
      do i = 1, n1
```

```
         x1(i) = x1(i) + xmid
         y1(i) = y1(i) + ymid
         z1(i) = z1(i) + zmid
      end do
      do i = 1, n2
         x2(i) = x2(i) + xmid
         y2(i) = y2(i) + ymid
         z2(i) = z2(i) + zmid
      end do
      return
      end
c     ##
##
c     ##  subroutine quatfit  --  quaternion superposition of
coords  ##
c     ##
##
c
c
c     "quatfit" uses a quaternion-based method to achieve the
best
c     fit superposition of two sets of coordinates
c
c     literature reference:
c
c     S. K. Kearsley, "On the Orthogonal Transformation Used
for
c     Structural Comparisons", Acta Crystallographica Section
A,
c     45, 208-210 (1989)
c
c     adapted from an original program written by D. J.
Heisterberg,
```

```
c     Ohio Supercomputer Center, Columbus, OH
c
c
      subroutine quatfit (n1,x1,y1,z1,n2,x2,y2,z2)
      implicit none
      include 'sizes.i'
      include 'align.i'
      integer i,i1,i2,n1,n2
      real*8 weigh,xrot,yrot,zrot
      real*8 xxyx,xxyy,xxyz
      real*8 xyyx,xyyy,xyyz
      real*8 xzyx,xzyy,xzyz
      real*8 q(4),d(4)
      real*8 work1(4),work2(4)
      real*8 rot(3,3)
      real*8 c(4,4),v(4,4)
      real*8 x1(maxatm),x2(maxatm)
      real*8 y1(maxatm),y2(maxatm)
      real*8 z1(maxatm),z2(maxatm)


c
c
c     build the upper triangle of the quadratic form matrix
c


       xxyx = 0.0d0
      xxyy = 0.0d0
      xxyz = 0.0d0
      xyyx = 0.0d0
      xyyy = 0.0d0
      xyyz = 0.0d0
      xzyx = 0.0d0
      xzyy = 0.0d0
      xzyz = 0.0d0
      do i = 1, nfit
         i1 = ifit(1,i)
```

```
            i2 = ifit(2,i)
            weigh = wfit(i)
            xxyx = xxyx + weigh*x1(i1)*x2(i2)
            xxyy = xxyy + weigh*y1(i1)*x2(i2)
            xxyz = xxyz + weigh*z1(i1)*x2(i2)
            xyyx = xyyx + weigh*x1(i1)*y2(i2)
            xyyy = xyyy + weigh*y1(i1)*y2(i2)
            xyyz = xyyz + weigh*z1(i1)*y2(i2)
            xzyx = xzyx + weigh*x1(i1)*z2(i2)
            xzyy = xzyy + weigh*y1(i1)*z2(i2)
            xzyz = xzyz + weigh*z1(i1)*z2(i2)
         end do
         c(1,1) = xxyx + xyyy + xzyz
         c(1,2) = xzyy - xyyz
         c(2,2) = xxyx - xyyy - xzyz
         c(1,3) = xxyz - xzyx
         c(2,3) = xxyy + xyyx
         c(3,3) = xyyy - xzyz - xxyx
         c(1,4) = xyyx - xxyy
         c(2,4) = xzyx + xxyz
         c(3,4) = xyyz + xzyy
         c(4,4) = xzyz - xxyx - xyyy
c
c     diagonalize the quadratic form matrix
c
         call jacobi (4,4,c,d,v,work1,work2)
c
c     extract the desired quaternion
c
         q(1) = v(1,4)
         q(2) = v(2,4)
         q(3) = v(3,4)
         q(4) = v(4,4)
c
c     assemble rotation matrix that superimposes the molecules
c
         rot(1,1) = q(1)**2 + q(2)**2 - q(3)**2 - q(4)**2
         rot(2,1) = 2.0d0 * (q(2) * q(3) - q(1) * q(4))
```

```
      rot(3,1) = 2.0d0 * (q(2) * q(4) + q(1) * q(3))
      rot(1,2) = 2.0d0 * (q(3) * q(2) + q(1) * q(4))
      rot(2,2) = q(1)**2 - q(2)**2 + q(3)**2 - q(4)**2
      rot(3,2) = 2.0d0 * (q(3) * q(4) - q(1) * q(2))
      rot(1,3) = 2.0d0 * (q(4) * q(2) - q(1) * q(3))
      rot(2,3) = 2.0d0 * (q(4) * q(3) + q(1) * q(2))
      rot(3,3) = q(1)**2 - q(2)**2 - q(3)**2 + q(4)**2
c
c     rotate second molecule to best fit with first molecule
c
      do i = 1, n2
         xrot = x2(i)*rot(1,1) + y2(i)*rot(1,2) +
z2(i)*rot(1,3)
         yrot = x2(i)*rot(2,1) + y2(i)*rot(2,2) +
z2(i)*rot(2,3)
         zrot = x2(i)*rot(3,1) + y2(i)*rot(3,2) +
z2(i)*rot(3,3)
         x2(i) = xrot
         y2(i) = yrot
         z2(i) = zrot
      end do
      return
      end
c#############################################################
c     ##
##
c     ##  subroutine jacobi  --  jacobi matrix diagonalization
##
c     ##
##
c
#############################################################
c
c
c     "jacobi" performs a matrix diagonalization of a real
c     symmetric matrix by the method of Jacobi rotations
c
c     variables and parameters:
```

```
c
c     n     logical dimension of the matrix to be diagonalized
c     np    physical dimension of the matrix storage area
c     a     input with the matrix to be diagonalized; only
c              the upper triangle and diagonal are required
c     d     returned with the eigenvalues in ascending order
c     v     returned with the eigenvectors of the matrix
c     b     temporary work vector
c     z     temporary work vector
c
c
      subroutine jacobi (n,np,a,d,v,b,z)
      implicit none
      include 'iounit.i'
      integer i,j,k
      integer n,np,ip,iq
      integer nrot,maxrot
      real*8 sm,tresh,s,c,t
      real*8 theta,tau,h,g,p
      real*8 d(np),b(np),z(np)
      real*8 a(np,np),v(np,np)
c
c
c     setup and initialization
c
      maxrot = 100
      nrot = 0
      do ip = 1, n
         do iq = 1, n
            v(ip,iq) = 0.0d0
         end do
         v(ip,ip) = 1.0d0
      end do
      do ip = 1, n
         b(ip) = a(ip,ip)
         d(ip) = b(ip)
         z(ip) = 0.0d0
      end do
```

```
c
c     perform the jacobi rotations
c
      do i = 1, maxrot
         sm = 0.0d0
         do ip = 1, n-1
            do iq = ip+1, n
               sm = sm + abs(a(ip,iq))
            end do
         end do
         if (sm .eq. 0.0d0)  goto 10
         if (i .lt. 4) then
            tresh = 0.2d0*sm / n**2
         else
            tresh = 0.0d0
         end if
         do ip = 1, n-1
            do iq = ip+1, n
               g = 100.0d0 * abs(a(ip,iq))
               if (i.gt.4 .and. abs(d(ip))+g.eq.abs(d(ip))
     &                     .and. abs(d(iq))+g.eq.abs(d(iq)))
then
                  a(ip,iq) = 0.0d0
               else if (abs(a(ip,iq)) .gt. tresh) then
                  h = d(iq) - d(ip)
                  if (abs(h)+g .eq. abs(h)) then
                     t = a(ip,iq) / h
                  else
                     theta = 0.5d0*h / a(ip,iq)
                     t = 1.0d0 /
(abs(theta)+sqrt(1.0d0+theta**2))
                     if (theta .lt. 0.0d0)  t = -t
                  end if
                  c = 1.0d0 / sqrt(1.0d0+t**2)
                  s = t * c
                  tau = s / (1.0d0+c)
                  h = t * a(ip,iq)
                  z(ip) = z(ip) - h
```

```
                z(iq) = z(iq) + h
                d(ip) = d(ip) - h
                d(iq) = d(iq) + h
                a(ip,iq) = 0.0d0
                do j = 1, ip-1
                   g = a(j,ip)
                   h = a(j,iq)
                   a(j,ip) = g - s*(h+g*tau)
                   a(j,iq) = h + s*(g-h*tau)
                end do
                do j = ip+1, iq-1
                   g = a(ip,j)
                   h = a(j,iq)
                   a(ip,j) = g - s*(h+g*tau)
                   a(j,iq) = h + s*(g-h*tau)
                end do
                do j = iq+1, n
                   g = a(ip,j)
                   h = a(iq,j)
                   a(ip,j) = g - s*(h+g*tau)
                   a(iq,j) = h + s*(g-h*tau)
                end do
                do j = 1, n
                   g = v(j,ip)
                   h = v(j,iq)
                   v(j,ip) = g - s*(h+g*tau)
                   v(j,iq) = h + s*(g-h*tau)
                end do
                nrot = nrot + 1
             end if
          end do
       end do
       do ip = 1, n
          b(ip) = b(ip) + z(ip)
          d(ip) = b(ip)
          z(ip) = 0.0d0
       end do
    end do
```

```
c
c     print warning if not converged
c
   10 continue
      if (nrot .eq. maxrot) then
         write (iout,20)
   20    format (/,' JACOBI  --  Matrix Diagonalization not
Converged')
      end if
c
c     sort the eigenvalues and vectors
c
      do i = 1, n-1
         k = i
         p = d(i)
         do j = i+1, n
            if (d(j) .lt. p) then
               k = j
               p = d(j)
            end if
         end do
         if (k .ne. i) then
            d(k) = d(i)
            d(i) = p
            do j = 1, n
               p = v(j,i)
               v(j,i) = v(j,k)
               v(j,k) = p
            end do
         end if
      end do
      return
      end
c#############################################################
c     ##
##
c     ##  function rmsfit  --  rms deviation for paired atoms
##
```

```
c     ##
##
c#############################################################
c
c
c     "rmsfit" computes the rms fit of two coordinate sets
c
c
      function rmsfit (x1,y1,z1,x2,y2,z2)
      implicit none
      include 'sizes.i'
      include 'align.i'
      integer i,i1,i2
      real*8 rmsfit,rmsterm
      real*8 xr,yr,zr,dist2
      real*8 weigh,norm
      real*8 x1(*),x2(*)
      real*8 y1(*),y2(*)
      real*8 z1(*),z2(*)
c
c
c     compute the rms fit over superimposed atom pairs
c
      rmsfit = 0.0d0
      norm = 0.0d0
      do i = 1, nfit
         i1 = ifit(1,i)
         i2 = ifit(2,i)
         weigh = wfit(i)
         xr = x1(i1) - x2(i2)
         yr = y1(i1) - y2(i2)
         zr = z1(i1) - z2(i2)
         dist2 = xr**2 + yr**2 + zr**2
         norm = norm + weigh
         rmsterm = dist2 * weigh
         rmsfit = rmsfit + rmsterm
      end do
      rmsfit = sqrt(rmsfit/norm)
```

```
return
end
```

References:

(1) Milano, G.; Muller-Plathe, F. *Journal of Physical Chemistry B* **2005**, *109*, 18609.
(2) Brasiello, A.; Crescitelli, S.; Milano, G. *Faraday Discussions* **2012**, *158*, 479.
(3) Kearsley, S. *Acta Crystallographica Section A* **1989**, *45*, 208.